Transition Metal Dichalcogenides Nanostructure/Graphene van der Waals Heterostructure for Surface Enhanced Raman Spectroscopy

By

Samar Ghopry
DPhil, University of Kansas, 2021
M.D., Virginia Commonwealth University, 2014
B.Sc., University of Jazan , 2007

Submitted to the graduate degree program in Department of Physics and Astronomy and the Graduate Faculty of the University of Kansas in partial fulfillment of the requirements for the degree of Doctor of Philosophy.

_____

Chair: Prof. Judy Wu

_____

Prof. Cindy L. Berrie

_____

Prof. Wai-Lun Chan

_____

Prof. Hartwin Peelaers

_____

Prof. Hui Zhao

Date Defended: 26 July 2021

The dissertation committee for Samar Ghopry certifies that this is the approved version of the following dissertation:

Transition Metal Dichalcogenides Nanostructure /Graphene van der Waals Heterostructure for Surface Enhanced Raman Spectroscopy

_____

Chair: Prof. Judy Wu

Date Approved: 10 December 2021

Abstract

Two-dimensional (2D) Van der Waals (vdW) heterostructures of graphene and transition metal dichalcogenides (TMDs/Graphene) provide a promising new material platform since it integrates the superior light–solid interaction in TMDs and ultrafast charge mobility in graphene, and therefore is promising for surface-enhanced Raman spectroscopy (SERS). This thesis explores design, fabrication and application of new SERS substrates based on novel TMD (MoS_2 and WS_2) nanostructure/graphene vdW heterostructures. Specifically, the design is guided by enhancing electromagnetic mechanism (EM) through development TMDs nanostructure for a strong localized surface plasmonic resonance (LSPR) upon light illumination and chemical mechanism (CM) via facilitating charge transfer between probe molecules of 2D materials.

In order to achieve high EM enhancement on the TMDs/graphene vdW SERS substrates, schemes in generating nanostructures of TMDs, including 1) nanodiscs (N-discs), 2) intermixed N-discs of MoS_2 and WS_2, 3) nanodonuts (N-donuts), and 4) their superposition with gold nanoparticles (AuNPs) have been explored. An extraordinary SERS sensitivity has been achieved on these substrates using fluorescent Rhodamine 6G (R6G) as probe molecules.

In Topic 1, Novel SERS substrate has been developed based on non-metallic TMD N-discs on single-layer CVD graphene/SiO_2/Si. This Substrate provided a high-performance SERS with EM and CM enhancement, both are associated with the strong dipole-dipole interaction at the heterostructure interface as indicated by the Density Function Theory (DFT) and ab-initio molecular dynamics simulation (AMID) simulations. Using fluorescent Rhodamine 6G (R6G) as probe molecules, an extraordinary SERS sensitivity up to $5X10^{-12}$ M was obtained on TMD N-discs/graphene vdW heterostructure substrate, using 532 nm Raman excitation. This sensitivity is 4-5 orders of magnitude higher than that of the single-layer MoS_2, WS_2 or graphene substrates and

is comparable and slightly better than the best reported plasmonic metal nanostructures/graphene SERS substrates. The enhancement factors were calculated by comparing the intensity of the Raman feature peak of R6G at 613 cm^{-1} obtained on different substrates, enhancement factor of 7-9 can be achieved on the MoS_2 N-discs/graphene or WS_2 N-discs/graphene vdW heterostructures with respect to the single-layer MoS_2, WS_2 or graphene reference. Importantly, SERS enhancement and sensitivity drop significantly when the TMD N-discs are replaced with a continuous TMD layer on graphene, indicating the TMD dimension and shape are highly relevant. Besides, the peak intensity of graphene's Raman signature with TMD N-discs is enhanced by factor of 8-10 as compared to that of graphene only, demonstrating the LSPR effect provided by the TMD N-discs.

In Topic 2, we explores a rationale design of intermixed WS_2 N-discs and MoS_2 N-discs on graphene (WS_2 N-discs s+MoS_2 N-discs/graphene) for ultrasensitive SERS beyond the sensitivity limit of the SERS substrates based on metallic plasmonic nanostructures. The intermixed WS_2 N-discs +MoS_2 N-discs/graphene allows superposition of the LSPR effects from the two types of plasmonic NDs. The enhanced SERS sensitivity is illustrated in the boosted graphene Raman peaks by approximately 14 fold on the WS_2 N-discs+MoS_2 N-discs/graphene, in contrast to ~ 7.6 fold on the counterparts with single types of the NDs. Furthermore, the SERS enhancement factors of R6G of $5x10^{-5}$ M concentration Raman spectra (normalized to that on graphene) are ~ 16.4 and 8.1 considering the R6G 613 cm^{-1} peak intensities were sensed on the WS_2 N-discs+MoS_2 N-discs/graphene and MoS_2-N-discs/graphene (or WS_2-N-discs/graphene), respectively. In addition, the WS_2N-discs+MoS_2 N-discs/graphene SERS substrate exhibits remarkably high SERS sensitivity as high as 5-7$\times10^{-13}$ M.

In Topic 3, We also further explored the effect of the TMDs nanostructure shape on electromagnetic enhancement and SERS and we reported a controllable growth of MoS_2 nanodonuts (N-donuts) and nanodiscs (N-discs) on graphene and show that the MoS_2 N-donuts exhibits considerably higher LSPR sensitivity than the MoS_2 N-discs. Using R6G as a probe, SERS spectra were compared on MoS_2 N-donuts/graphene and MoS_2 N-discs/graphene vdW heterostructures substrates. The former exhibits remarkably higher R6G SERS sensitivity up to 2×10^{-12} M, in contrast to 5×10^{-12} M on the MoS_2 N-discs/graphene vdW heterostructures substrate, which can be attributed to the more robust LSPR effect by the finite difference time-domain simulation.

In Topic 4, we explore superposition of LSPR effect of Au nanoparticles (AuNPs) with that on WS_2 N-discs. The LSPR superposition is confirmed first when Raman signatures of graphene, such as the G-peak intensity got enhanced by approximately 7.8 fold on the AuNPs/WS_2 N-Discs/graphene over that of reference graphene sample, in contrast to 4.0 and 5.3 folds respectively on AuNPs/graphene and on WS_2 N-discs/graphene. Furthermore, Raman spectra of probe molecules of R6G were employed to quantify the enhanced SERS on AuNPs/WS_2 N-discs/graphene SERS substrates. At the R6G concentration of $5x10^{-5}$ M, enhancement factors of ~ 2.0 and 2.4 based on the R6G 613 cm^{-1} peak intensity are observed on the AuNPs/WS_2 N-discs/graphene with respect to that on WS_2 N-discs/graphene and AuNPs/graphene, respectively. The benefit of the superposition of the LSPR effects from the WS_2 N-discsand AuNPs results in high SERS sensitivity up to 1×10^{-12} M on AuNPs/WS_2 N-discs/graphene, which is more than an order of magnitude higher than that on WS_2 N-discs/graphene, and several orders of magnitude higher than that on the AuNPs/graphene and metal nanostructure/TMD (continuous layer) substrates.

Acknowledgements

I would like to first thank my advisor and mentor Professor Judy Wu for her guidance and supervision of this long process of PhD study. Dr. Wu has been tremendous help during the process of my PhD research and dissertation development, I cannot imagine how difficult and long lasting it would have been without her. I would like to also mention how welcoming and supportive she has been since the day I joined her group and started this journey. One last time I would like to thank my advisor Dr. Judy Wu.

Second, I would like to thank the Dissertation Committee: Professors Cindy L. Berrie, Wai-Lun Chan, Hartwin Peelaers, and Hui Zhao for the valuable times they have spent in evaluating my dissertation and attending my PhD defense. Please accept my deepest appreciation for all the help you have given me in these important processes!

I would like to express my greatest gratitude to my husband, Mohammed. Without his inspiration and heartily support, I would not be here. My journey to the United States was made possible because of him and his sacrifices. Since arriving at the University of Kansas, he has always reminded me of my ambition to achieve a PhD degree and to make my family proud. I would like to also thank my parents, children, brothers and sisters for sticking by myside in this journey. A special thanks goes to my children. During the past three months particularly I have been working late in lab and

on my thesis, I know they missed me, but they had supported each other with their father's precious help.

I would like to also mention my thanks to my colleagues in Wu laboratory and beyond for their invaluable assistance and encouragement since joining this department.

Also, I gratefully acknowledge The University of Jizan in Saudi Arabia for providing a full scholarship for my PhD study towards a scientific profession. Additionally, I acknowledge the further financial support from the University of Kansas. This long process was made easier and possible with these help mentioned above.

I would like to thank my theoretical collaborators, Professors Seyed Sadeghi and Ridwan Sakidia. They have provided valuable simulations for my experimental works. A special thanks goes to Professor Cindy L. Berrie for the valuable contributions to several of my publications in characterization for the samples.

Finally, I would like to thank the Department of Physics and Astronomy, the University of Kansas, for all of their support that makes my PhD study a memorable experience filled with hard works and joys. I would like to extend my thanks especially to Professor Feldman, Professor Rudnick, Mrs. Kristin Rennells, and Graduate Advisor Sauerwein Joel.

List of Publications

1. Extraordinary Sensitivity of Surface-Enhanced Raman Spectroscopy of Molecules on MoS_2 (WS_2) Nanodomes/Graphene van der Waals Heterostructure Substrates

   Samar Ali Ghopry, Mohammed Alamri, Ryan Goul, Ridwan Sakidja, and Judy Wu, Adv. Optical Mater. 2019, 1801249

2. Plasmonic Au Nanoparticles on 2D MoS_2/graphene van der Waals Heterostructures for High-Sensitivity Surface Enhanced Raman Spectroscopy

   Mohammed Alamri, Ridwan Sakidja, Ryan Goul, Samar Ghopry, and Judy Z. Wu, ACS Appl. Nano Mater. 2019, 2, 3, 1412–1420

3. Au Nanoparticle/WS_2 Nanodome/Graphene van der Waals Heterostructure Substrates for Surface-Enhanced Raman Spectroscopy

   Samar Ali Ghopry, Mohammed Alamri, Ryan Goul, Brent Cook, Seyed Sadeghi, Rithvik R. Gutha, Ridwan Sakidja, and Judy Z. Wu. ACS Appl. Nano Mater. 2020, 3, 3, 2354–2363

4. Intermixed WS_2+MoS_2 Nanodisks/Graphene van der Waals Heterostructures for Surface-Enhanced Raman Spectroscopy Sensing

   Samar Ali Ghopry, Seyed Sadeghi, Yasmine Farhat, Cindy Berrie, Mohammed Alamri, and Judy Wu. ACS Appl. Nano Mater. 2021, 4, 3, 2941–2951

5. MoS_2 Nanodonuts for high-Sensitivity Surface-Enhanced Raman Spectroscopy Sensing

   Samar Ali Ghopry, Seyed Sadeghi, Cindy L. Berrie and Judy Z. Wu Biosensors 2021, *11*(12), 4

Table of Contents

List of Figures

Chapter 1: Introduction

1.1 Overview of Two Dimensional (2D) Materials

The Family of two dimensional (2D) materials represents a novel class of materials consist of single- or few-layer atomic sheets of crystalline materials of a variety of physical properties ranging from metallic, insulating and semiconducting. Researches that investigate the unique properties of the 2Dmaterials, including electronic, optical, mechanical, thermal, optoelectronic, etc., have grown rapidly with a broad interest in applications since the discovery of graphene by Andre Geim and Kostya Novoseov in 2004 [1]. In these 2D materials, the atoms are organized into layers and held together by powerful in-plane bonds. Therefore, they typically have strong in-plane mechanical properties. In contrast, their bulk layered counterparts consist of sheets staked together via weak van der Waals (vdW) forces along the out-of-plane direction, which means that the layers can be separated easily even using a scotch tape, resulting in monolayer and few layer materials with different properties than their bulk counterparts due to the quantum confinement of charge carriers in the direction perpendicular to the sheets [2]. These include strong interaction with light, high carrier mobility, and tunable electronic and optical properties, making them promising candidates for applications in electronic, optoelectronic, and other devices [3]. Besides the single-layered form, the 2D atomic layers can be stacked together to vdW heterostructures, permitting a theoretically infinite number of combinations of 2D materials to combine or create new materials with unique properties. Finally, due to the different electronic properties of 2D materials they can cover a very broad range of the electromagnetic spectrum as shown in Figure 1.1.1 [4].

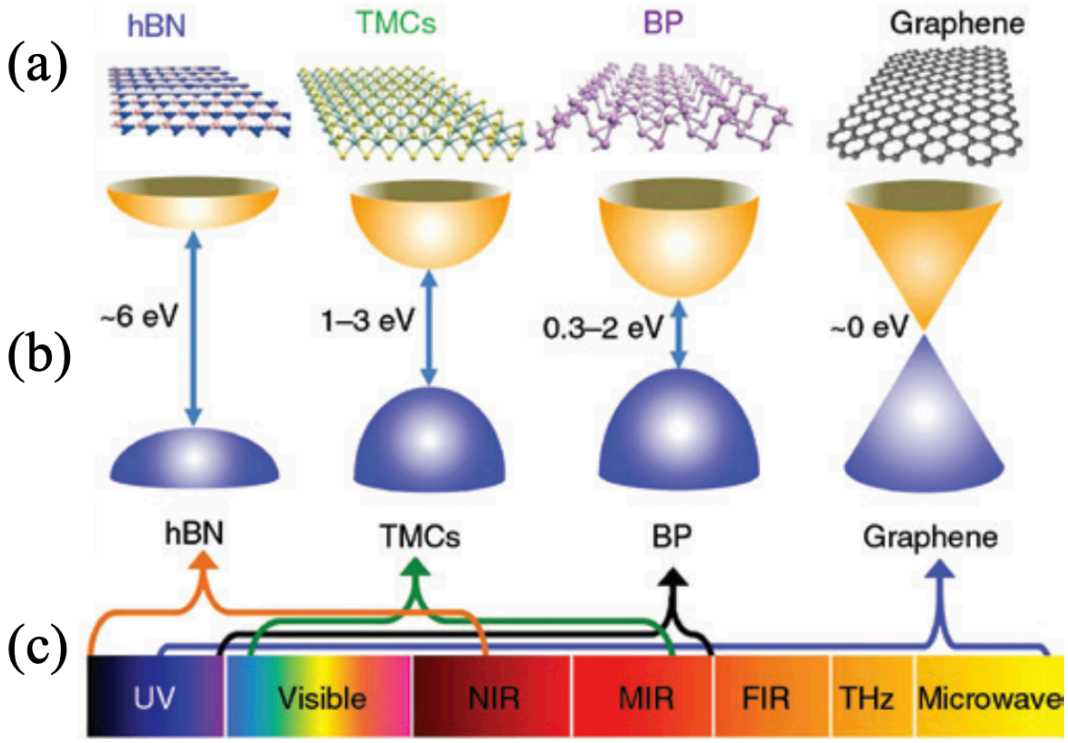

Figure 1.1.1 Atomic crystal structure of 2 D material (a), the corresponding electronic band structure (B), and accessible wavelength spectrum [4]

1.2 Graphene

Graphene, a novel atomic sheet (2D material monolayer) of carbons atoms, has exhibited great potentials in numerous fields due to its unique electronic[5], optical[6] thermal[7] and mechanical[8] properties. The carbons atoms organized in a honeycomb lattice created by the triangular planar organization of carbon-carbon strong in-plane covalent bonds (σ bonds: sp2 hybridization bonding (Figure 1.2.1 a [9])) that is responsible for graphene's excellent mechanical properties such as stability, and half-filled out-of-plane π bands that arise from the electron in the P_z orbitals. The π bond contributes to a delocalized net of electrons and therefore responsible for the high electrical and thermal conductivity that behave like relativistic particles described by the Dirac equation [10]. Due to unique electronic structure of graphene (special π-π* band

structure), graphene is a zero-gap semiconductor (semi-metal). The valence band and conduction band are symmetric around the six corners at the K point (Dirac point). This leads to a linear energy-momentum relation (the dispersion relation) near the six corners of the 2D hexagonal Brilloun zone and consequently leads to massless electrons and holes that behave like relativistic particles described by the Dirac equation leading to extremally high charge mobility [11], (Figure 1.2.1 c-e [9])).

Since the discovery of graphene, extensive researches have demonstrated the novel properties of graphene including high specific surface area, mechanical strength (breaking strength ~42 N $m^{-1}$and Young's modulus ~1100GPa), thermal conductivity around 5000 W mK-1at room temperature), high optical transparency (only ~2.3% absorption towards visible lights) together with extraordinary electronic conductivity , and high charge mobility (~200,000 cm^2 V^{-1} s^{-1}, due to the charges confined to 2-D) [6, 12-14]. Besides all of the fantastic properties, graphene being a fundamental bio-compatible surface and its relatively low cost and scalable fabrication make graphene extremely attractive for optoelectronic such as biosensor applications [15, 16].

Despite these novel properties, graphene still has limitations in optoelectrical applications and devices due to its zero bandgap. Therefore, many recent studies have focused on other 2D materials with finite bandgaps. At the same time, due to the large aera and high-quality producible graphene and able transfer process, currently graphene holds promise in flexible electronics such as organic light-emitting diode (OLED) [17], electrochemical sensors[18, 19],

field-effect transistors (FETs) [20, 21], touch screen [22] and photodetector [23].

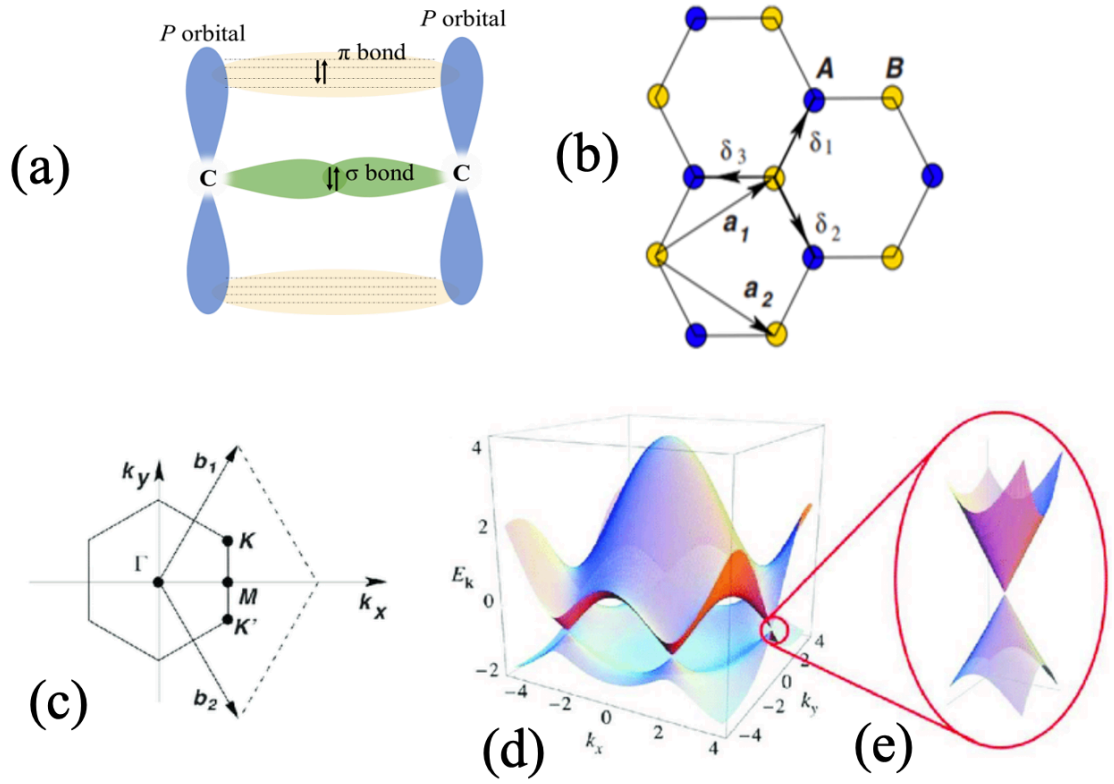

Figure 1.2.1 Sigma and pi bonds formed by sp^2 hybridization in graphene (b) The lattice structure (honeycomb lattice) of graphene. (c) Corresponding Brillouin zone. (d) Electronic dispersion of graphene in the honeycomb lattice (e) zoom in energy bands close to one of the Dirac point [9]

Among various novel 2D materials discovered so far, TMDs have received extensive attention recently due to their unique physical properties. TMDs are composed of MX_2, where M is a metal element (Mo, W, etc.), sandwiched between two X layers, where X is a chalcogen (Te, S or Se) [24]. In TMDs, the adjacent atomic thin layers weakly interact and hold together by vdW forces although within the layer, strong in-plane covalent bonds formed in-between the transition metal (M) and chalcogen (X) atoms creating X-M-X sandwich assembly for each layer of MX_2 [25]. Due to the week Van der Waals interaction between the layers, TMDs can be effectively exfoliated into few layers or indeed monolayers. The study of the structure of the most important TMDs, MoS_2, can be traced back to 1923 [26]. TMDs has different electronic

properties from metallic to semiconductor, depending on the MX_2 layers stacking sequence and their metal coordination which lead to a few polymorphs in TMDs, including 1T, 2H, and 3R. Furthermore, it has been demonstrated experimentally that when TMDs' band structure has a transition from the indirect-to-direct bandgap semiconductor when the TMDs thickness is reduced from bulk to single layer. The direct band gap can significantly improve the effectiveness of the electrons and holes radiative recombination which can rise the photoluminescence quantum efficiency from the excitons [27]. Furthermore, direct bandgap in 2D TMD monolayer result in the high light absorption, TMD can absorb up to 10% of incident light [28]. Therefore, TMDs are very interesting material for the future optoelectronic applications such as photodetectors [29] and light emitting diodes [30].MoS_2, for example, is a semiconductor with an indirect bandgap of 1.29 eV in its bulk form and a direct bandgap of 1.9 eV when it is a single-layer [27, 31], Figures 1.2.2 a-b show the crystal structure of MoS_2[32] and 1.3.1c shows the calculated electronic band structures of bulk, four-layer, two-layer, and single-layer MoS_2 (from left to right) [32]. This transition is caused by shifting of the maximum valence band and minimum conduction band locating at the K point of the Brillouin zone, resulting in the alignment of the maximum and minimum and the rise of the bandgap as the number of layers decreases. Moreover, the TMDs semiconductors with large band gaps around 1 – 2 eV that are greater than that of Si (1.11 eV) are interesting since their bandgaps are in the visible light energy spectrum, leading to an extensive range of applications that are projected to be implemented in field-effect transistors (FET) and optoelectronics device applications such thin-film solar cells [2, 3, 33]., Beside all of the unique electronic and optical properties of the TMD [34] such as the possibility of bandgap tuning, strong light-matter interaction, and large exciton bind energy, the ability of the fabrication

of this ultrathin sheet materials on flexible and transparent devices makes these materials very interesting for electronic, optical, and optoelectronic future applications..

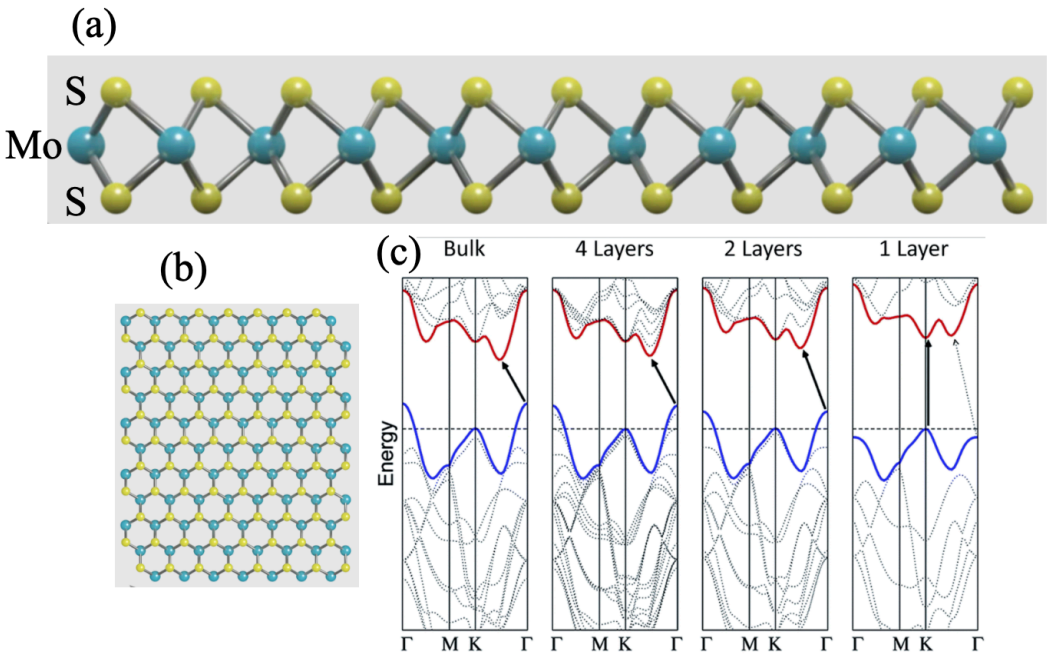

Figure 1.2.2 Side view (a) and top view (b) of the crystal structure of monolayer MoS_2 showing a layer of molybdenum atoms (Mo) (blue) sandwiched between two layers of sulfur (S) atoms (yellow). (c) Calculated electronic band structures of bulk, four-layer, two-layer, and single-layer MoS2 (from left to right)[32]

1.3 Two-dimensional van der Waals heterostructures

Different 2D materials can be stacked on top of each other to form heterostructures like LEGOs (Figure 1.3.1, [35].). These 2D heterostructures can be regarded as artificial materials collected in a chosen sequence with novel properties. In these 2D materials heterostructures, the vertical stacking does not require lattice match between constituent layers [36], which is a stringent requirement for conventional epitaxial heterostructures. The graphene hexagonal boron nitride/(hBN) vdW heterostructure was the first successful vdW heterostructure assembly where hBN served as a high-quality substrate (less charge defects as compared to SiO_2/Si and many other dielectric substrates) for graphene [37]. This is beneficial considering the charge defects on substrates can generate charge (holes and electrons) scattering and therefore reduce charge

mobility. Furthermore, the electrical and optical properties of these 2D heterostructures can be tuned due to the interlayer coupling. For example, in MoS_2/WS_2 heterojunctions, the photoexcited holes and electrons separate in the two opposite layers leading to effective charge transfer [38]. The mechanical properties of heterostructures can be tuned, too. For example, elastic stiffness of MoS_2/WS_2 and MoS_2/graphene heterostructures are about 314 and 467 N/m, respectively [39]. TMDs/graphene vdW heterostructure, have received extensive attention in various applications recently due the mixing of their unique performance and preparties such as the direct band gap and superior light-absorption of monolayer TMDs and ultrafast charge mobility of graphene.

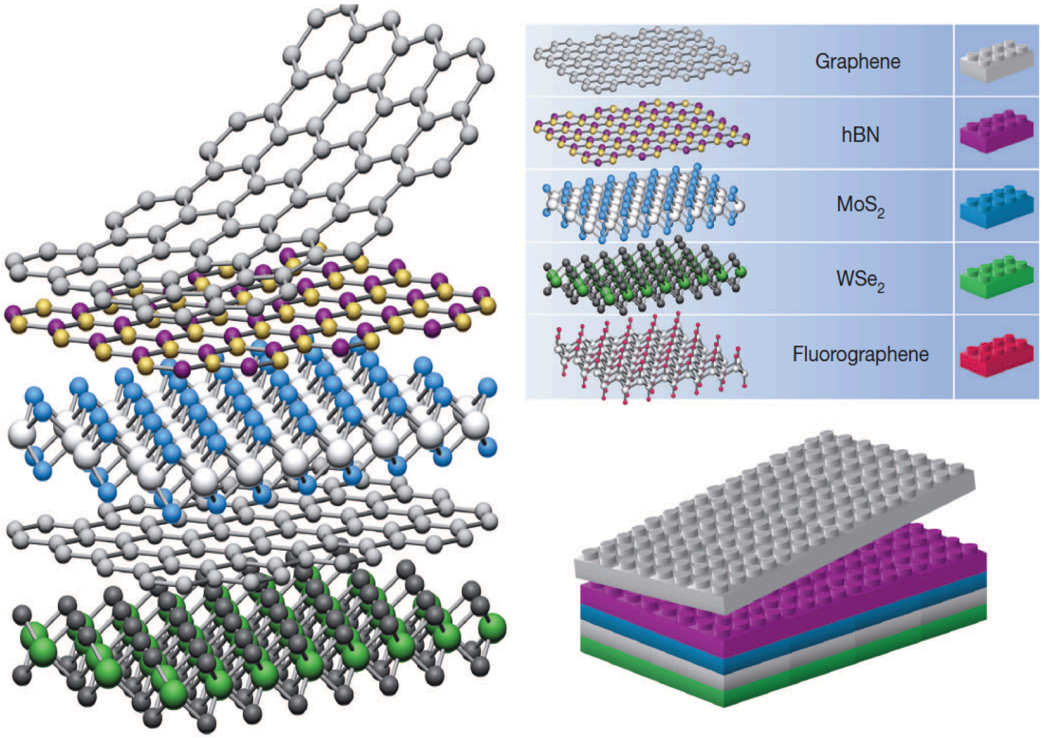

Figure 1.3.1 Concept of assembling 2D heterostructures as similar to Lego Block [35].

1.4 Raman Spectroscopy

Raman spectroscopy is a spectroscopic tool based used to identify the vibrational modes of the molecules based on the transferred energy when a molecule scatters an incident photon. Raman

scattering can be interpreting physically by one of two ways: the quantum interaction picture and the classical interaction picture. In the quantum interaction, is represented in Figure 1.4.1 (a), when a molecules hits by a photon, the electrons of the molecule will be excited to a higher level of energy state and then mostly the molecule will re emit the photons and return to its initial energy level with no net energy been transfer in the system, elastic scattering. This elastic scattering is known as Rayleigh scattering. However, rarely, small fraction (one of 10^7) of the excited molecule may land on a different energy level than its original state, resulting in a scattered photon with less (Stokes shifted) or more (anti-Stokes shifted) energy compare to its original energy before the scattering. This inelastic scattering was discovered in 1928 by an Indian physicist Raman and named as Raman scattering. Figure 1.4.1 (b) pictures the classical interaction, where molecular vibrations represented by a simple diatomic molecule. Hooke's law can be utilizing to express the displacement of the molecule as in eq1.1, where the vibration frequency depends on the spring constant (k), and the atomic mass m_1 and m_2.

$$\frac{m_1 m_2}{m_1+m_2}\left(\frac{d^2x_1}{dt^2}+\frac{d^2x_2}{dt^2}\right) = -k(x_1+x_2) \qquad (1.1)$$

x, and k are represent the displacement and bond strength, respectively, using $\mu = \frac{m_1 m_2}{m_1+m_2}$, eq 1.1 will be simplified as,

$$\mu\left(\frac{d^2q}{dt^2}\right) = -k(q) \qquad (1.2)$$

The solution of the equation will be given by:

$$q = q_0 \cos(2\pi v_m t) \qquad (1.3)$$

Where $v_{m=}\frac{1}{2\pi}\sqrt{\frac{K}{\mu}}$,

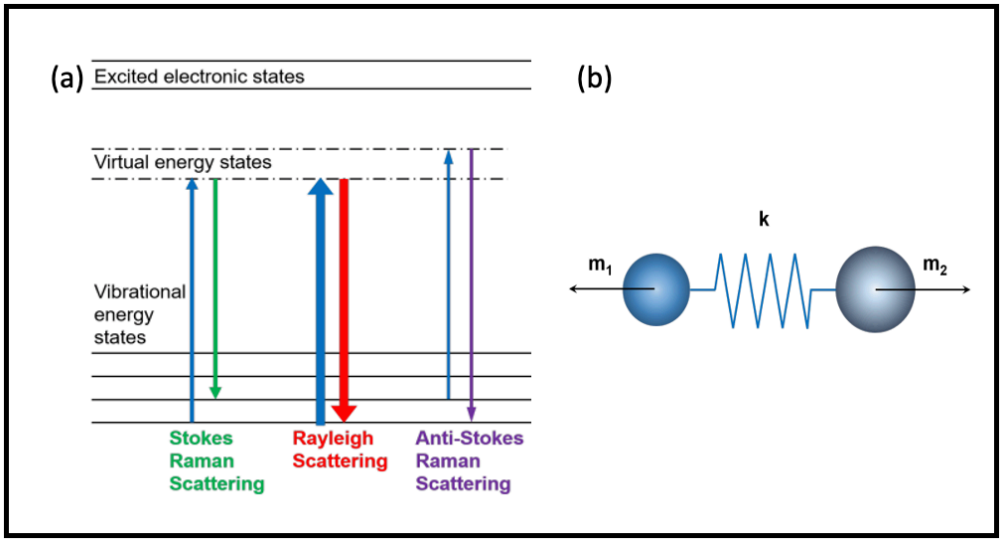

Figure 1.4.1(a) Energy-level diagram representation of the energy shifts in Rayleigh and Raman scattering. (b) the harmonic oscillator representing the diatomic molecule.

Raman spectroscopy, constructed on Raman scattering which becomes extremely useful tool in chemistry to deliver rich structural fingerprint and information of probe molecule as the transferred energy of the scattering procedure matches to a particular transition mode such as vibration or rotation in a molecule, showing the ability to provide rich structural information of the targeted molecules.

However, Raman spectroscopy has its fundamental shortfall in sensitivity since the probability for the occurrence of a Raman scattering is very low. Specially, the cross section of a Raman scattering are often more than five orders of magnitude weaker compare to one of Raleigh scattering. The cross section of a Raman scattering is around 10^{-29} cm^2 that is very small compare to the cross section of fluorescence that is (10^{-19} cm^2) [40]. Therefore, Raman spectroscopy would be limited only for the measurement of the bulk substance if the sensitivity issue can't be addressed. Though, the Surface enhanced Raman spectroscopy (SERS) technology has been shown the ability to enhanced cross section of Raman scattering to be around 10^{-16} cm^2 [40],

making Raman spectroscopy comparable to fluorescence as an ultrasensitive biological and chemical sensor.

1.5 Recent progress made on Surface Enhanced Raman Spectroscopy substrates

SERS is an important mothed for detecting molecules with ultra-high sensitivity [41-44]. By improving the Raman signature of molecules and offer a promising approach for high sensitivity biosensing SERS enables detection of a single molecule [15, 41, 45]. Theoretically, SERS involves two mechanisms: electromagnetic enhancement (EM) and chemical enhancement (CM). The EM involves the local electromagnetic field enhancement that is typically attributed to the localized surface plasmonic resonance (LSPR) ((Figure 1.5.1a [46]) [47, 48]. The surface plasmonic are coherent oscillations of free charge carriers at the surface of the metal nanostructures induced by the incident light. There are two different types of Surface plasmonic; the surface plasmonic polaritons (SPP) and LSPR. In SPP, plasmons propagate along the metal-dielectric interface until its energy is lost to absorptions by the material or scattering to different directions. LSPR (non-propagate) is resulting from the confinement of surface plasmon in a metallic nanoparticles. when spherical metallic nanoparticle is irradiated by light, the electric field causes the free electrons to oscillate coherently and displaced from their nuclei resulting in opposite charge will be build up on the surface of the particle and act as a restoring force for the oscillating electrons due to the Coulombic attraction between electrons and nuclei. Molecules positioned close to the LSPR nanostructures experience an enhanced evanescent electromagnetic field as compared to the incident excitation. This LSPR and therefore EM enhancement directly depends on the morphology of the metal surface, the wavelength of the incident light, carrier density and the dielectric constant of the surrounding medium of the metal. The EM enhancement factor can reach over 10^8 to enable ultrasensitive SERS detection down to the single-molecule level [49-51]. Metal

nanoparticles (NPs) such as Ag and Au NPs have been widely used in SERS because of their unique physical properties that depend on size and shape of the nanoparticles [52, 53].

The CM is induced by charge-transfer between the SERS substrate and molecule with an enhancement factor typically on the order of 10^1 to 10^3[16, 54, 55]. The CM effect is dictated by the interface electronic structures between the analyte and substrate and can be optimized by selecting a substrate with favorable band alignment with the highest-occupied molecular orbital (HOMO) and the lowest-unoccupied molecular orbital (LUMO) at the interface where the analyte (or probe molecule) bond to the substrate.

Thus, tuning of the substrate electronic structure is important to an enhanced CM effect [56]. This has prompted intensive research exploring graphene-based SERS substrates considering the unique two dimensional (2D) atomically flat surface with delocalized π bonds, chemical inertness, biological compatibility, superior electronic and photonic properties, and the intrinsic Fermi energy at ~ 4.5 eV that is compatible, as well as tunable, for CM enhancement with a large number of probe molecules (Figure 1.5.1b [57]) [16, 54, 58, 59]. Therefore, graphene is an excellent SERS substrate primarily due to the CM effect with the adsorbed molecules and the enhancement factor is quantitatively affected by the alignment of the probe molecule electronic structure with the Fermi level of graphene [15, 16].

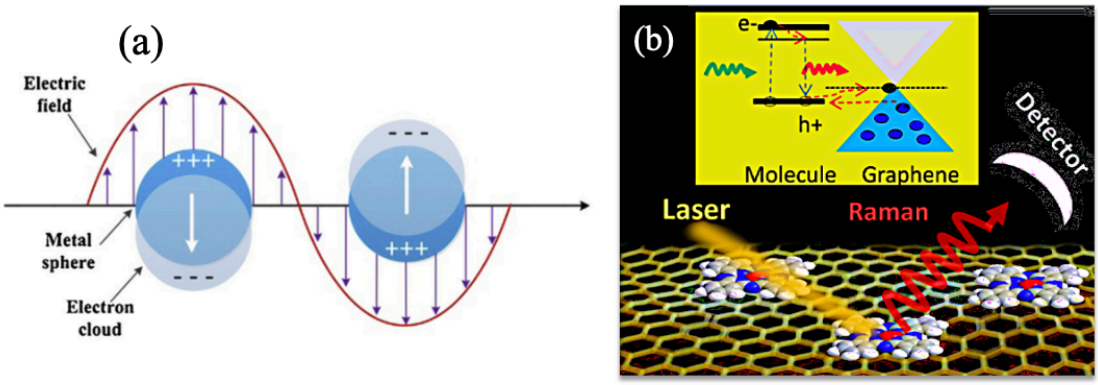

Figure 1.5.1 (a) Schematic description of LSPR in metal NPs when they couple with electric field. Conductive oscillations of electrons are excited and generate localized electromagnetic field in the metal–dielectric interface [46]. (b) Schematic description of the Raman scattered process of graphene-enhanced Raman spectroscopy[57].

Very recently, several members of the TMDs family, especially MoS_2 with a visible-range bandgap (1.9 eV and 1.2-1.4 eV for single- and multilayer MoS_2) approximately, have been shown to be applicable for SERS [60-63]. Qiu *et al* synthesized MoS_2 on flat and Si-pyramids substrate by thermally decomposing the precursor $(NH_4)_2MoS_4$. SERS sensitivity of adenosine and cytidine molecules up to 10^{-6} M was obtained, which is one order of magnitude better than that on the MoS_2-flat-Si substrate [62]. Based on the result, the authors argued that the higher sensitivity from MoS_2/Si-pyramids SERS substrates is caused by the morphology of the substrate since the Si-pyramid arrays can lead the incident laser to oscillate between the valleys of the pyramids and locally enhance incident light. They have also collected the Raman spectra from the Si-pyramid SERS substrates with sensitivity up to 10^{-4} M concentration of adenosine and the authors attributed to low sensitivity to the lack of the surface plasmons on Si-pyramids substrate. Yin *et al* synthesized samples of metallic 1T-MX_2 (with octahedral structure) and the semiconducting 2HMX_2 (with trigonal-prismatic coordination) using a chemical exfoliation method to investigate the Raman enhancement of samples using copper phthalocyanine, R6G, and crystal violet as probe molecules [61]. They reported that the metallic 1T- MX_2 has Raman signatures significantly

higher for the probe molecules tested compared to semiconducting $2HMX_2$ and obtained a SERS sensitivity up to 10^{-8} M using R6G molecules and a 532 nm laser as the excitation source. The authors argued the observed enhancement of SERS due to phase transition can be caused by the extremely efficient charge transfer (or CM effect) from the $1T\text{-}MoX_2$ fermi energy level to HOMO level of the probe molecule.

The EM and CM enhancement factors may be combined by adding metal nanostructures on graphene [54, 64]. Since the optical absorption of graphene is ~ 2.3 % and the intrinsic graphene plasmon is in the THz frequency region, graphene in SERS is considered to be absent of EM contribution. Instead, combining EM enhancement of the metal nanostructures and CM enhancement of graphene to form metal/graphene nanohybrids enables higher SERS enhancement factor than each alone [50, 64-67]. However, the metal/graphene nanohybrids have several disadvantages including the strong spectra noise background introduced by the metal, due to the carbonization effect on the metal surface, the metal-catalyzed side reactions of the probe molecules, and the deformation and distortion of the probe molecules due to the strong metal-adsorbate interactions[15, 16, 55, 58]. In this sense, a metal-free graphene-based nanohybrid SERS substrate with competitive SERS sensitivity becomes increasingly important in both fundamental studies of SERS and its extension to meet the requirements of many practical applications.

1.6 Remaining Critical Issues and Motivation of This Thesis

In SERS, it remains a challenge to design SERS substrates that are able to detect molecules with high sensitivity and selectivity. Plasmonic metal nanostructures on SERS substrates generate significant EM enhancement of the local electromagnetic that can enhance Raman signal of probe molecules. However, the metallic plasmonic nanostructures have several disadvantages including high ohmic losses, strong spectra noise background introduced by the metal, carbonization effect

on the metal surface, the metal-catalyzed side reactions of the probe molecules, and the deformation and distortion of the probe molecules due to the strong metal-adsorbate interactions[15, 16, 55, 58]. Therefore, these traditional noble metal SERS substrates are lack of stability and reproduciblity, which restrict the practical applications of SERS. Furthermore, these metallic materials are costly and required a long and complicated synthetization process.

Motivated by this, this thesis has explored a new design of the 2D vdW heterostructures SERS substrates that have both EM (on TMDs nanostructures) and CM enhancements. The EM effect relies on the induced LSPR facilitated by the dipole-dipole interaction at the TMD nanostructure/graphene vdW interfaces. Further improvement of the EM enhancement has been achieved through control the areal density, and shape of the TMD nanostructures. This thesis, for the first time to our knowledge, illustrates that the non-metallic TMD nanostructure/graphene SERS susbstrates can have SERS sensitivity significantly better that their counterparts' based on metallic nanostructures/graphene heterostructures. This seems not surprising considering the weaknesses of the metallic plasmonic nanostructures mentioned above. In addition, we have shown the LSPR effects from TMDs nanostructures and metallic nanostcrutures can be combined for further enhanced SERS sensitivity. Finally, engineering the surface of the TMD/graphene has been explored and improved CM enhancement has been demonstrated. By optimizing the EM and CM enhancements in the TMD nanostructures/graphene SERS substrates, this thesis illustrates they can be highly promising for practical sensor applications with sensitivity much beyond that of previously developed SERS substrates based on metallic nanostructures.

Chapter 2: Experiment

This chapter reviews the related experimental techniques that have been used in our work for samples synthesis and devices fabrication. It also reviews the characterization techniques that have been used for sample characterization.

2.1 Samples preparation

2.1.1 Synthesis of 2D materials

Generally, 2D atomic materials can be peeled from their 3D parent crystals that are already found in nature using mechanical exfoliation or synthesized in lab (Figure 2.1.1a). Since the out of plane bonding force is much weaker than the in-plane bond between the atoms in the flakes, we can exfoliate them into atomic flakes using scotch tape. This method was the first technique used to create graphene sheet from bulk graphite by Novoselov and Geim in 2004 [1]. It is also used to produce a high quality TMDs. However, the Mechanical Exfoliation has limitation of synthesizing large-scale graphene since it produces only micrometer-sized samples.

The chemical vapor deposition (CVD) method shown in Figure 2.1.1b is one of the most applied methods providing large areas of high quality graphene , described in detail in next section.

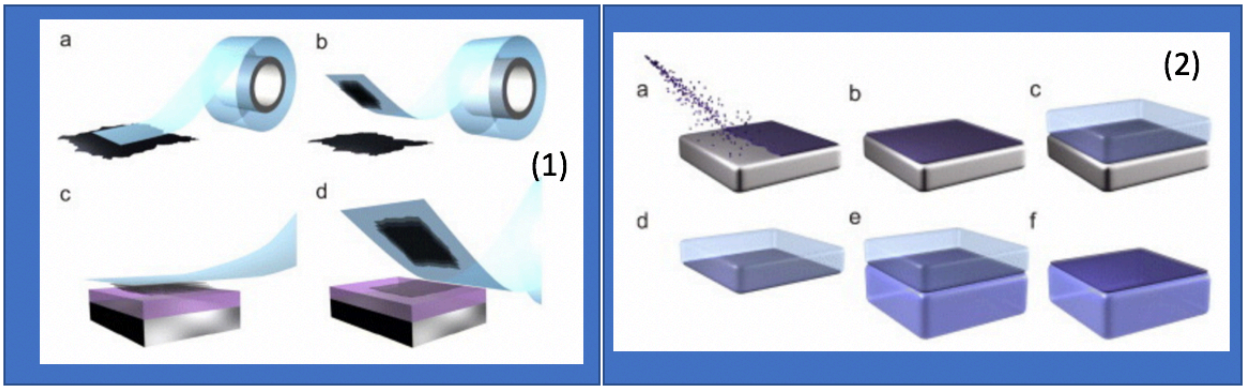

Figure 2.1.1 Micromechanical exfoliation of 2D crystal. (a) The tape placed against a substrate and pulled off (b). The tape with sheet is pressed against the surface (c) and peel off leaving the bottom atomic layer adhered on the surface (d). (2) The chemical vapor deposition. (a) and (b) 2D atomic layer grown by CVD

on metallic surface. (c) The PMMA is spin-coated on the 2D crystal. (d) Etching the metal away, leaving the PMMA/2D crystal. (e) the PMMA/2D crystal is transferred onto the substrate. (f) PMMA is removed [68].

2.1.1.1 Growth of Graphene in Chemical Vapor Deposition

Graphene synthesized process was carried in a quartz tube (25 mm in dimeter) is show in Figure 2.1.b . Graphene was made using CVD on copper foils in a quartz tube (25 mm in dimeter) inside a CVD furnace. The temperature was increased, followed by purging the substrate using H_2 at a flow rate of 40 sccm. After the temperature reached 1050 °C, after approximately 25 min of heating, the H_2 environment was maintained for 1 hour for cleaning the surface. The CVD graphene growth was carried out at 1050°C for 30 min with a combination of H_2 and CH_4 with a flow rate of 7 sccm and 40 sccm, respectively. After completing the graphene growth, the furnace was turn off and the sample was cooled down to room temperature while the H_2 kept flowing during the cooling whole time for protection. . The typical dimension of the CVD graphene is 1 cm x 2 cm. After CVD growth, graphene was transferred to a silicon. Poly(methyl methacrylate) (PMMA) was spin-coated on graphene, followed by baking at 120 °C for 5 min. The Cu/graphene/PMMA was then immersed (PMMA side up) in copper etchant $FeCl_3$ for about 3 hours to dissolve the Cu foil. Afterwards, the sample was rinsed/soaked in deionized water multiple times to remove residues of the copper etchant. The graphene/PMMA assemblies were then transferred onto the target SiO_2/Si substrates and left to dry overnight. The PMMA layer was removed by immersion in acetone (multiple times) and IPA, and then dried under a flow of N_2 gas. Thermal annealing at 400 °C for 30 min in mixed Ar/H_2 gases (500 sccm/300 sccm) was applied to remove residues of chemicals and polymers. The clean surface of the graphene is important to the formation of the TMD nanodiscs (N-discs) and the quality of the TMD nanodisc/graphene vdW

interface. On the clean graphene surface, the TMD solution will branch and stick on some areas, growing as an island instead of a continuous layer.

2.1.1.2 Growth of TMD Nanostructures using Vapor Transport Process

The CVD TMDs were synthesized using the thermal decomposition method that ammonium tetrathiomolybdate ($(NH_4)_2MoS_4$) or ammonium tetrathiotungstate ($(NH_4)_2WS_4$) were thermally decomposed to fabricate MoS_2 and WS_2, respectively. The $(NH_4)_2MoS_4$ precursor solution of 0.1 wt was made by dissolving a 10 mg of the $(NH_4)_2MoS_4$ or $(NH_4)_2WS_4$ powder in 10 mL of N,Ndimethylformamide (DMF). After sonication of the precursor solution for 20 min, to coat the precursor on the graphene/SiO_2/Si samples, they were first dipped in the $(NH4)_2MoS_4$ or $(NH_4)_2WS_4$) precursor solution, followed by sample spinning immediately afterwards at 3000 rpm for 1 min. The samples with coated precursor were placed in a quartz tube furnace with a mix of 10 sccm H_2 and 50 sccm Ar gas. Sulfur powder was placed in the upstream region of the quartz tube and warmed up by the emission heat of the tube furnace. The samples were annealed at 450 °C for 30 min and cooled down to room temperature. The pressure was maintained at 50 mTorr in the CVD system for MoS_2 or WS_2 growth time about 1 hour.

2.2 Preparation of the R6G Solutions of Different Concentrations

A solution of aqueous R6G of the concentration $5x10^{-5}$ M was made by dissolving solid concentrated R6G from Sigma Aldrich (Sigma Life Science) in deionized (DI) water. Droplets with lower concentration were made by diluting the concentration of $5x10^{-5}$ M further by mixing with DI water to obtain the desired concentration of the R6G. Single droplet (~10 μL) of selected concentrations were placed on the substrates and dried on hotplate at 70°C for 1 hour. . For SERS measurement, excitation lasers of 633 and 532 nm and an 20× microscope objective were used. The excitation laser beam spots are different when the excitation lasers of different wavelengths

are employed for Raman spectroscopy and imaging. For example, the laser beam spot using the 488 nm laser with a 20× microscope objective is about 10-15 mm in diameter and can be further reduced to 2-3 mm using a 100× microscope objective. The beam spot increases with the laser wavelength. It increases to 20-30 mm in diameter and 12-15 mm with 20 × and 100 x microscope objectives respectively using the 532 nm laser. Considering the spatial resolution limit of a half wavelength in the range of 244 nm to 317 nm using lasers of 488 nm to 633 nm, the step-size of 200 nm-500 nm was employed for the Raman mapping in order to achieve the spatial resolution approaching the theoretical limit. The sub-millimeter laser beam spot with a 20 × microscope objective was reasonably small allowing multiple scan locations in the center of each drop during the Raman measurement. A low intensity typically in the range of 5-10 mW and small integration time of 3 s were used to avoid damage of the R6G molecules. For better signal to noise ratio, each spectrum presented was the result of an average of several spectra taken on the same sample spot. The areal density of the molecules can be estimated from the R6G concentration, the droplet volume, and the dimension of the R6G samples on the SERS substrates. For a droplet of ~ 4-5 mm in diameter and R6G concentration of 5×10^{-5} M, the number of R6G molecules in the droplet is around 10^{12} molecules. After the R6G droplet dried, a circular spot with area of ~ 12 mm^2 was formed. The number of molecules per unit area in the spot can be estimated by dividing the number of R6G molecules in the droplet by the dried spot area. Thus, the number of molecules per unit area in the spot ~ 10^4 -10^5 molecules/μm^2 at dilution of the 5×10^{-5} M and ~ 2×10^{-2} molecules /μm^2 at dilution of the 5×10^{-12} M. With the laser beam area, the number of molecules under detection can be estimated. It should be noted that all Raman spectra presented in this work are representative based on average of multiple (typically 6-10) Raman spectra collected at spots randomly selected

on a sample to demonstrate reproducibility and consistency. The spots were selected not too close to the edge of the sample to avoid the coffee-ring effect.

2.3 Devices Fabrication and Characterization:

2.3.1 TMDs Nanodiscs (N-discs) /graphene 2D vdW Heterostructure SERS Substrate

The MoS_2 (WS_2) N-discs /graphene 2D vdW heterostructure samples were made-up in a layer-by-layer. First, graphene was synthesized on Cu and transfer to SiO_2/Si substrates as described in 2.1.1.1. For synthesis of MoS_2 (WS_2) N-discs on the graphene/SiO_2/Si substrate, the thermal decomposition method (described in section 2.1.1.2) was used. The graphene/SiO_2/Si samples were first dipped in the $(NH4)_2MoS_4$ for MoS_2 N-discs and $(NH4)_2WS_4$ for WS_2 N-discs (precursor solution (0.1 wt %) one to two times, followed by sample spinning immediately afterwards at 3000 rpm. One dipping led to a very thin coating of the precursor that segregated into nanodiscs on the hydrophobic graphene surface upon heating. The small precursor thickness typically in the range of a few nm and clean graphene surface are the key to TMD nanodiscs formation. In addition, when the dipping times were increased to four times or more, the morphology of the MoS_2 evolves from nanodiscs, mixture, and continuous layers. The best SERS was observed on single precursor dipping (MoS_2 N-discs) while it decreases drastically with increasing number of the precursor dipping.

Raman spectroscopy and Raman maps of graphene and MoS_2 (WS_2) N-discs were collected using WiTec alpha 300 confocal Raman system. The laser excitation of 488 and 532nm, and 20 × microscope objective were used for characterization of graphene and MoS_2(WS_2) N-discs. The integration time is 3 s and the laser intensity was ~1 mW. For the Raman map of TMDs 100 × microscope objective was used. Raman maps were collected at different locations (at least 4 time) on each sample. For graphene and R6G spectra with Raman signature peaks above 500 cm^{-1}, a

lower Raman spectra resolution of 5 cm^{-1} (1 point per 5 cm^{-1}) was employed using the 600 gr/mm grating. For the Raman spectra of TMD with peaks at smaller wave numbers <500 cm^{-1}, the high spectra resolution of 1.0 cm^{-1} (1 point per 1.0 cm^{-1}) was adopted using the 1800 gr/mm grating. Atomic force microscopy (AFM) on the same Witec system was used to characterize the morphology and dimension of the MoS_2 N-Discs.

A signal droplet of R6G aqueous solution (~4 mm in diameter) with the concentration in the range of 5×10^{-5} M to 5×10^{-13} M was deposited on samples. Afterwards, the samples were left to dry on a hotplate at 70 °C for 1 hour to dry the solvent and used for characterization and then the SERS measurement was taken, see section 2.1.3 for more details on the R6G preparation and SERDS measurement.

2.3.2 Intermixed WS_2+MoS_2 N-discs/Graphene van der Waals Heterostructures SERS

In order to obtain the mixed WS_2 N-discs and MoS_2 N-discs on graphene, these two kinds of the TMD-NDs were grown sequentially on graphene that was prepared on Cu sheet via CVD (section 2.1.1.1) and. MoS_2 N-discs was first synthesized on graphene, the details of the fabrication have been reported in section 2.1.1.2 and then, the same fabrication process was repeated to obtain the WS_2 N-discs on the MoS_2 N-discs/graphene samples, in the otherwise same way but $(NH4)_2MoS_4$ was used.

Figures 2.3.1 (a-f) illustrate schematically the procedure established in this work for synthesis of the WS_2N-discs+MoS_2 N-discs/graphene vdW heterostructure SERS substrate. The process includes three steps of CVD graphene growth and transfer (Figures 2.3.1 a), vapor transport growth of MoS_2NDs on graphene (Figures 2.3.1 b-c), followed with vapor transport growth of WS_2N-discs on MoS_2NDs/graphene **(**Figures 2.3.1 (d-e)). Figures 2.3.1 (f**)** shows the schematic illustration of the LSPR effect excited on the mixed WS_2N-discs and MoS_2N-discs on graphene.

It should be realized that the LSPR effect on the continuous layers of TMDs and TMD/graphene vdW heterostructures has been found negligibly small [69]. AFM system (Digital Instruments) using MSLN cantilevers with spring constants between 0.006 and 0.12 N/m (Bruker) with scan rates for approximately 3 Hz. Was used to study the morphology of the samples. Images were collected at least 3 different locations on each sample at multiple scan sizes. Particle density analysis was carried out using the Nanoscope version 1.5 offline analysis software (Bruker). Dimensional analysis was carried out by measuring the height and full-width at half maximum on at least 30 molecules. In addition, Raman system, Raman spectroscopy (using WiTec alpha 300 confocal Raman system) and SEM (LEO 1550) were used for morphological characterization of the TMDs and graphene samples.

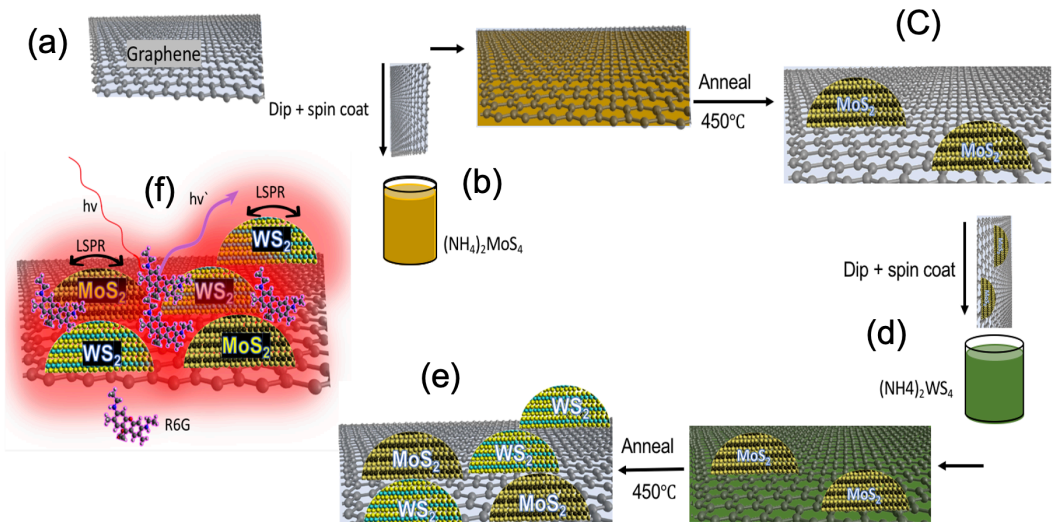

Figure 2.3.1 Schematic description of the synthesis process for the WS_2nanodiscs+MoS_2 nanodiscs/graphene SERS substrate: (a) growth and transfer of CVD graphene on SiO_2/Si substrates; (b-c) synthesis of the MoS_2nanodiscs on graphene using the vapor transport process. (b) the graphene/SiO_2/Si samples dips in the $(NH_4)_2MoS_4$ precursor solution and spins coated. (c) The annealing of the samples in Sulfur vapor in a tube furnace; (d-e): As in (b-c) for synthesis of the WS_2 N-discs on the MoS_2NDs/graphene ; and (f) the completed WS_2nanodiscs+MoS_2 nanodiscs/graphene vdW heterostructure SERS substrate.

2.3.3 Synthesis of MoS_2 Nanodonuts (N-donuts) on Graphene:

The MoS_2N-donuts/graphene 2D vdW heterostructure samples were made-up in a layer-by-layer. First, graphene was synthesized on Cu and transfer to SiO_2/Si substrates as described in 2.1.1.1. For synthesis of MoS_2 on the graphene/SiO_2/Si substrate, the thermal decomposition method (described in section 2.1.1.2) was used. In order to obtain MoS_2 N-donuts and MoS_2 N-discs, the $(NH_4)_2MoS_4$ precursor solution of low concentrations was prepared by dissolving $(NH_4)_2MoS_4$ powder in (N,N-dimethylformamide, DMF) with different concentrations of 0.06 wt%, 0.13 %wt, 0.2.wt%, 0.26 wt% and 0.4 wt. However, the low precursor concentration leads to the growth of more N-discs and the higher precursor concentration leads to the growth of more MoS_2 N-donuts. The graphene/SiO_2/Si samples were dipped in the precursor solution, followed with spinning at 3000 rpm for 30 seconds to achieve a uniform coating of the precursor on graphene. The samples were annealed afterwards in a tube furnace at~ 450 °C for 30 minutes in sulfur vapor transported by a mixed gas of H_2 (10 sccm) and Ar (50 sccm) from the sulfur powder placed upstream from the sample in a quartz tube at about 200 °C.

Figures 2.3.2 a-g demonstrate schematically the process established in this work for syntheses of graphene and the MoS_2 N-donuts and N-discs on graphene. Controlling the $(NH_4)_2MoS_4$ precursor concentration in a DMF solution was found critical to obtaining the MoS_2 of different morphologies under otherwise similar processing conditions. Indeed, MoS_2 N-discs and MoS_2 N-donuts start to grow on graphene with low precursor concentrations of 0.06 wt% depending on the precursor nuclei lateral dimension. However, with low precursor concentration the growth results in a majority of N-discs and with higher precursor concentration the majority become MoS_2 N-donuts as represented in Figure 2.3.2 d-e. (to be discussed later). This means the amount of the precursor available on the sample surface affects the nucleation and evolution of the

MoS_2 nanostructures during the MoS_2 growth. While the detailed mechanism requires further investigation, we hypothesize that the lateral and vertical dimension of the precursor nuclei formed at the initial stage of the vapor transport process may increase monotonically with the precursor concentration. This argument is supported by the increasing MoS_2 N-discs size (to be discussed later) with the precursor concentration. In fact, when the precursor concentration exceeds 0.1 wt% (multiple dips) , a MoS_2 continuous layer forms [70]. As the MoS_2 N-discs lateral and vertical sizes become large enough at 0.2 wt% or higher precursor concentrations, the conversion of the precursor to MoS_2 during the vapor transport process may become nonuniform with the conversion occurs at the edges of the nuclei first. The converted MoS_2 edge may facilitate transport of the remaining precursor at the center of the nuclei to the edge, resulting in the formation of the MoS_2 N-donuts. When the $(NH_4)_2MoS_4$ precursor concentration is low (Figure 2.3.2 f) the precursor island has a small size and vapor transport process may become more uniform and lead to more MoS_2 N-discs. Raman system, Raman spectroscopy (using WiTec alpha 300 confocal Raman system) and AFM were used for morphological characterization of the TMDs and graphene samples.

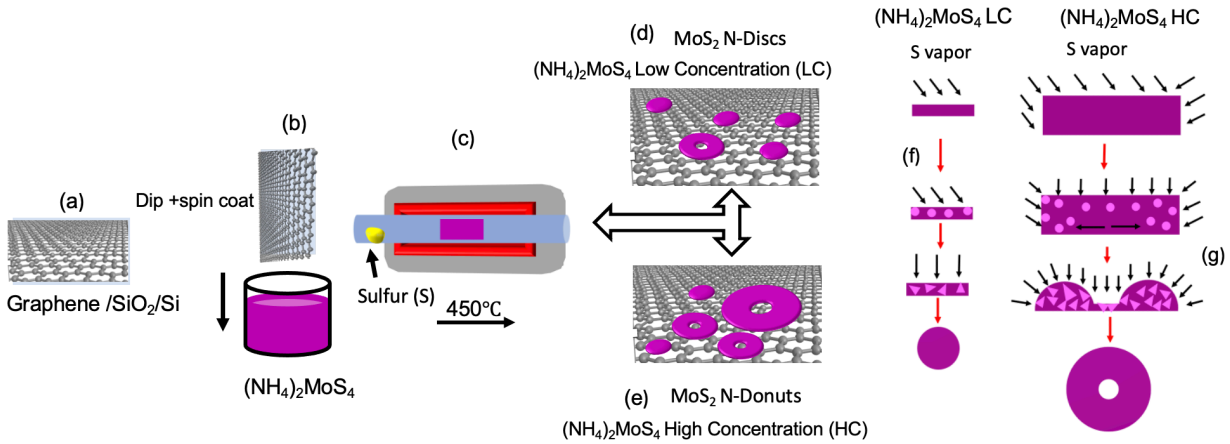

Figure 2.3.2 schematic description of the synthesis process (a) graphene transferred on SiO_2 /Si substrates via a wet transfer procedure (b-c) MoS_2 on graphene using the vapor transport process. (d) synthesis of the

MoS_2 N-Discs with low concentrations of $(NH_4)_2MoS_4$ precursor solution and (e) synthesis of the MoS_2 N-donuts with high concentrations of $(NH_4)_2MoS_4$ precursor solution. The hypothesis MoS_2 growth process with low (f) and high (g) $(NH_4)_2MoS_4$ precursor concentration.

2.3.4 AuNPs/WS_2 N-discs/Graphene van der Waals Heterostructure Substrates

In order to decorate AuNPs on the WS_2 N-discs /graphene heterostructures, electron-beam evaporation was used to coat Au of nominal thickness of 10-12 nm in high vacuum (~10^{-6} Torr at 300 °C) . The evaporation time is about ~90 seconds (growth rate of 0.11-0.13 nm/second) at the sample temperature ~300 °C [64, 71, 72]. SERS measurement, a droplet of R6G aqueous solution with different concentration was prepared and costed on the samples (see section 2.3.1 for more details on SERS measurement). Raman spectroscopy, Raman maps and AFM were used to study the morphology and characteristic of graphene and WS_2 N-discs using WiTec alpha 300 confocal Raman system. Scanning electron microscopy (SEM, LEO 1550) and dispersive x-ray spectroscopy (EDS) were used for morphological characterization of the AuNPs and WS_2 N-discs.

2.4 Simulation

2.4.1 Density Function Theory (DFT)

DFT was used to calculate the electronic structure of TMD (MoS_2, WS_2) nanodisc and graphene for more understanding of the SERS sensitivity enhancement in the TMD/graphene vdW heterostructures (chapter 3). To assess the potential charge transfer mechanism between the TMD (MoS_2, WS_2) nanodisc and graphene, the electron localization function (ELF) was evaluated using the VASP code. ELF provides a quantitative measure of the spatial delocalized bonds within the hybrid structure. Detailed atomic relaxation processes and electronic structure calculations that we employed can be found in our recent paper on hybrid nanostructures[73], but we would like to note that to account for the dispersion effect, we used vdW functional following the approach of Lion et al[74] and Roman-Perez and Soler [75] and as implemented in VASP. To assess the charge transfer mechanism, we performed the Bader Charge Analysis using the fast and efficient

algorithm developed by Henkelman's group which is also being implemented in VASP [76-78]. In addition, we also assess the potential charge transfer mechanism between the TMD nanodisc and graphene by means of the electron localization function (ELF) plots as evaluated using the VASP code. ELF provides a quantitative and normalized (range of 0-1) measure of the spatial delocalized bonds within the hybrid structures. We used the library of PAW pseudopotentials [79] as provided by VASP with the relatively high energy cut-off of 400 eV with a dense FFT-mesh of 250x250x250.

DFT[80] method was used to calculate the electronic structure of AuNPs/TMD_2/graphene 2D vdW heterostructure as obtained in Vienna *ab-initio* simulation package (VASP) (section 4.2)[81]. These hybrid systems consist of a combination of TMDs layer of MoS_2 (WS_2) and one to multi-layers of Au (111) with different thicknesses as detailed in our previous publication [71]. It is important to note that a thicker Au layer (2 monolayers or 2L, and multilayers) was found to lead to reduction of the interatomic distance due to enhanced dipole-dipole interaction and electron delocalization of TMD-NDs at the Au/TMD interface, which promote the plasmonic EM effect [71].

2.4.2 Finite Difference Time-Domain (FDTD) simulation:

In order to investigate the impact of the density of the NDs and their near field coupling on their overall plasmonic responses we carried out simulation using finite difference time domain (FDTD). This was done using Device Multiphysics Simulation Suite of Lumerical software (2020a version). For this we considered a metallic material structure model that allowed formation of LSPRs in the range of those of the WS_2 or MoS_2 nanodiscs (section 4.3). For simulation, we considered metallic nanodiscs were placed on a SiO_2 substrate while their numbers (N) or surface

densities were varied. This highlights the impact of the inter-ND coupling on the extinction spectra of the nanodiscs.

The FDTD study of the characteristic plasmonic effect was carried out to reveal the differences between MoS_2 N-donuts and MoS_2 N-discs. A commercial software package Device Mutliphysics Simulation Suite of Lumerical software (2020a version) was used. Our simulation model is mostly used to highlight how these two structures support different plasmonic field enhancement factors, defined as the ratios of the field intensities in the presence of the N-donuts and N-discs to those in their absence. Simulations were carried out considering metallic N-donuts and N-discs with difference sizes, placed on SiO_2 substrates.

FDTD simulation, the focus was to highlight the impact of the plasmonic AuNPs on the AuNPs/TMD-NDs/graphene heterostructures. Specifically, we numerically studied the interaction of light with an Au semispherical NP with a diameter of 40 nm placed on a layered structure consisting of a SiO_2 substrate covered with 5 nm of a high refractive index (n=4.4) dielectric material regarding multiple published works [82-84]. The simulation was done using the Lumerical FDTD solutions software, considering a plane wave reaching the AuNPs from the top along the z-axis. For the 5-nm dielectric materials we used Ge from the library of this software. In terms of refractive index, for the range of wavelengths considered here, i.e., ~550 nm, Ge is similar to WS_2. They have, however, different absorption, which can influence the extinction spectrum. Since the thickness of the dielectric is very small, we do expect this significantly changes the wavelengths of the plasmonic modes and their near fields.

Chapter 3: Surface-Enhanced Raman Spectroscopy based on TMDs Nanodiscs/Graphene van der Waals Heterostructure Substrates

3.1 Motivation and current research on 2D based SERS substrates

2D vdW heterostructures of graphene and TMDs may provide an unique platform for SERS due to their novel electronic and optoelectronic properties [36, 56, 85, 86]. Density functional theory (DFT) calculations have suggested that graphene could bond weakly to TMDs with weak vdW force. In the case of MoS_2, for example, a binding energy of -23 meV per C atom is predicted irrespective of the adsorption arrangement [87]. This weak TMD/graphene vdW interface could lead to an enhanced electric dipole moment and dipole-dipole interaction, facilitate effective charge transfer across the MoS_2/graphene vdW interface and therefore enhanced CM contribution to SERS [45, 88].

Nanostructured TMDs may enable LSPR upon photo-induced carrier doping with enhanced EM effect to SERS in a similar way to the LSPR quantum dots and nanocrystals [73, 89]. Motivated by this, we have developed a novel SERS substrate using a CVD process to synthesize TMD (MoS_2 and WS_2) N-discs on single-layer CVD graphene transferred on SiO_2/Si wafers to obtain the TMDs N-discs/graphene vdW heterostructure on SiO_2/Si wafers and investigated the SERS signatures of probe molecules of fluorescent R6G on these substrates.

3.2 Development of TMD nanodiscs

The Raman spectrum taken on graphene is shown in Figure 3.2.1 a with three graphene characteristic peaks: G band at ~1580 cm^{-1}, small disorder induced D band at ~1350 cm^{-1} and 2D band at ~2702 cm^{-1}. The intensity ratio of 2D to G is about 2. This, together with a negligible D peak suggest the sample is high-quality single-layer graphene. Figure 3.2.1 b shows the Raman spectrum of MoS_2 grown on top of the single-layer graphene. Besides the three graphene

characteristic peaks, two additional peaks at ~385 cm^{-1} (E_{1g}^2) and ~ 409 cm^{-1} (A_{1g}) are ascribed to MoS_2. The frequency difference between A_{1g} and E_{1g}^2 modes is about 24 cm^{-1}, indicating the MoS_2 is multilayer (up to ~ 6 layers) grown on top of the graphene [90]. In order to clarify this, Raman spectra of MoS_2 N-discs (grown) and graphene (transferred) on an Si/SiO_2 substrate were taken, from this the A_{1g} and E_{1g}^2 modes of MoS_2 have been observed at the same locations on Si/SiO_2 as on graphene, as depicted in Figures 3.2.2a. This is in contrast to a noticeable shift of the graphene peaks with TMD grown atop. Additionally, the magnitude of the MoS_2 peak shifts seem to increase with the MoS_2 layer number. It should be pointed out that an opposite trend is expected since MoS_2 with smaller layer numbers would be more affected by graphene. For a single-layer of MoS_2 grown (using CVD) on graphene[91], the peaks for the E_{1g}^2 and A_{1g} modes are shifted to ~386 and ~ 406 cm^{-1}, respectively, thus the spacing between the peaks is ~20 cm^{-1}. It has been shown that the peaks' positions and thus the spacing between them is changed as a function of the layer number[90], suggesting the Raman peak shifts for TMDs are primarily from the increased number of layers in the TMD N-discs/graphene vdW heterostructures. This argument is supported by the simulation results shown in this manuscript. The Raman signatures of $E_{1g}^2$and A_{1g} show FWHMs of about 6-9 cm^{-1}, indicating good crystalline quality, but still wider than the FWHM of exfoliated MoS_2 flakes which is about 4 cm^{-1} [92]. This indicates the presence of the growth defects in the TMDs [93, 94] (MoS_2 and WS_2 in this work) which may facilitate charge transfer or CM contribution to SERS. However, this contribution is unlikely dominant in the LSPR effect observed in TMD N-discs/graphene SERS substrates considering the significantly lower SERS sensitivity in substrates with TMD N-discs only as compared to samples with TMD N-discs/graphene. The intensity ratio of 2D to G is about 1.3, which is lower than the ratio of ~2 observed on graphene before growth of the MoS_2 and may be attributed to the interface interaction

between the MoS_2 and graphene. The intensity ratio of D to G peaks remains negligible, indicating that the graphene degradation is negligible during the MoS_2 (or TMD) growth. Figure 3.2.1d illustrate the Raman maps of graphene (G mode) and MoS_2 (A_{1g} mode) on graphene using the excitation laser of 488 nm. While the former shows a continuous distribution, the latter has a morphology of uniformly distributed islands**.** Figure 3.2.1e displays an atomic force microscopy (AFM) image of a few MoS_2 islands on graphene, which reveals the MoS_2 has a nanodisc shape with lateral dimension on the order of 200-500 nm, and the height in the range of 3-5 nm. This result is agreed with MoS_2 layer number range suggested by the Raman spectra. The optical image of MoS_2 is shown in Figures 3.2.2b, revealing the uniform distribution of the MoS_2 N-discs on graphene. A similar result has been observed on WS_2/graphene vdW heterostructures except the WS_2 signature peaks are located at 342 cm^{-1} and 412 cm^{-1} in Raman spectra.

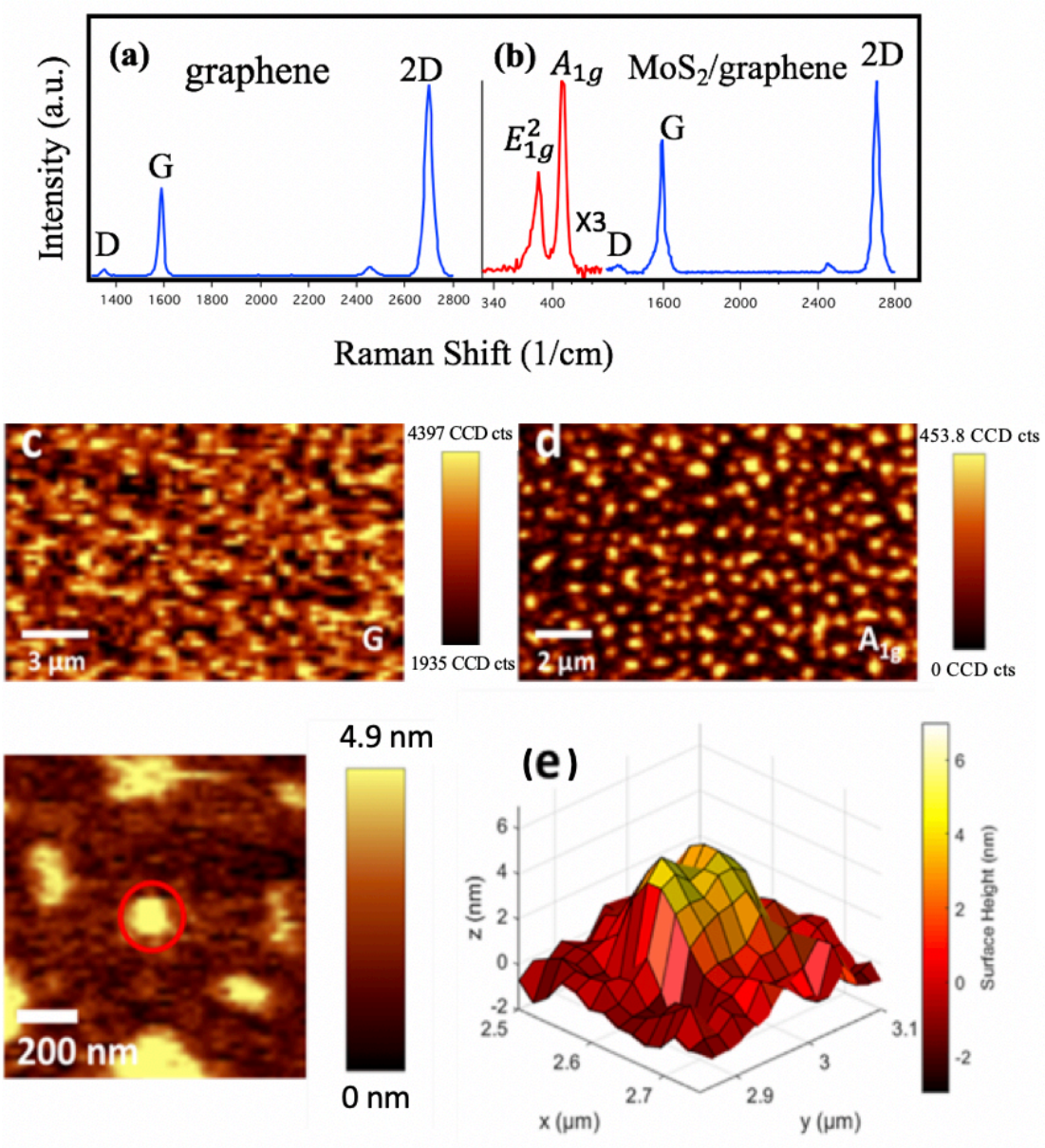

Figure 3.2.1 (a) a representative Raman spectrum of transferred graphene, with peak labels for the D, G, and 2D peaks. (b) a representative Raman spectrum of MoS_2/Graphene van der Waals heterostructure, with peak labels for the D, G, and 2D peaks from graphene and the A_{1g} and E^2_{1g} peaks from MoS_2. Spectra of graphene was multiplied by 3 to make it easier to see. (c) 18 x 14 mm^2 Raman map of graphene using G mode. (d) 15 x 12 mm^2 Raman map of MoS_2 using A_{1g} mode. The excitation wavelength of 488 nm was used. (e) AFM image of MoS_2, showing the locations and the shape of MoS_2 on the sample surface with the 3D image showing one of the MoS_2 N-discs.

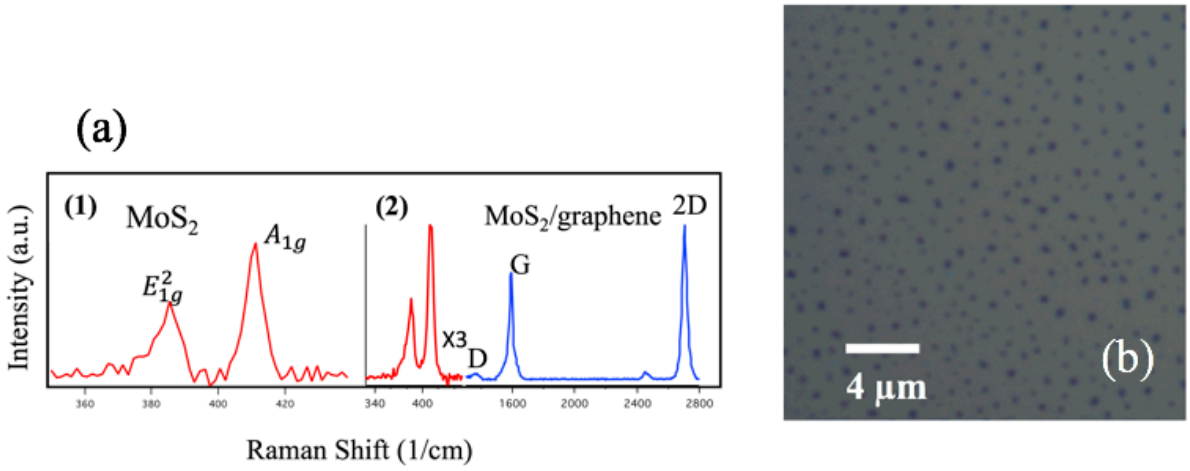

Figure 3.2.2 (a) Raman spectra of MoS_2 on Si/SiO_2 (1) and of MoS_2/graphene/ Si/SiO_2 (2). (b) Optical image of the MoS_2.

3.3 Enhanced SERS sensitivity on TMD nanodiscs/graphene

Figure 3.3.1b shows the collection of Raman spectra of R6G molecules at 10^{-5}M form 8 different spots randomly selected in the MoS_2/graphene substrate for confirmation of consistency. The intensities of the R6G peak at 613 cm^{-1} from these spectra are compared in Figure 3.3.1c with fairly reasonable consistency. A comparison of the Raman spectra of graphene without and with TMD N-discs was added as Figure 3.3.1d. The peak intensity of the graphene's Raman signature is enhanced by factor of 8-10 with the TMD N-discs compared to that of graphene only. This enhancement is similar to the LSPR by AuNPs on graphene [64] and demonstrates the LSPR effect provided by the TMD N-discs. Figure 3.3.1 a shows the comparison of Raman spectra of R6G ($5x10^{-5}$ M) on the TMD (MoS_2 and WS_2) N-discs/graphene vdW heterostructures, as well as on graphene, MoS_2, WS_2 monolayers, and bare SiO_2/Si. The excitation laser wavelength was 532 nm. The SERS enhancement is shown to depend strongly on the substrates employed for R6G molecules. On the bare SiO_2/Si substrate, R6G Raman signals (purple) are barely visible, which is expected due to the lack of SERS enhancement. Among the three single-layer substrates of

graphene (blue), MoS_2 (light blue) and WS_2 (green), the Raman R6G signature peaks are the most intensive on graphene, which is not surprising considering a more efficient charge transfer to the more conductive graphene from R6G molecules. On the other hand, this also indicates that the CM enhancement on TMD will be much less than on graphene. In stark contrast, a significant Raman enhancement of the R6G signature can be observed on the TMD N-discs/graphene vdW heterostructures. In fact, the use of MoS_2 (black) and WS_2 (red) TMDs yields a comparable SERS enhancement that is much higher than, and hence cannot be explained solely by, the combined CM effects from the constituents of TMD and graphene. By comparing the feature peak intensity of R6G at 613 cm^{-1} an enhancement factor of 7- 9 can be achieved on the MoS_2 N-discs/graphene or WS_2 N-discs/graphene vdW heterostructures with respect to the single-layer MoS_2, WS_2 or graphene reference substrates at an R6G concentration of 5×10^{-5} M.

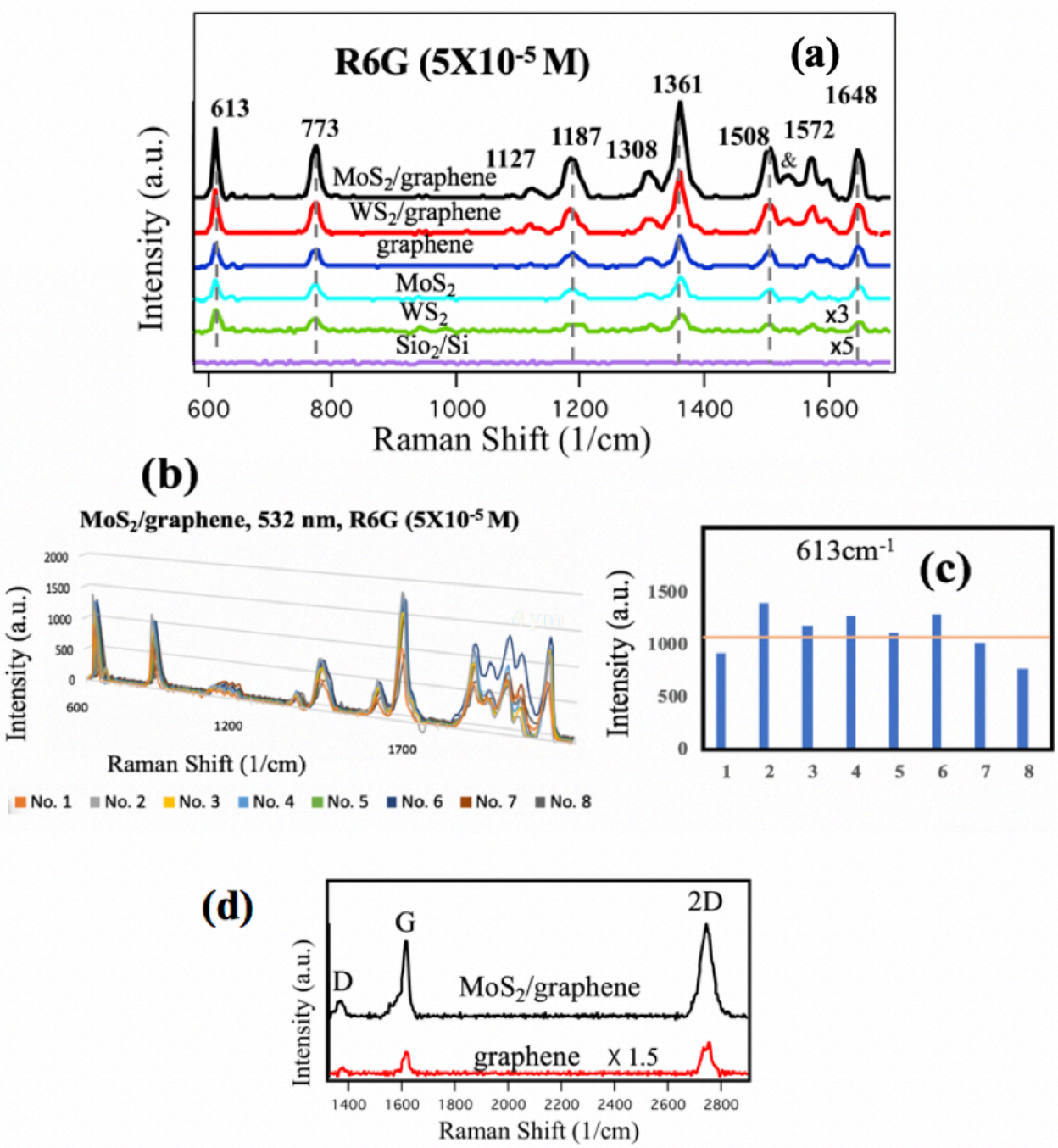

Figure 3.3.1 (a) Raman spectra of R6G molecules [5×10-5M] deposited on the MoS_2/graphene, WS_2/graphene heterostructures, MoS_2, WS_2, graphene and bare SiO_2/Si with excitation wavelength of 532 nm. Spectra on which WS_2 and bare SiO_2/Si were multiplied by 3 and 5, respectively, to make it easier to compare with the other spectra. The & mark represents the 1532 cm^{-1} of R6G. (b) the enhanced Raman spectra of the R6G molecules 5×10^{-5}M collected from 8 batches of MoS_2/graphene substrates. (c) The corresponding intensity distribution of R6G (peak 613 cm^{-1}) in the different branches from MoS_2/graphene substrates. (d) Comparison of Raman spectra of graphene with and without MoS_2 N-discs (multiplied by 1.5).

Raman spectra of R6G molecules in different concentrations were collected on both single layer (MoS_2, WS_2 and graphene) and MoS_2 (WS_2) N-discs/graphene vdW heterostructures to demonstrate SERS sensitivity using the 532 nm resonance excitation wavelength for R6G. The results on MoS_2 N-discs/graphene vdW heterostructures and on the single layers are illustrated in Figure 3.3.2a-d, while the results on WS_2 N-discs/graphene vdW heterostructures are in Figure 3.3.3. As shown in Figure 3.3.2a (for MoS_2) and 3.3.3 (for WS_2), the Raman signatures of R6G on both TMD N-discs/graphene vdW heterostructures are visible at the lowest R6G concentration of 5×10^{-11} to 5×10^{-12} M**.** This sensitivity is comparable to and slightly better than the best so far reported on the doped graphene and plasmonic metal nanostructure/graphene SERS substrates [65, 95]. It should be realized the high SERS sensitivity is unique to the TMD N-discs/graphene vdW heterostructure since the R6G sensitivities of single-layer graphene and TMD substrates are significantly lower as illustrated in Figure 3.3.2 (b-d). In fact, the Raman signatures of R6G on MoS_2 and WS_2 substrates are comparable with R6G sensitivity of around 5×10^{-6} M, which is not a surprise considering the single or few-layer semiconducting TMD (or 2DTMD) sheets do not to provide any significant EM and CM SERS enhancement. In contrast, the higher SERS sensitivity of 5×10^{-7} M R6G on the graphene substrate indicates a higher CM enhancement on graphene as compared to the TMDs due most probably to the more efficient charge transfer between R6G and graphene.

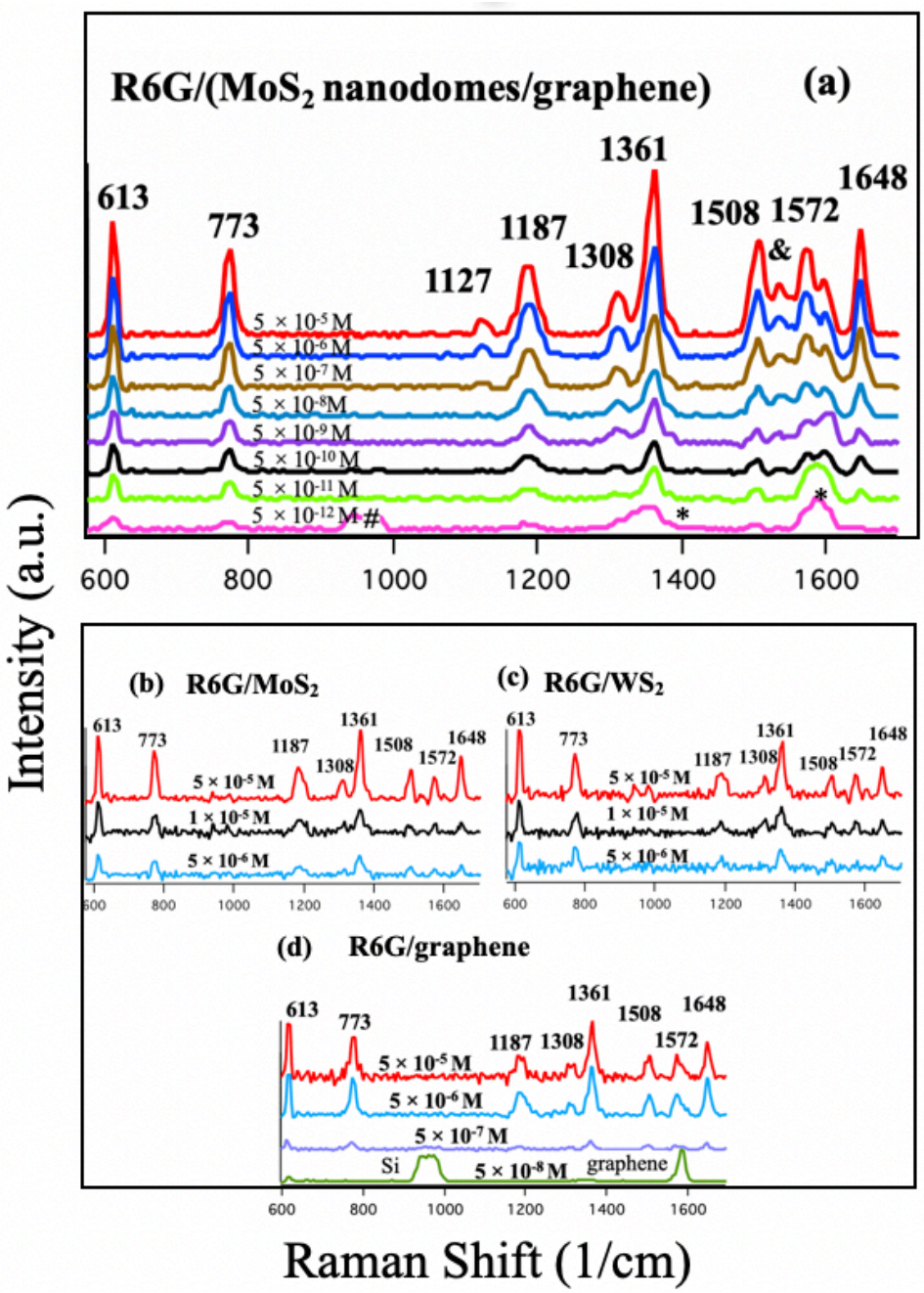

Figure 3.3.2 (a) Raman spectra of the R6G molecules with different concentrations from 5×10^{-5}M to 5×10^{-12} deposited on the MoS_2 N-discs/graphene. The marks of #, & and * denote Si peak, R6G peak at ~1532 cm^{-1} and graphene peaks, respectively. (b-c) Raman spectra of R6G molecules with concentrations from 5×10^{-5}M to 5×10^{-6} M deposited on MoS_2 and WS_2, and from 5×10^{-5}M to 5×10^{-8} M on graphene substrates, using an excitation wavelength of 532 nm.

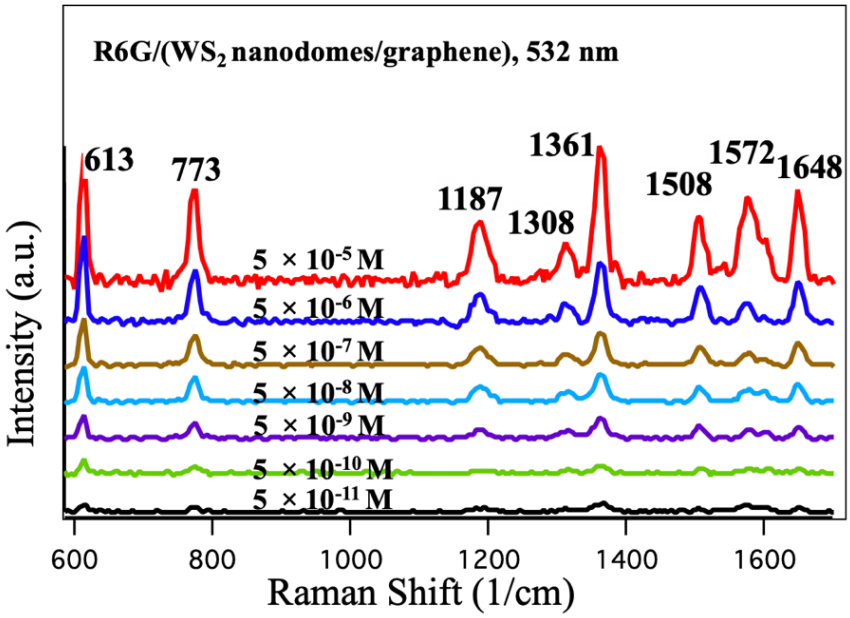

Figure 3.3.3 Raman spectra of the R6G molecules with different concentrations from 5×10^{-5}M to 5×10^{-11} M deposited on the WS_2 N-discs/graphene using excitation wavelength of 532 nm.

It should be noted that the N-discs morphology of the MoS_2 layer is critical to the high SERS sensitivity. As detailed in the Method, the morphology of the MoS_2 evolves from N-discs at one dipping of the $(NH4)_2MoS_4$ precursor solution to a continuous layer at four such dipping. The variation in the morphology of the MoS_2 layer led to a drastic decrease of the SERS sensitivity with increasing number of dipping. The MoS_2 /graphene in which the MoS_2 N-discs layer was synthesized by dipping the sample two times into the $(NH4)_2MoS_4$ precursor solution shows a similar Raman map to the one dipping sample (Figure 3.3.4 a) with of predominantly N-discs of MoS_2. However, connections of some N-discs, which leads to more nonuniform morphology and dimension of the N-discs are clearly visible. This seems consistent the reduced SERS sensitivity at ~5×10^{-11} M. Figure 3.3.4 (b-c) depict the Raman map of the MoS_2 A_{1g} mode of MoS_2/graphene samples that were synthesized with three and four precursor dippings, respectively. Patches of continuous MoS_2 layer with a small number of N-discs were obtained. Figure 3.3.4 d compares the R6G Raman signatures taken on sample (synthesized with three dippings) and the obtained

sensitivity of 5×10^{-8} M is four orders of magnitude less than that on the MoS_2 N-discs/graphene vdW heterostructures shown in Figure 3.3.2.a. Figure 3.3.5 shows the comparison of Raman spectra of R6G (5×10^{-8} M) on MoS_2/graphene vdW heterostructures with one, two, three and four precursor solution dipings. By comparing the feature peak intensity of R6G at 613 cm^{-1} an enhancement factors up to 13 can be achieved on the MoS_2 N-discs/graphene vdW heterostructures with respect to the samples with more continues MoS_2 layer (three to four dips).

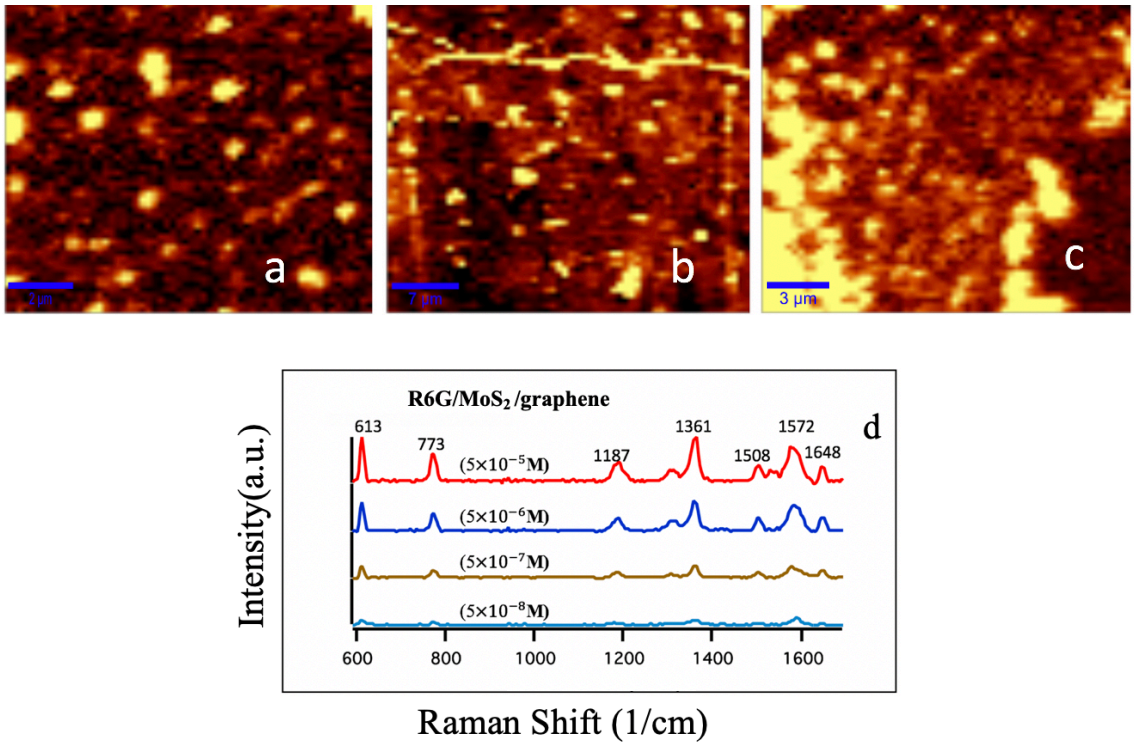

Figure 3.3.4 (a-c) A representative Raman map of MoS_2 (A1g mode) in which the MoS_2 was generated by dipping the sample two times, three times or four times, respectively, into the $(NH4)_2MoS_4$ precursor solution. (d) The Raman spectra of R6G molecules with different concentration from5×10^{-5}M to 5×10^{-8} M using an excitation wavelength of 532 nm, where the MoS_2 sample was generated by dipping into the $(NH4)_2MoS_4$ precursor solution three times.

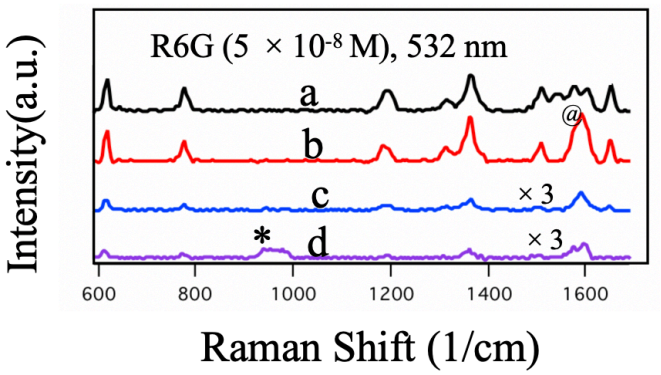

Figure 3.3.5 Raman spectra of R6G molecules 5×10^{-8}M on (a) and (b) MoS_2 N-discs/graphene (i.e. MoS_2 N-discs layer was synthesized by dipping the sample one time or two times, respectively, into the $(NH4)_2MoS_4$ precursor solution; (c) and (d) MoS_2/graphene in which the MoS_2 was generated by dipping the sample three times or four times, respectively, into the $(NH4)_2MoS_4$ precursor solution; The spectra b and c are multiplied by 3 for better visibility. *and @ are attributed to the Si and graphene peaks, respectively.

To study the SERS performance on the substrates the Raman peak of R6G at 613 cm^{-1} on single layer substrates and at 613 cm^{-1} and 773 cm^{-1} on the TMD (MoS_2 and WS_2) N-discs/graphene vdW heterostructures substrates were used to fit the Raman signatures as a function of the R6G concentration. As shown in Figure 3.3.6 and 3.3.7, an approximately logarithmic relation can be observed on all substrates which is consistent to the previous reports of SERS sensitivity employing different kinds of analyte molecules [50, 58, 96, 97]. Figure 3.3.7 (b, d, f, and h) show the linear correlation between the R6G (613 and 773 cm^{-1}) peak intensity and the logarithmic concentration of R6G on TMDs/graphene SERS substrates, which indicated a monotonic rise with the logarithmic concentration of R6G. At high concentration, the peak intensity is off the linear fitting and that was seen in previous reports of SERS [98, 99].

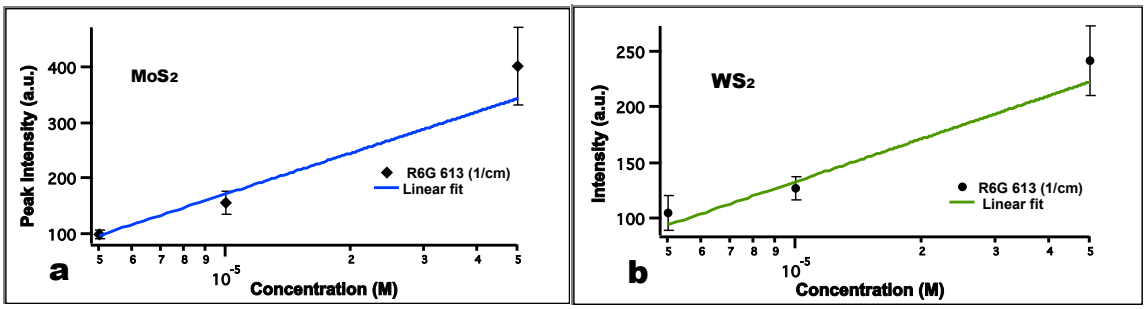

Figure 3.3.6 The intensities of the R6G Raman peaks as a function of the R6G concentrations at 613 cm-1 on the few-layer MoS_2 (a) and WS_2 substrate (b), while logarithmic scale was used for the plots with R^2~1.2.

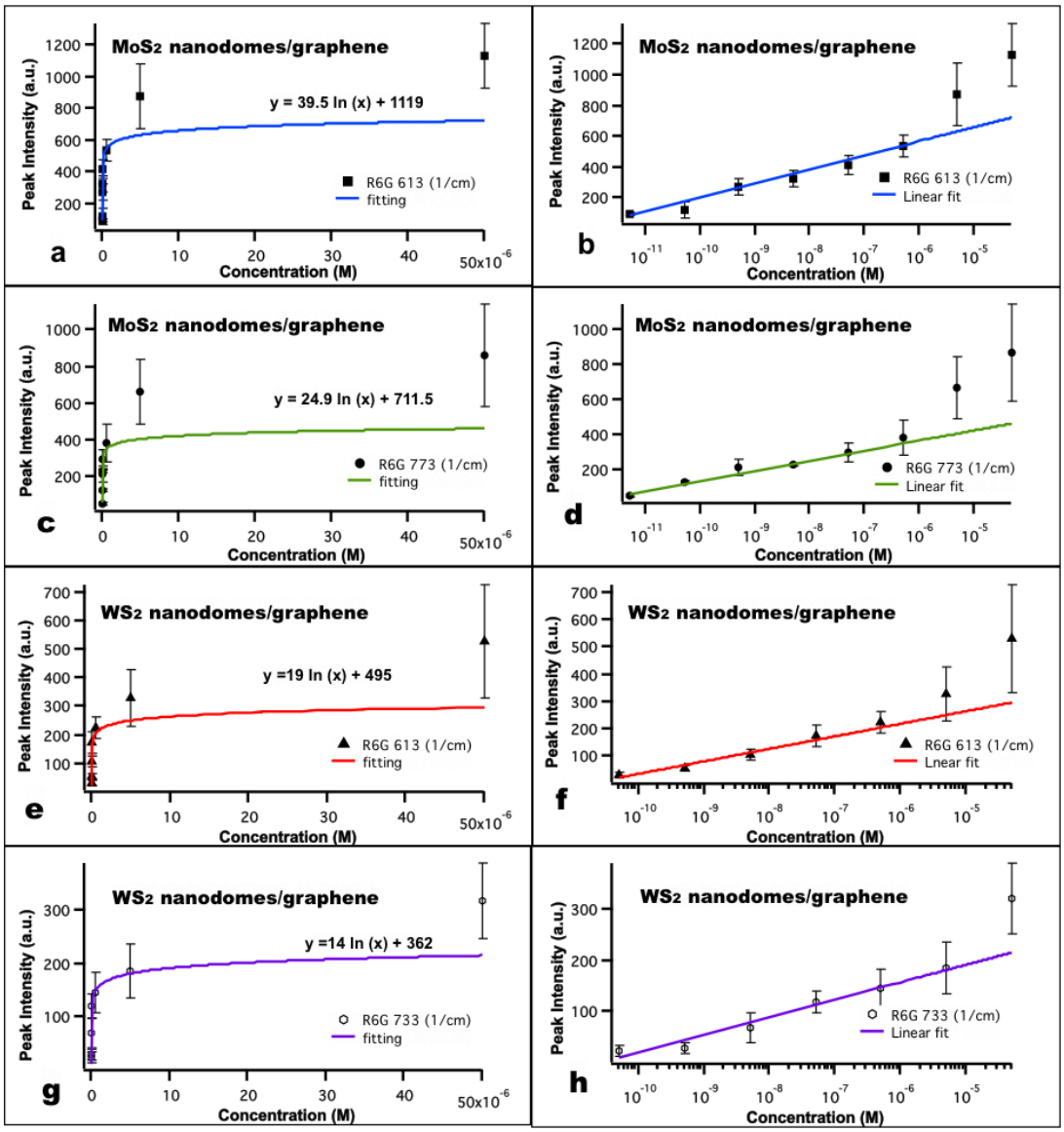

Figure 3.3.7 The intensities of the R6G Raman peaks as a function of the R6G concentrations at 613 cm-1 (a) and 767 cm-1(c), for the MoS_2 N-discs/graphene and 613 cm-1 (e) and 767 cm-1(g) for the WS_2 N-

discs/graphene vdW heterostructure substrates, while the right side plots (b, d, f, h) are the corresponding logarithmic scale plots. R^2 is in the range of 0.96 - 1.3.

The observed extraordinary SERS enhancement in the TMD N-discs/graphene vdW heterostructures indicate a unique role of the TMD N-discs decorated on the graphene. To shed some light on this, especially on the correlation between the microscopic dipole moments and dipole-dipole interactions and the SERS sensitivity enhancement in the TMD (MoS_2, WS_2) N-discs/graphene vdW heterostructures, the electronic structure of this heterostructure was calculated using density functional theory (DFT). Figure 3.3.8 a shows the final configuration of TMDs (MoS_2 and WS_2) after the ground state calculation in the ab-initio molecular dynamics simulations (AIMD) simulation. Both DFT and AIMD simulations show the TMDs remain stable in single-layer and few-layer forms. We then proceeded by relaxing the position of the TMD N-discs onto the graphene. The graphene is comprised of 288 atoms for a placement of a MoS_2 N-discs for a total of 324 atoms (Figure 3.3.8 b). Figure 3.3.8 c depicts a sectional portion of the MoS_2 N-discs in contact with the graphene. The contour color level indicates the degree of delocalized electrons. As expected in the graphene due to the covalent C-C bond, the electrons are highly delocalized between C atoms. However, delocalization can also be observed in areas between the sulfur atoms in TMD and the carbon atoms on graphene as evident by the similar color contour. This suggests that even though, in general, the dominant mechanism of chemical bonding remains the relatively weak vdW interaction, there is an observed charge redistribution between the graphene and the TMD in the TMD/graphene vdW heterostructures, which may allow us to further tune the vdW interaction. Certainly, the large reported work function between graphene (4.51 eV) and MoS_2 (5.52 eV) must have further aided the ease in charge transfer between the two structures. To further assess this mechanism and the stability of the structure, we also evaluated and compared the total cohesive energy of the TMD/graphene vdW heterostructures between a structure wherein the TMD

N-discs is placed close to the graphene (-2851.1328 eV) versus one where the N-discs is located far from the graphene (-2853.5725 eV). The energy comparison and the energy difference indicate a favorable gain in cohesive energy through the adsorption of the TMD nanodisc, which can be attributed to charge transfer.

It should be noted that Xu *et al* [100] reported a theoretical work in evaluating the bonding mechanism in a variety of multilayer hybrid systems including a bilayer of MoS_2 and graphene. The work also suggested that by tuning the vdW interaction through the enhanced charge transfer, one can further enhance the optical adsorption mechanism [100]. On the other hand, Joo *et al* investigated a variety of organic dipolar molecules dispersed on graphene and reported the enhanced molecule/graphene interface dipole-dipole interactions in turn yield enhanced SERS [101].

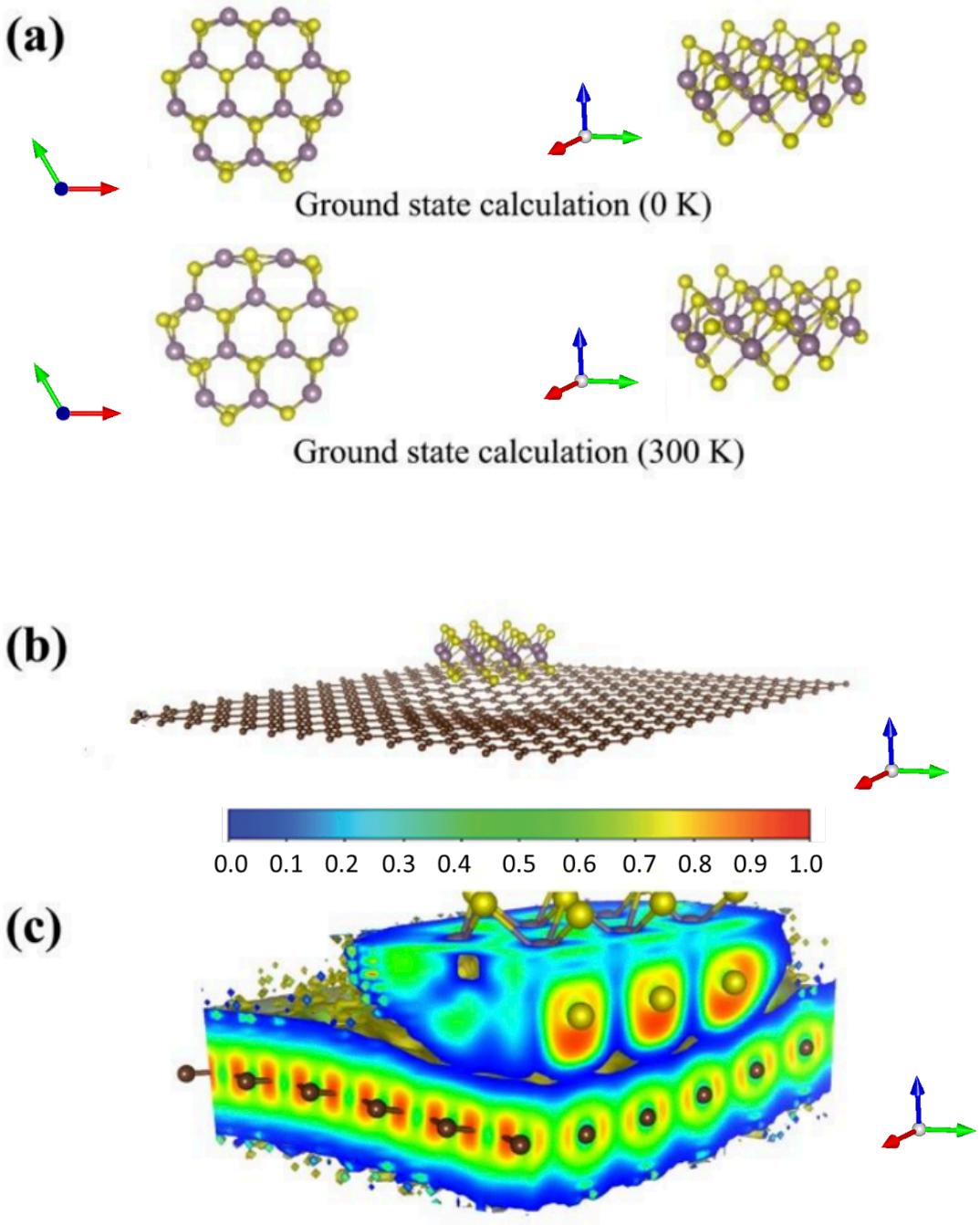

Figure 3.3.8. (a) Monolayer MoS_2 N-discs after both the ground state calculation at 0K and after AIMD simulation at 300K. Both show stable configurations. (b) Vertical MoS_2/graphene bilayer heterostructure. (c) Electron Localization Function (ELF) of the MoS_2/graphene bilayer heterostructure showing the localized electron concentration below the sulfur atom indicating the charge transfer occurrence.

Based on the insights gained from the simulation, we propose a photo-doping LSPR mechanism on TMD N-discs/graphene vdW heterostructures. As schematically depicted in Figure 3.3.9, the enhanced dipole-dipole interaction and charge transfer across the TMD/graphene vdW interface is critically important for the LSPR to be excited and sustained on TMD N-discs as the free carriers are excited to the conduction band upon optical excitation. This is very similar to the Au nanoparticle/graphene nanohybrid case for enhanced SERS with both contributions from CM and EM effect. The morphology of the TMD N-discs enables localization of the plasmonic resonance and therefore the LSPR to be generated without any metal plasmonic nanostructures. We argue that the metal-free TMD N-discs/graphene vdW heterostructures may provide unique advantages on the matching LSPR resonance frequency via the electronic structures of the TMDs. In fact, some differences have been observed in the metal-free TMD N-discs/graphene vdW heterostructures as compared to their metal nanostructure/graphene counterparts. First, both electrons and holes can participate in the LSPR in semiconductor TMD N-discs/graphene since free electrons and holes are generated simultaneously upon light excitation as shown Figure 3.3.9. This may lead to more efficient plasmonic resonance or a reduced Ohmic loss due to the high carrier mobility in semiconducting TMD N-discs. As we have mentioned earlier, the R6G SERS sensitivity up to $5x10^{-12}$ M on the TMD N-discs/graphene vdW heterostructures is comparable and slightly better than the best so far achieved on metal nanostructures/graphene SERS substrates. On the other hand, the LSPR frequency in semiconducting TMD N-discs/graphene is expected to be broadband similar to the plasmonic semiconductor quantum dots and nanocrystals [73, 87]. This is supported by the much smaller difference of only 1-2 orders of magnitude between the resonance (10^{-11}-10^{-12} M at 532 nm excitation) vs. non-resonance (10^{-10} M at 633 nm excitation) SERS sensitivities of R6G observed on the TMD N-discs/graphene vdW heterostructures, rather than the

3-4 orders of magnitude difference on Au nanoparticles/graphene SERS substrate counterparts. This is particularly important for molecule sensing, since resonance SERS may not be possible for most molecules due to the limited availability of excitation laser frequencies.

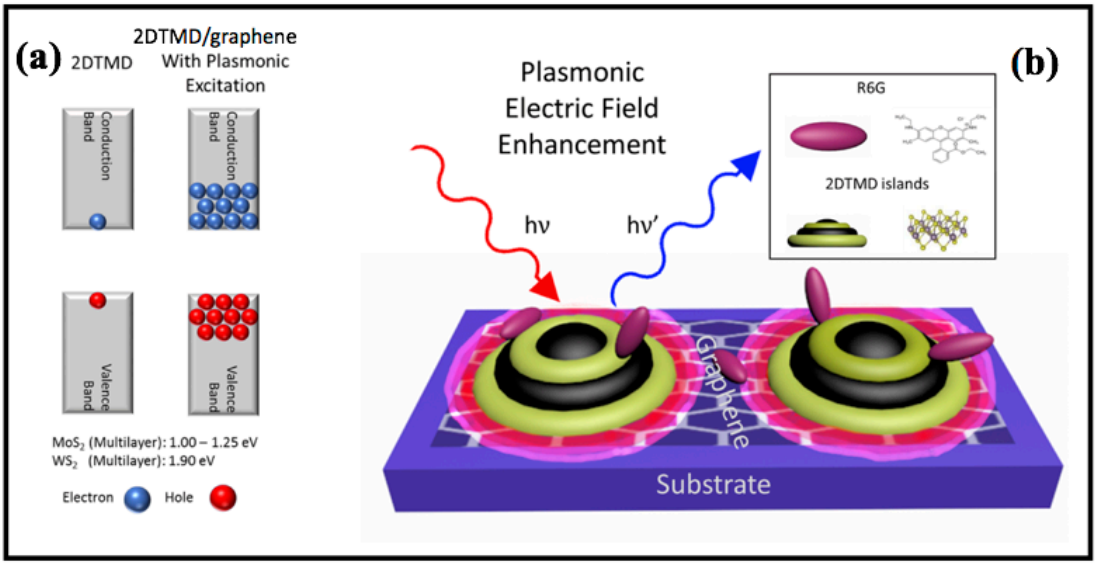

Figure 3.3.9 (a)Schematic representation of electron–hole pairs of few-layer TMDs (2DTMD)/graphene vdW heterostructure showing enhancing Raman scattering due plasmonic excitation in TMD multilayers. (b) Diagram of TMD N-discs/graphene vdW heterostructures on SiO_2 is 90 nm, with R6G molecules covering the substrate, showing enhancing Raman scattering due to possibly electromagnetic enhancement (EM) and chemical enhancement (CM). The black and green toroids represent the transition metal element (Mo, W) and chalcogen (S).

3.4 Conclusion

In summary, we have developed a novel SERS substrate of TMD (MoS_2 and WS_2) N-discs /graphene. This metal-free TMD N-discs/graphene vdW heterostructures provide a high-performance SERS substrate with EM and CM enhancement, both are associated with the strong dipole-dipole interaction at the heterostructure interface as indicated by the DFT and AMID simulations. On R6G probe molecules, an extraordinary SERS sensitivity up to 10^{-12} M was obtained using TMD N-discs/graphene vdW heterostructure substrate. Importantly, the SERS sensitivity of TMD N-discs/graphene vdW heterostructures is 4-5 orders of magnitude higher than

that of the single-layer MoS_2, WS_2 or graphene substrates. A remarkably high SERS sensitivity in the range of 5×10^{-11} M to 5×10^{-12} M were obtained on these TMD nanodiscs/graphene vdW heterostructure SERS substrates, which is not only several orders of magnitude higher than that of single-layer graphene, MoS_2 and WS_2 SERS substrates, but also comparable to and slightly better than the best sensitivity reported so far on the plasmonic metal nanostructure/graphene SERS substrates [65, 95].This enhancement drops significantly when the TMD N-discs are replaced with a continuous TMD layer on graphene, indicating the TMD dimension and shape are highly relevant. Besides, the peak intensity of graphene's Raman signature with TMD N-discs is enhanced by factor of 8-10 as compared to that of graphene only, demonstrating the LSPR effect provided by the TMD N-discs. Based on these observations, we attribute the high SERS sensitivity to the combination of the CM enhancement due to the enhanced dipole-dipole interaction at the TMD/graphene interface and the EM enhancement through the LSPR on the photo-doped TMD N-discs/graphene [73, 89, 102, 103]. This result illustrates a new pathway in designing high-efficiency metal-free SERS substrates by engaging 2D vdW heterostructures that combine the superior and complementary optical and electronic properties of the constituent atomic layers.

Chapter 4: Improving the TMDs density for Surface-Enhanced Raman Spectroscopy based on intermixed WS_2 and MoS_2 nanodiscs

After the exciting SERS sensitivity and enhancement that has been achieved on developing non-metallic TMDs N-discs/graphene that may have caused by EM +CM enhancement and since these EM effect depends on the density of nanoparticles, several attempts has been done in this work to improve the density of TMDs N-discs. We have tried several ways to control the density of one kind of TMD NDs, such as using consecutive coatings of the same TMD or dipping the samples serval time in the $(NH_4)_2MoS_4$ or $(NH_4)_2WS_4$ precursor solation. Disappointingly, the additional coating of the same TMD material seems to only lead to larger NDs with reduced SERS sensitivity. Therefore, the purpose of this work is to exploit the ways to achieve high TMD N-discs density and to probe the effect of the TMD N-discs density on SERS sensitivity. In fact, maxing two kind of TMDs (WS_2+MoS_2) lead to SERS substrates with higher ND density with similar size, resulting in strong SERS effect compare to one kind of TMDs.

4.1 Enhanced SERS sensitivity on TMD on intermixed WS_2 and MoS_2 N-discs/Graphene

Figure 4.1.1a shows a Raman spectrum of the TMD-NDs in a representative WS_2N-discs +MoS_2 N-discs/graphene sample using Raman excitation at 488 nm. Four peaks on the spectrum can be indexed to the A_{1g} at ~384 $cm^{-1}$and E_{2g}^1 at ~409 cm^{-1}modes of MoS_2, and A_{1g} at ~367 $cm^{-1}$and E_{2g}^1 at ~424 cm^{-1}modes of WS_2 respectively, confirming that both WS_2 and MoS_2 were obtained in the WS_2N-discs+MoS_2 N-discs/graphene sample.

The observation of the signature peaks for crystalline MoS_2 and WS_2 from the Raman spectrum in Figure 4.1.1a is consistent with that observed on MoS_2/graphene heterostructures bilayers made using the same processing condition [104]. In the latter case, a further confirmation

of the crystallinity of stoichiometric MoS_2 (or WS_2) was provided using X-ray photoelectron spectroscopy (XPS) in our prior work [104]. While a precursor layer of a much smaller thickness (by reducing the precursor concentration) was employed in this work to facilitate formation of MoS_2 (WS_2) nanodiscs as compared to that for the continuous layer counterparts, this morphological difference is unlikely to result in differences in the crystallinity and phase under the same processing condition for MoS_2 (or WS_2) ND layer growth in vapor transport process as confirmed in the Raman spectra and mapping. In fact, Raman spectroscopy and mapping have been adopted widely and conveniently to confirm the phase, crystallinity, and morphology of 2D atomic materials including TMDs nanostructures [104-108]. Figure 4.1.1b shows the Raman A_{1g} peaks map for MoS_2 and WS_2 together (since the two A_{1g} peaks are very close to each other) and illustrates the TMD-NDs morphology for the WS_2N-discs and MoS_2NDs. It should be noted that the small precursor coating thickness and low precursor concentration are the key to obtaining the TMD-NDs morphology [69]. At higher precursor concentrations or larger precursor thicknesses, TMD continuous layers would form. Multiple coatings of the low concentration precursor would increase the TMD-ND concentration together an increased dimension of the previously formed NDs and leads to a continuous TMD layer after about 3-4 coatings [69]. Figure 4.1.1c-d exhibit the Raman maps of the WS_2 (E_{2g}^1 mode) and MoS_2 (E_{2g}^1 mode), respectively. The contrast in the brightness demonstrates clearly that most WS_2N-discs and MoS_2NDs are located at different locations in the WS_2N-discs+MoS_2 N-discs/graphene samples, instead of being on top of each other. This is different from repeating the growth process for the same kinds of the TMD-NDs, which results in larger dimension of NDs and eventually a continuous TMD layer [69]. It should be pointed out that differences are present on the concentrations and dimension of the two types of NDs. Based on Figure 4.1.1c, the WS_2 N-discs have the average concentration of $0.55/\mu m^2$ and

lateral dimension of 500 nm -1.0 mm. In contrast, the MoS_2 N-discs shown in Figure 4.1.1d have the average concentration of $1.3/\mu m^2$ and lateral dimension of 300-500 nm. It should be noted that WS_2 N-discs were fabricated after the completion of the MoS_2 N-discs. The observed lower concentration and larger dimension of the WS_2 N-discs suggests that the nucleation of the WS_2 N-discs is affected by the presence of the formed MoS_2 N-discs on the sample. In comparison with the Raman map of the MoS_2 and WS_2 together using their A_{1g} peaks (Figure 4.1.1b), it seems that they unlikely grow in continuous layer or on top of each other, which means a higher TMD-ND areal density (by a factor of > 3 approximately in the range of 1.4-3.7/μm^2 would be obtained in the WS_2N-discs+MoS_2 N-discs/graphene sample as opposed to the WS_2N-discs/graphene and MoS_2NDs/graphene samples with only one kind of the TMD-N-discs. Figure 4.1.1e-f display the SEM images taken on a representative WS_2 + MoS_2 N-discs/graphene heterostructure sample at different magnifications. The formation of N-discs of irregular shapes (approximately spherical) can be confirmed. The lateral dimension of the MoS_2 and WS_2 N-discs is varied within the range of 200 nm-500 nm. Besides the larger nanodiscs, many smaller nanoparticles with dimension << 100 nm can be seen also in the SEM images and these particles distribute fairly uniformly across the sample. Samples prepared by deposition of the MoS_2 and WS_2 in different order (WS_2N-discs on MoS_2ND/graphene and MoS_2NDs on WS_2 N-discs/graphene were imaged by AFM. Representative images of the samples at two different sizes ($10 \times 10\ \mu m^2$ and $5 \times 5\ \mu m^2$) are shown in Figure 4.1.2a-b along with a magnified image of an individual nanodisc with a cross-sectional profile through the feature as indicated by the blue line in the illustrations. The images show a variety of features on the surface, but most features are round with a disk-like shape with a depression in the middle, almost a donut shape. These types of features are consistently observed on each sample. It is likely that the distinct ring like features (raised rings in the domes) are the

result of the dynamics of the particle motion during the solvent evaporation. The two types of samples show very similar density and size of features, regardless of order of deposition (Table. 4.3.1). A density of approximately 1.3 $\frac{particles}{\mu m^2}$ was observed on both types of surfaces, which is approximately twice of that of WS_2N-discs (or MoS_2N-discs) on graphene. The average width of the features was ~350 nm with a height of ~7-8 nm. The results show that there is very little difference overall density and sizes of the features. This is consistent with the consistent SERS enhancement observed on these two types of SERS substrates. Finally, it should be noted AFM measurement on graphene samples made with the same CVD protocol as in this work has confirmed the single-layer graphene[109], which is consistent to the Raman and SEM results shown in Figure 4.1.1.

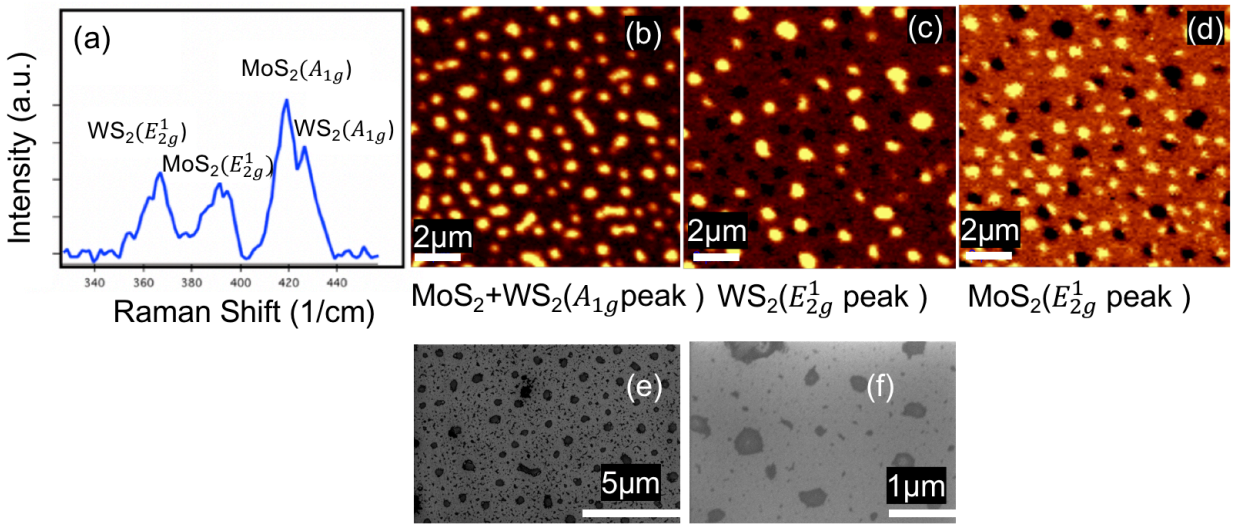

Figure 4.1.1 (a) Raman spectrum of WS_2N-discs+MoS_2 N-discs/graphene in the low wavenumber range. Raman maps of (b) the A_{1g} peaks for MoS_2NDs and WS_2N-discs, (c) the WS_2 ($\boldsymbol{E^1_{2g}}$ mode), and (d) the MoS_2 ($\boldsymbol{E^1_{2g}}$ mode). A Raman excitation laser of 488 nm was used. (e) the SEM image of the sample of WS_2N-discs+MoS_2 N-discs/graphene and (f) represents zoomed in feature.

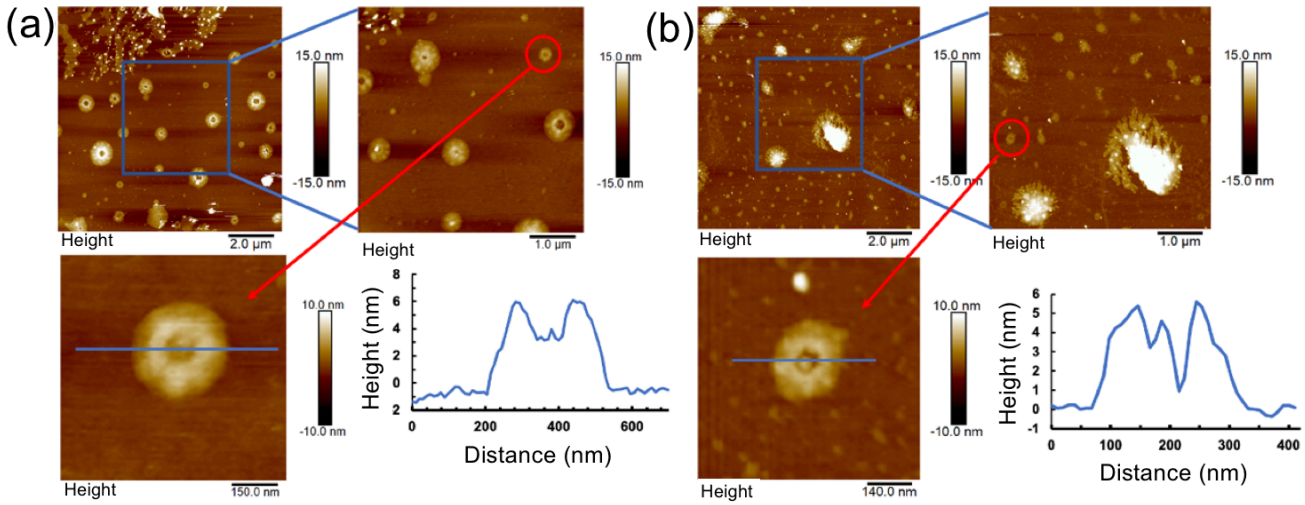

Figure 4.1.2 (a) Top: Sample of WS_2N-discs+MoS_2 N-discs/graphene contact mode AFM images, (left)$10 \times 10\ \mu m^2$ and (right, area in blue box on left) $5 \times 5\ \mu m^2$. Lower panel shows a representative zoomed in feature (in red circle in upper panel) along with a cross-sectional profile through the center of the feature (blue line). (b): As in (a) for sample MoS_2NDs+WS_2 N-discs /graphene.

Figure 4.1.3a displays the Raman spectra taken on three samples of pristine graphene only (red) (inset), MoS_2NDs/graphene (blue) and WS_2N-discs+MoS_2 N-discs/graphene (black), on which three peaks of D, G and 2D modes are all indexed to graphene. The G peak at ~1587 cm^{-1} and the 2D peak at ~ 2695 cm^{-1} are clearly observable on all three samples. The D peak at ~1356 cm^{-1} is because of the defect in graphene [54]. On pristine graphene, the intensity ratio of 2D peak to G peak is around 1.9, which is anticipated for the monolayer graphene. The intensity ratio of D to G is negligible (around 0.04), confirming high quality of graphene. The graphene's signature peaks exhibit some quantitative changes after TMD-NDs were grown on graphene. For example, the intensity of D peak increased so that the radio of D to G is about 0.4 and that can be caused by the damage of the exposed to S vapor. Furthermore, the (2D/G) relative intensity is obviously reversed and the location of the G peak is shifted slightly. In fact, the G peak and 2D peak intensities for graphene are significantly enhanced with the decoration of the plasmonic MoS_2NDs

(blue) and the plasmonic WS_2N-discs+MoS_2 N-discs (black). On the MoS_2NDs/graphene samples, the enhancement factor of the graphene G peak is 7.4, while on the WS_2N-discs+MoS_2 N-discs the enhancement of G and 2D peaks of graphene further improved to 14 which are similar to previously reported works on plasmonic metal nanostructures/graphene [64, 110, 111]. The enhancement of the graphene signature peaks in the WS_2N-discs+MoS_2 N-discs/graphene sample is most probably due to the LSPR effects superposition from the WS_2N-discs and MoS_2N-discs. Figure 4.1.3b compares the representative optical absorption spectra in the wavelength range of 300-900 nm taken on the MoS_2NDs/graphene (blue), MoS_2N-discs+MoS_2 N-discs/graphene (green) made with two coatings of the same precursor, and WS_2N-discs+MoS_2 N-discs/graphene (black) samples on glass substrates. The MoS_2NDs/graphene sample has the lowest absorption while the WS_2N-discs+MoS_2 N-discs/graphene, the highest. The fact that the absorption in the WS_2N-discs+MoS_2 N-discs/graphene sample is higher than that of the double-coating MoS_2NDs/graphene one is anticipated from the higher N-discs concentration in the former. This demonstrates the benefit of the mixed WS_2N-discs+MoS_2 N-discs to prevent formation of large TMD patches with diminishing LSPR effect with the increasing patch dimension [69]. The absorption spectra of the three samples show two broad shoulders at ~ 400-450 nm and 550-600 nm respectively, which may relate to the broad size distribution of the NDs and their thickness in the range of 3-5 nm[69, 112].

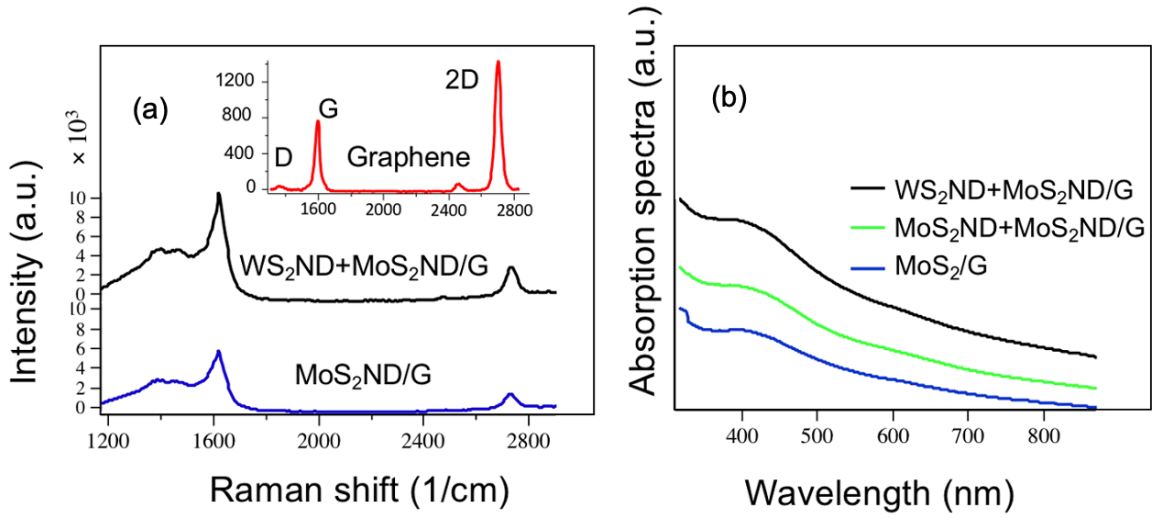

Figure 4.1.3 Raman spectra of a pristine graphene (red, inset), MoS_2NDs/graphene (blue), and WS_2ND+MoS_2ND/graphene (black) using 488 nm laser of power of 1 mW. (b) Optical absorption spectra of WS_2ND+MoS_2ND/graphene (black), MoS_2ND+MoSNDs/graphene (green, made with double coating of the MoS_2ND) and MoS_2ND/graphene (blue).

Figure 4.1.4 a compares the Raman spectra of R6G ($5x10^{-5}$ M) probe molecules on MoS_2 N-discs+WS_2 N-discs/graphene (purple curve, using growth sequence of MoS_2NDs/WS_2N-discs/graphene) and WS_2N-discs+MoS_2 N-discs/graphene (black curve, using growth sequence of WS_2N-discs/MoS_2N-discs/graphene) and MoS_2ND_S/graphene heterostructures (blue), and graphene. The Raman excitation wavelength is 532 nm. In addition, the R6G SERS spectrum taken on an AuNPs/WS_2N-discs/graphene (green) is also included since this sample also contains two plasmonic nanostructures: metallic AuNPs and non-metallic WS_2N-discs. A series of R6G Raman signature peaks can be identified on all four spectra. Specifically, the spectra include the R6G major peaks at 613 cm^{-1} assigned to the C–C–C ring in-plane vibration mode, 773 cm^{-1} assigned to aromatic C–H bending mode, the 1190 cm^{-1} assigned to C–O–C stretching mode and 1361 cm^{-1}, and 1648 cm^{-1} assigned to the C–C stretching mode, respectively [15, 113]. Among the five spectra, graphene has the lowest R6G peak intensity, indicative of the lowest SERS enhancement

due to the CM only. As revealed in Figure 4.1.4a, the SERS enhancement of the R6G Raman signatures on the MoS_2N-discs+WS_2 N-discs/graphene (purple curve, using growth sequence of MoS_2N-discs/WS_2N-discs/graphene) and WS_2N-discs+MoS_2 N-discs/graphene (black curve, using growth sequence of WS_2N-discs/MoS_2N-discs/graphene) are both considerably greater than the one on the AuNPs/WS_2N-discs/graphene (green curve), MoS_2NDs/graphene (blue curve) and graphene (or G, red curve). In order to quantify the enhancement, the ratios (R) of the 613 cm^{-1} peak intensity on the MoS_2N-discs+WS_2 N-discs/graphene, WS_2N-discs+MoS_2 N-discs/graphene, AuNPs/WS_2N-discs/graphene, and MoS_2NDs/graphene, to that on graphene (G) were calculated to be 17.3, 16.4, 12.2, and 8.1, respectively (Figure 4.1.4b). Interestingly, the SERS enhancement factors on the WS_2 N-discs+MoS_2 N-discs/graphene and MoS_2 N-discs+WS_2 N-discs/graphene are comparable, while they are a factor of ~2.0 higher than that on the MoS_2 N-discs (WS_2N-discs)/graphene. In addition, TMD N-discs seem to provide stronger SERS effect than the metallic AuNPs, making them appealing for low-cost, large-scale applications. This observed SERS enhancement demonstrates the advantage of the superposition of the LSPR effects from the WS_2 N-discs and MoS_2NDs on graphene vdW heterostructures. In addition, the enhancement factor of the R6G 613 cm^{-1} peak on WS_2N-discs+MoS_2 N-discs/graphene is 34% higher than that on the AuNPs/WS_2 N-discs/graphene, illustrating the non-metallic SERS substrates based entirely on the 2D atomic materials can provide better performance than their counterpart based on mixture of TMD and Au plasmonic nanostructures.

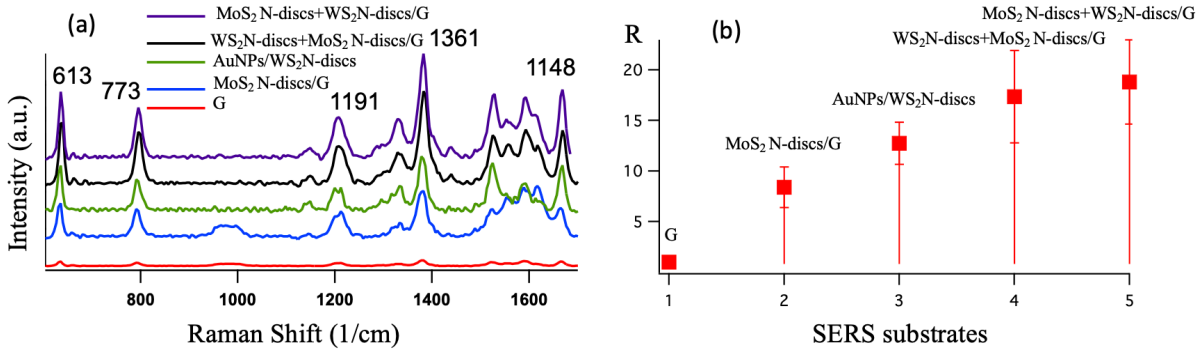

Figure 4.1.4 (a) Raman spectra of R6G molecules at the concentration of 5×10^{-5}M deposited on MoS_2N-discs+WS_2 N-discs/graphene (purple), WS_2N-discs+MoS_2 N-discs/graphene (black), AuNPs/WS_2N-discs/graphene (green), MoS_2N-discs /graphene heterostructures substrates (blue) and graphene (G, red) with 532 nm excitation. (b) The ratio (R) of the 613 cm^{-1} R6G peak intensity to the same peak on graphene of the SERS substrates of graphene (column 1), MoS_2NDs/graphene (Colum 2), AuNPs/WS_2N-discs/graphene (Column 3), WS_2N-discs+MoS_2 N-discs/graphene (Column 4), and MoS_2N-discs+WS_2 N-discs/graphene (Column 5).

Furthermore, a sample of MoS_2ND/graphene (made with two consecutive coatings) was synthesized to obtain a SERS substrate, attempting for a higher density of TMD NDs for further enhanced SERS substrate. Figure 4.1.5a-c compare the Raman maps of the MoS_2NDs/graphene samples with one MoS_2ND coating (a), two consecutive MoS_2ND coatings (b), and intermixed WS_2 N-discs+MoS_2 N-discs/graphene sample, revealing that adding multiple coatings of the same kind of TMDs, such as MoS_2, would primarily lead to larger NDs towards a continuous layer when MoS_2 N-discs overlap. The comparison of the Raman spectra of R6G molecules at the concentration of 5×10^{-5}M on the three substrates of MoS_2NDs/graphene (blue), MoS_2NDs+MoS_2 N-discs/graphene (green), and WS_2N-discs+MoS_2N-discs/graphene (black) is shown in Figure 4.1.5 d, illustrating that the R6G SERS enhancement on the MoS_2N-discs+MoS_2N-discs/graphene is lower than that on the MoS_2N-discs/graphene and MoS_2N-discs+MoS_2 N-discs/graphene. By comparing the R6G's 613 cm^{-1} peak intensity with respect to that on the MoS_2N-discs/graphene reference substrate (Figure 4.1.5e), the enhancement factor of ~ 2.0 can be reached on the

WS_2ND+MoS_2 N-discs/graphene while it is only 0.8 on the MoS_2ND+MoS_2ND/graphene. This result demonstrates intermixing different TMD NDs, such as MoS_2N-discs+MoS_2 N-discs/graphene provides a promising process to achieve high density TMD NDs for further enhanced SERS sensitivity.

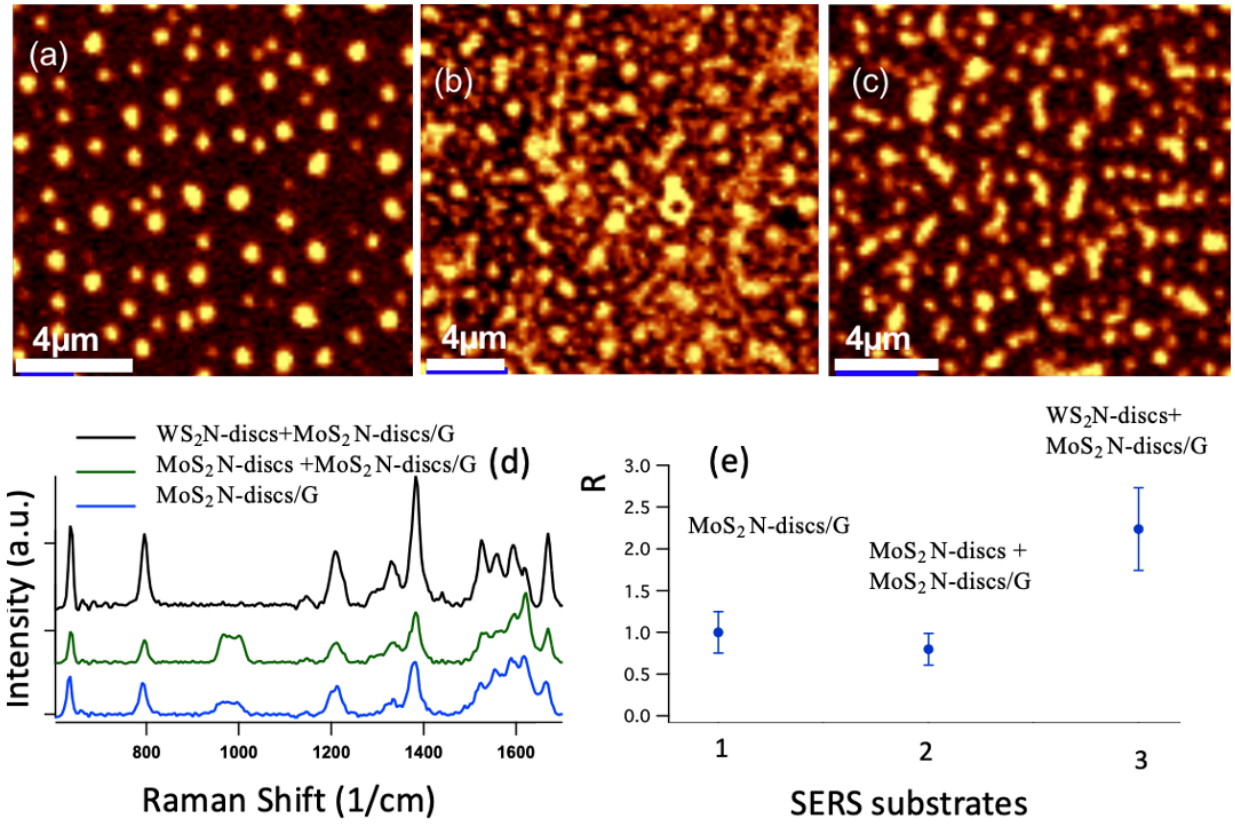

Figure 4.1.5 (a) A representative Raman map of MoS_2 (A_{1g} mode) of MoS_2NDS/graphene, (b) A representative Raman map of MoS_2 (A_{1g} mode) of oS_2N-discs+MoS_2N-discs/graphene sample, (c) Raman maps of MoS_2NDs and WS_2N-discs (A_{1g} mode) of WS_2N-discs+MoS_2NDS/graphene sample. (d) Raman spectra of R6G molecules at the concentration of 5×10^{-5}M deposited on WS_2N-discs+MoS_2 N-discs/graphene (black), MoS_2N-discs+MoS_2 N-discs/graphene (green), and MoS_2N-discs /graphene (blue) heterostructures substrates. (e) The ratio (R) of the 613 cm^{-1} R6G peak intensity of the SERS substrates of MoS_2/G to the same peak on MoS_2/G (column 1), MoS_2NDs+MoS_2NDs/graphene (Colum 2), and WS_2 N-discs+MoS_2NDs/graphene (Column 3).

To examine the SERS sensitivity of the MoS_2NDs+WS_2 N-discs/graphene substrates, the R6G molecules droplets of different concentrations in a range from 5×10^{-5} M to 5×10^{-13} M were casted on the substrate. Raman spectra were taken with a 532 nm excitation. The R6G Raman spectra are compared at the R6G concentrations of 5×10^{-5} M to 5×10^{-9} M in Figure 4.1.6a, and the R6G concentrations of 5×10^{-10} M to 7×10^{-13} M in Figure 4.1.6b, respectively. All Raman signatures associated to the R6G are observable at R6G concentrations around 5×10^{-9} M or higher. With further decrease of the R6G concentration to 7×10^{-13} M, the detectable signature modes of R6G are limited to the vibrational modes with greater polarizability, such as 613 cm^{-1}, 773 cm^{-1} and 1191 cm^{-1}. Actually, the peak at 613 cm^{-1} can be noticeable at the lowest concentration of R6G of 5×10^{-13} M. Therefore, the R6G sensitivity of 5-7×10^{-13} M of the MoS_2NDs+WS_2 N-discs /graphene is about two orders of magnitude higher than the best sensitivity so far reported using the plasmonic metal nanostructure/graphene substrates [114]. In addition, this sensitivity on the mixed MoS_2N-discs+WS_2 N-discs/graphene SERS substrate is about one order of magnitude higher than that of the single kind of the TMDs-NDs/graphene counterparts [69]. In fact, the enhanced R6G SERS sensitivity MoS_2N-discs+WS_2 N-discs/graphene SERS substrate demonstrated in Figure 4.1.6 is consistent with the enhancement of graphene Raman signatures shown in Figure 4.1.3a on the same substrate, which can be ascribed to the LSPR effects superposition from MoS_2NDs and WS_2 N-discs in the WS_2N-discs+MoS_2 N-discs/graphene. Figure 4.1.6c displays Raman spectra at the R6G concentration of 7×10^{-13} M collected at ten spots arbitrarily chosen on a sample to illustrate consistency and reproducibility. The spots were designated to be distanced from the sample droplet's edge to prevent the coffee-ring effect. Figure 4.3.6d shows the histogram of the 613 cm^{-1} peak intensity of the ten spectra in Figure 4.1.6c.

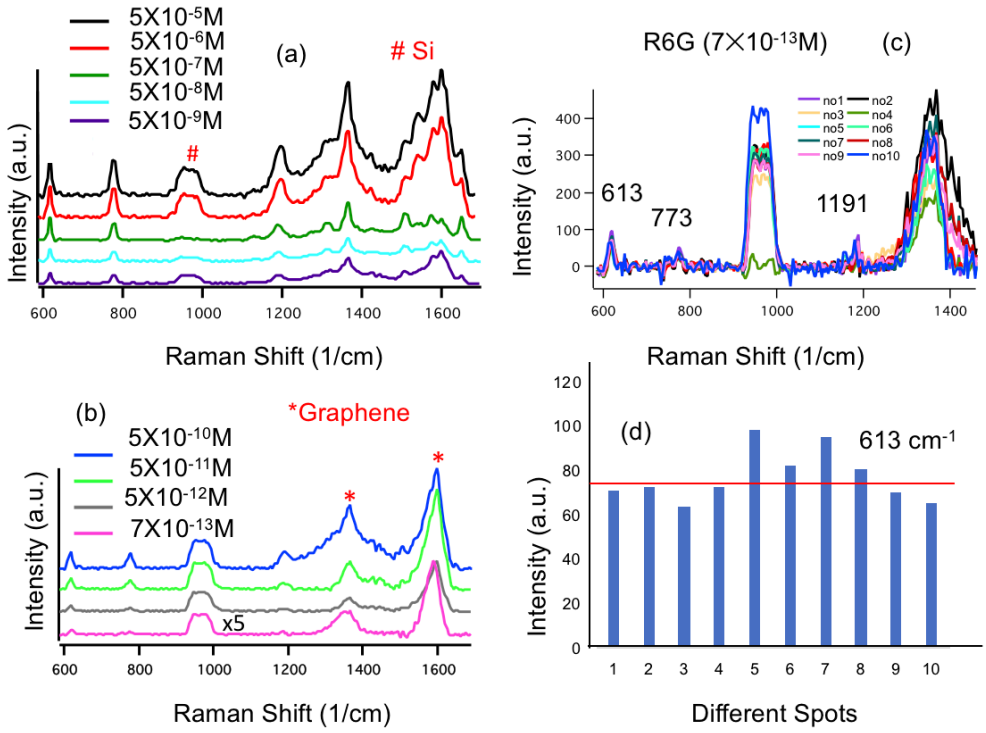

Figure 4.1.6 Raman spectra of the R6G molecules with different concentrations in the range of 5×10^{-5} M to 5×10^{-9} M (a), and 5×10^{-10} M to 7×10^{-13} M (b) on the WS_2N-discs+MoS_2 N-discs/graphene vdW heterostructures substrates. (c) Raman spectra of R6G molecules of 7×10^{-13} M concentration collected from seven random positions of the same sample, and (d) histogram of the peak intensity at 613 cm^{-1} for the seven spectra in (c). The Raman excitation was at 532 nm.

The R6G concentration dependence of the R6G Raman peak intensities at 613 cm^{-1} are depicted in Figure 4.1.7a-b for the MoS_2NDs/graphene, Figure 4.1.7c-d for the AuNPs/WS_2N-discs/graphene, and Figure 4.3.7e-f for the WS_2N-discs+MoS_2 N-discs/graphene, respectively. Figure 4.1.7a**,** 4.1.7c and 4.1.7e are in linear scale while Figure 4.1.7b, 4.1.7d and 4.3.7f, in semi-logarithmic scale. When viewing Figure 4.1.7a**,** 4.1.7c and 4.1.7e in a logarithmic scale in the R6G concentration axis, it is obvious that their correlation is logarithmic as illustrated in Figure 4.1.7b, 4.1.7d and 4.1.7f respectively. This relation of y=lgx+m has been reported in other studies

involving plasmonic nanostructures and SERS using a variety of analyte molecules [50, 115-117].

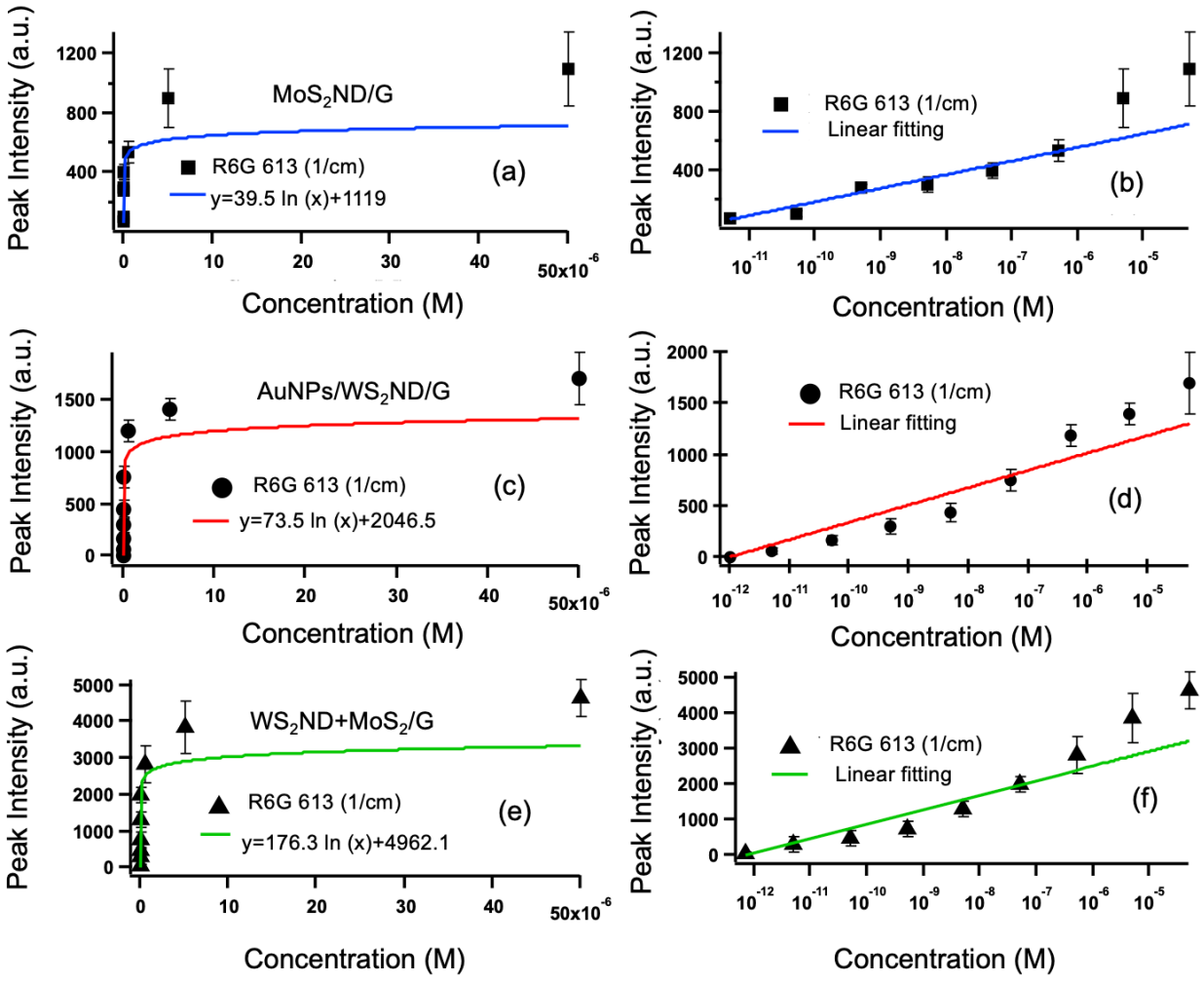

Figure 4.1.7 The intensities of the Raman at 613 cm^{-1} peak as a function of the R6G concentration on (a, b) MoS_2NDs/graphene, (c, d) the AuNPs/WS_2N-discs/graphene, and (e, f) the WS_2N-discs+MoS_2 N-discs/graphene using a linear scale (a, c, e) and a semi-logarithmic scale (b, d, f). The Raman excitation was at 532 nm

The results presented in this paper suggest formation of LSPRs in TMD NDs. Considering the wavelength range and the sizes of such NDs, theoretical investigation of such LSPRs requires a detailed microscopic approach, which is out of the scope of this paper. Instead, here we present a phenomenological approach that can shed some light onto the impact of density of NDs in their

overall optical responses. For this we utilized the FDTD technique for Ag NDs with lateral diameter of 100 nm and 20 nm thickness at the center (Figure 4.1.8a). Such a material structure is quite different from WS_2 and MoS_2 studied in this paper. Considering the fact that LSPRs are ubiquitous optical signature of charge carriers and the Ag NDs considered here are shown to have similar spectral plasmonic features as those of the WS_2 and MoS_2 N-discs, we believe this model can highlight the impact of inter-N-discs coupling on their collective optical properties.

For simulation we considered a planar light reaches the Ag ND structure with linear polarization. The separation between the NDs were considered to be random to mimic the experimental conditions (Figure 4.1.8a). Considering the lateral dimension of the SiO_2 substrate used in the simulation was 1 μm^2, the density of Ag NDs is given as N/μm^2. Figure 4.1.8b compares the relative extinction spectra for Ag NDs/SiO_2 substrates with densities of 1 (solid line), 3 (dashed line), 5 (dotted-dashed line), 10 (dotted line), and 15 ND/μm^2 (thick dashed line). A dominant peak around 565 nm can be obviously observed in all spectra while the amount of extinction varies with N monotonically.

The sublinear increase of the extinction with N can be associated with the fact that not all NDs interact similarly with light. To see this better in Figure 4.1.9 we show the results of the simulation for the plasmonic mode profiles of the cases associated with densities 5 (a), 10 (b), and 15 ND/μm^2 (c) at 565 nm. The color variations in Figure 4.1.9 refer to slight fluctuations in the positions of the Ag NDs. Note that these results further highlight the fact that plasmonic field enhancement tends to reach its maximum around the wavelength of the extinction peak (Figure 4.3.8b). Figure 4.1.9c shows that as N increases the inter-ND coupling starts to become more significant. This can be related to the results in Figure 4.1.8b that suggest an average enhancement of extinction by about 80% when N increases to 2N. This is compatible with the experimental

results shown Figure 4.1.3b. In fact, a close inspection of this figure shows that the addition of the WS_2N-discs to MoS_2NDs/graphene increases its absorption (extinction) by ~80%. This confirms that the number of WS_2N-discs was similar to that of MoS_2 N-discs in the WS_2N-discs+MoS_2N-discs/graphene sample. Additionally, it shows the extent of nonuniformity in the interaction of NDs with the incident light and the extent of the inter-ND coupling.

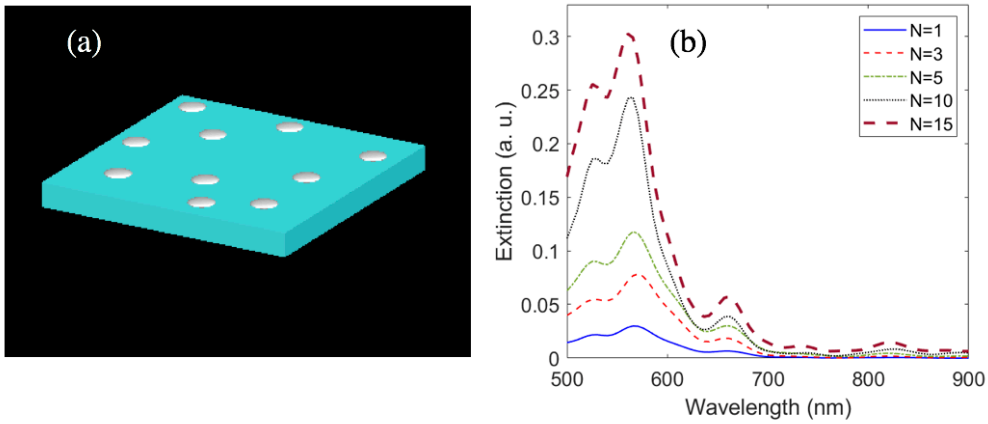

Figure 4.1.8 (a) Random arrangement of N=10 Ag NDs on a SiO_2 substrate. (b) Relative extinction spectra of Ag NDs on SiO_2 substrate as a function of their numbers or areal concentrations. The area of the substrate shown in (a) is 1 μm^2.

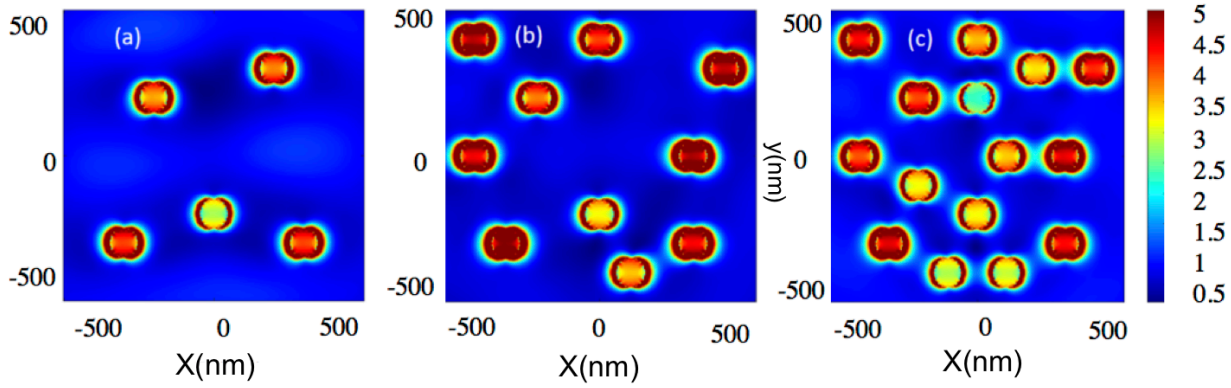

Figure 4.1.9 Electric field enhancement profiles of the Ag NDs when N=5 (a) 10 (b) and (c)15 Ag NDs. The color-coded bar on the right shows the extent of the field enhancement between 0-5.

Table 4.1.1 Particle density, width and height of N-discs along with their standard deviations

	Particle Density ($\frac{particles}{\mu m^2}$)	Width (nm)	Height (nm)
WS_2+MoS_2	1.4 ± 0.7	340 ± 180	6.9 ± 2.7
MoS_2+WS_2	1.3 ± 0.6	370 ± 240	8.6 ± 6.5

4.2 Conclusion

In summary, we established a novel SERS substrate with extra high sensitivity-based on plasmonic superposition on AuNP/WS_2 N-discs/ graphene vdW heterostructures and non-metallic SERS substrate of WS_2N-discs+MoS_2 N-discs/graphene vdW heterostructures. The first substrate integrates two plasmonic nanostructures of AuNPs and WS_2−NDs, and the DFT and FDTD simulations indicate that the improved dipole− dipole interaction together with charge transfer at the vdW interfaces plays a critical role to enable superposition of their LSPR effects. This has been confirmed experimentally in observations of enhanced graphene Raman signatures and enhanced SERS sensitivity of R6G probe molecules on the AuNP/WS_2−ND/graphene vdW heterostructure, comparing to that on WS_2−ND/graphene and AuNP/graphene substrates. Specifically, the graphene's G-peak intensity is enhanced by 7.8- fold by the combination of AuNPs and WS_2−NDs, in contrast to 5.3 or 4.0 folds respectively by WS_2−NDs or AuNPs alone. Moreover, the high R6G SERS sensitivity of 1×10^{-12} M achieved on the AuNP/WS_2−ND/graphene substrates is one or three orders of magnitude enhancement over that of on the WS_2−ND/graphene or AuNP/graphene,

respectively. Furthermore, this sensitivity is two to four orders of magnitude better than that on the TMDs/metal nanostructure SERS substratesand at least an order of magnitude better than the best SERS substrates reported in previous works.

The second intermix SERS substrate of WS_2N-discs+MoS_2 N-discs/graphene vdW heterostructures that were obtained via layer-by-layer growth using CVD and vapor transport processes over wafer size substrates including SiO_2/Si and fused silica may allow superposition of the LSPR effects from each the constituent WS_2N-discs and MoS_2NDs, resulting in much enhanced LSPR effect as compared to the counterparts with single kinds of TMD-NDs on graphene. Using R6G as the probe molecule, the SERS sensitivity of R6G has been evaluated on the WS_2N-discs+MoS_2 N-discs/graphene in comparison with several other SERS substrates including MoS_2N-discs/graphene, AuNPs/WS_2N-discs/graphene and pristine graphene. The obtained high SERS sensitivity up to 5-7×10^{-13} M on the WS_2N-discs+MoS_2 N-discs/graphene is about one order of magnitude higher than that on the single TMD-NDs/graphene counterparts, including MoS_2NDs/graphene and WS_2N-discs/graphene, and at least two orders of magnitude higher than that on the AuNPs/graphene and metal nanostructure/TMD substrates. In addition, the sensitivity of 5-7×10^{-13} M on the WS_2N-discs+MoS_2 N-discs/graphene is considerably higher than the sensitivity of ~10^{-12} M on the AuNPs/WS_2N-discs/graphene SERS substrate. Therefore, this result illustrates that the LSPR effect could be more efficiently induced on non-metallic TMD-NDs than in metallic nanostructures. Finally, the layer-by-layer growth process developed in this work for the WS_2N-discs+MoS_2 N-discsgraphene can be readily scaled up for run-to-run synthesis of the WS_2N-discs+MoS_2 N-discs/graphene vdW heterostructures SERS substrates for commercial applications.

Chapter 5: Controlling the Shape of TMDs Nanosturacture for Further Enhanced SERS

5.1 Motivation

Motivating by the extraordinary SERS sensitivity and enhancement that was achieved on TMD nanostructure, in this chapter we further explored the effect of TMDs shape on EM effect and SERS enhancement. Quantitatively, SERS enhancement relies on many factors such as the size and the shape of metallic nanostructures and substrate morphology [118-121]. For example, Hong *et al* examined SERS enhancement using 4-nitrothiophenol (4-NTP) and 4-aminothiophenol (4-ATP) as a probe by adsorbing them on gold nanoparticles (AuNPs) of the average lateral size of 17, 30, 40, 50, 60, and 80 nm. With increasing AuNPs lateral size, the SERS enhancement was found to increase initially until reaching the highest at ~50 nm. The observed trend was attributed to combined effect of AuNP size and shape for maximizing probe molecule adsorption, minimizing light scattering and optimizing electromagnetic field configuration. Similarly, Stamplecoskie *et al* examined the correlation between the SERS enhancement and AgNP lateral size using R6G as a probe [53]. In addition to a similar trend of SERS enhancement with AgNP size variation, the best SERS enhancement is reported on AgNPs of ~50 nm in lateral dimension. On the other hand, plasmonic nanostructures of different shapes have been fabricated including Au nanospheres[122], Au nanostars[123], Au nanorods[124] and so on [125, 126]. Li *et al* compared SERS on Au nanobipyramids and Au nanorods and found much stronger SERS signals in the former than in the latter [127]. Fan *et al* investigated SERS of graphene oxide (GO) hybrids with different Ag nanostructures including spheres, cubes and octahedral,[128] and observed a strong effect of shapes on SERS enhancement. The highest SERS enhancement was obtained on the Ag octahedra/GO.

In this chapter, we explore growth of MoS_2 nanodonuts (N-donuts) by controlling size of the $(NH4)_2MoS_4$ precursor nuclei via variation of its concentration in the range of 0.06 wt%-0.32 wt%. The hypothesis is that MoS_2 N-donuts could be achieved on large-size precursor nuclei due to the nonuniform conversion to MoS_2 along the radial direction while MoS_2 N-discs form on smaller nuclei when such nonuniformity is negligible. With increasing precursor concentrations, the precursor nuclei dimension increases monotonically and N-donuts become predominant at precursor concentration of 0.26 wt% or higher. Interestingly, a resonant R6G SERS sensitivity ~ 2×10^{-12} M was achieved on these MoS_2 N-donuts/graphene SERS substrates, in contrast to 5×10^{-12} M for the MoS_2 N-discs/graphene counterpart's[69]. More importantly, the obtained SERS sensitivity is more than two orders of magnitude higher than that of the AuNPs/graphene and TMDs/metal nanostructure SERS substrates,[129-132] indicating the non-metallic TMD plasmonic nanostructures can provide a promising alternative to the SERS and other applications that require light management**.**

5.2 MoS_2 Nanodonuts for high-Sensitivity Surface-Enhanced Raman Spectroscopy Sensing

Figure 5.2.1a exhibits the Raman spectra taken on samples including the pristine graphene (green, inset), MoS_2 N-discs (red) and MoS_2 N-donuts/graphene (blue) (Supporting Information). The G peak at ~1600 cm^{-1}, due to a primary in-plane vibration mode , and 2D peak at ~ 2707 cm^{-1} ,due to secondary in-plane vibration of zone-boundary phonons,[133] and D peak at ~1356 cm^{-1} (associated to the defect in graphene[54]) are clearly observable on the samples. On the pristine graphene, the intensity ratio of 2D peak to G peak (I_{2D} /I_G) is around 1.8 while I_D /I_G is negligible, indicating that the graphene is a monolayer with high quality. After MoS_2 N-discs were grown on

graphene the graphene Raman peak intensities are notably enhanced due to the LSPR effect on MoS_2 N-discs [69]. The enhancement factor of the graphene G peak is ~ 5. Interestingly, a higher enhancement factor of the graphene G peak ~ 8 is observed on the MoS_2 N-donuts/graphene sample, suggesting a stronger LSPR effect due to the decoration of the plasmonic MoS_2 N-donuts. It should be noted that such an enhancement in the Raman signature of graphene by metallic plasmonic has been reported on metal-nanostructures/graphene samples [64, 110, 111]. The similar trends observed on MoS_2 N-donuts/graphene and MoS_2 N-discs/graphene samples indicate that the LSPR can be effectively generated on nonmetallic TMD nanostructures and its magnitude is quantitatively affected by the shape on TMD nanostructure shapes. Figure 5.2.1b displays the Raman spectra of MoS_2 taken of MoS_2 N-discs (red) and MoS_2 N-donuts (blue), using Raman excitation at 532 nm. The Raman peaks in both spectra can be indexed to the E^1_{2g} at ~393 cm^{-1}(due to S and Mo atoms in-plane displacment mode) and A_{1g} at ~419 cm^{-1}(due to the S atoms out of displacment mode) of MoS_2 [134], confirming MoS_2 was grown on the graphene samples.

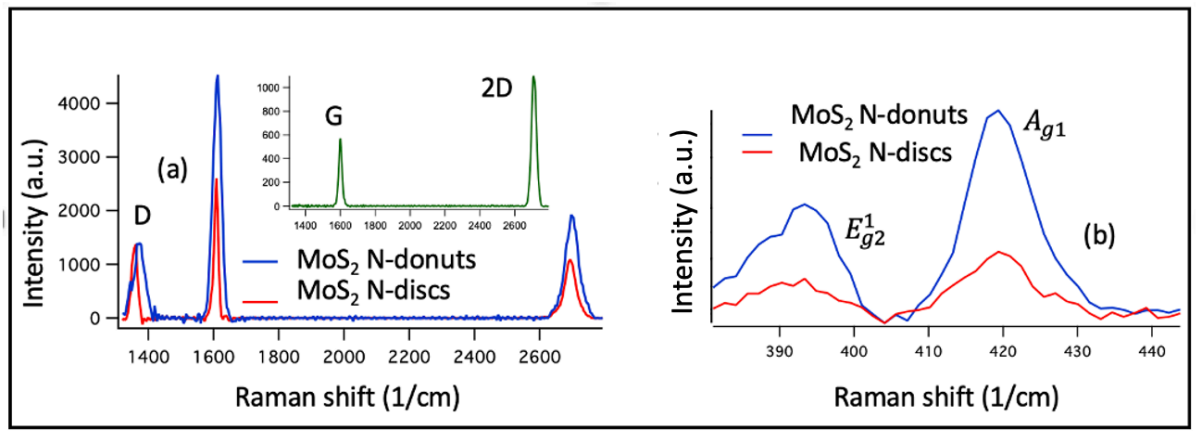

Figure 5.2.1 (a) Raman spectra of a pristine graphene (green, inset), and MoS_2N-donuts/graphene (blue) and MoS_2N-discs/graphene (red). (b) Raman spectrum of MoS_2N-donuts (blue) and MoS_2N-discs (red). All spectra were taken using 488 nm.

Figure 5.2.2 a-f show Raman maps of MoS_2 A_{g1} maps taken on MoS_2 N-donuts and MoS_2 N-discs/graphene samples made with different precursor solution concentrations of (a) 0.06 wt % , (b) 0.13 wt %, (c) 0.2 wt %, (d) 0.26 wt %, (e) 0.32 wt%, and (f) 0.4 wt%. The Raman maps show that the MoS_2 formed is not in continuous layer, rather is in the morphology of NPs of approximately round shape in the selected $(NH_4)_2MoS_4$ precursor concentration range. Quantitatively, the $(NH_4)_2MoS_4$ precursor concentration exhibits effect on both MoS_2 nanoparticles density and shapes. At the lowest precursor concentration of 0.06 wt%, the round shape of MoS_2 NPs grow in two different sizes: smaller size with an average diameter of ~200 nm (majority) and lager size of average diameter of ~1 μm with low density. With increasing precursor concentrations in the range of 0.2 -0.26 wt %, the size of the MoS_2 NPs changes moderately in the range of 300-600 nm, while the NP density increases. Above the precursor concentration of 0.26 wt%, the lateral dimension of the MoS_2 NPs increases considerably and the NP density decreases.

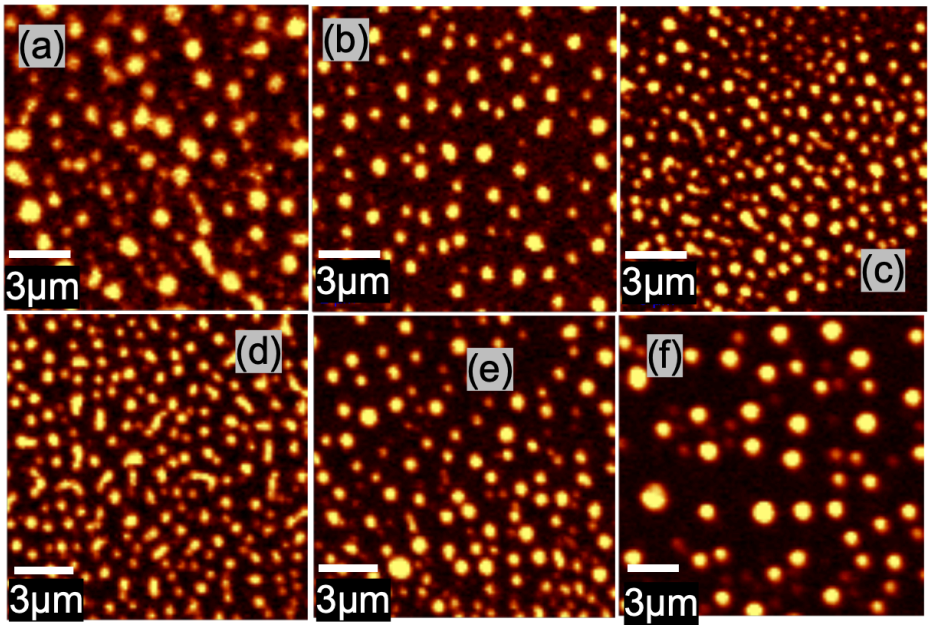

Figure 5.2.2 (a-e) MoS_2 A_{g1} peak Raman maps of MoS_2 N-donuts and N-discs/graphene samples that were synthesized with different precursor solution concentrations of (a) 0.06 wt %, (b) 0.13 wt %, (c) 0.2 wt % and (d) 0.26 wt % and (e) % 0.32 wt%, and (f) % 0.4 wt%.

A more quantitative measurement of the morphology and density of the MoS_2 N-discs and N-donuts is shown in AFM results (Figures 5.2.3 and 5.2.4) at different precursor concentrations. The discontinuous morphologies of the MoS_2 NPs have been confirmed in the entire range of the precursor concentration (Figures5.2.3) and the result agrees well qualitatively with the Raman maps in Figure 5.2.2. However, the better spatial resolution in AFM images in Figure 5.2.3 suggests the MoS_2 NPs tend to have irregular shapes at lower precursor concentrations while becoming more round-shaped at higher precursor concentrations of 0.26 wt% or higher.

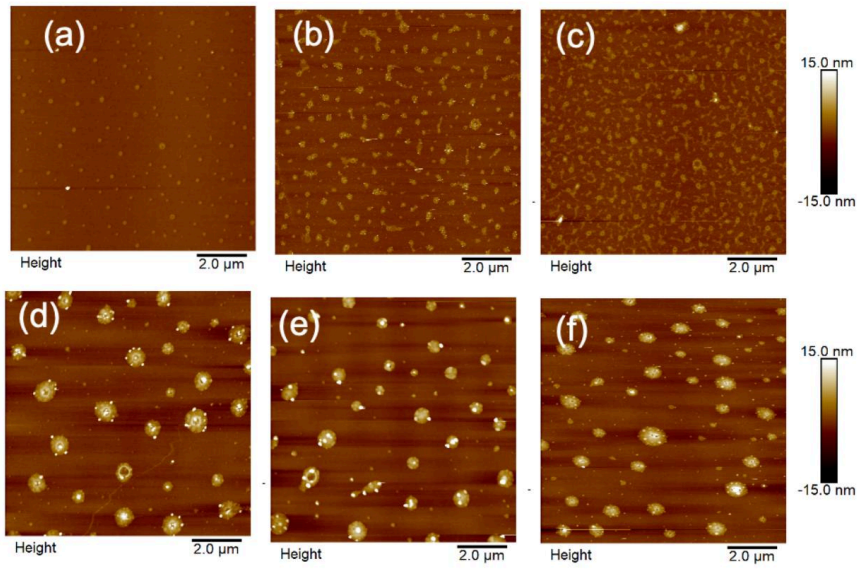

Figure 5.2.3 (a-f) Contact mode AFM images (10 ×10 μm) of MoS_2 samples that were synthesized with different precursor solution concentration. (a) 0.06 wt%, (b) 0.13 wt%, (c) 0.2 wt%, (d) 0.26 wt%, (e) 0.32 wt%, and (f) 0.40 wt%.

AFM images of 5 ×5 μm at selected concentrations are shown in Figure 5.2.4 a-c along with zoomed in images of single MoS_2 N-donuts and N-discs features in Figure 5.2.4 d-f. Interestingly, MoS_2 N-discs of smaller lateral dimension are the dominant features at lower precursor concentrations. In contrast, MoS_2 N-donuts have a larger lateral dimension and are present even in samples made at the lowest precursor concentration of 0.06 wt%. With increasing precursor concentration, the proportion of the MoS_2 N-donuts increases and in the samples made with precursor concentrations of 0.26% or higher, MoS_2 N-donuts become the dominant features. The average dimensions and density of the features are shown in Figure 5.2.4 g-h as a function of the precursor concentration. At low precursor concentrations, the MoS_2 NP diameter is between 200 to 400 nm, the height 2-7 nm, and the density is 2-4 particles/μm^2. Diameters and height increase up to 600 nm and 10 nm, respectively, with increasing precursor concentration which results in

density decreasing to 1.5 to 1 particles/μm^2 in and that may lead to the donuts shape. After a precursor concentration of approximately 0.20 %, the shape of MoS_2 N-donuts was obtained.

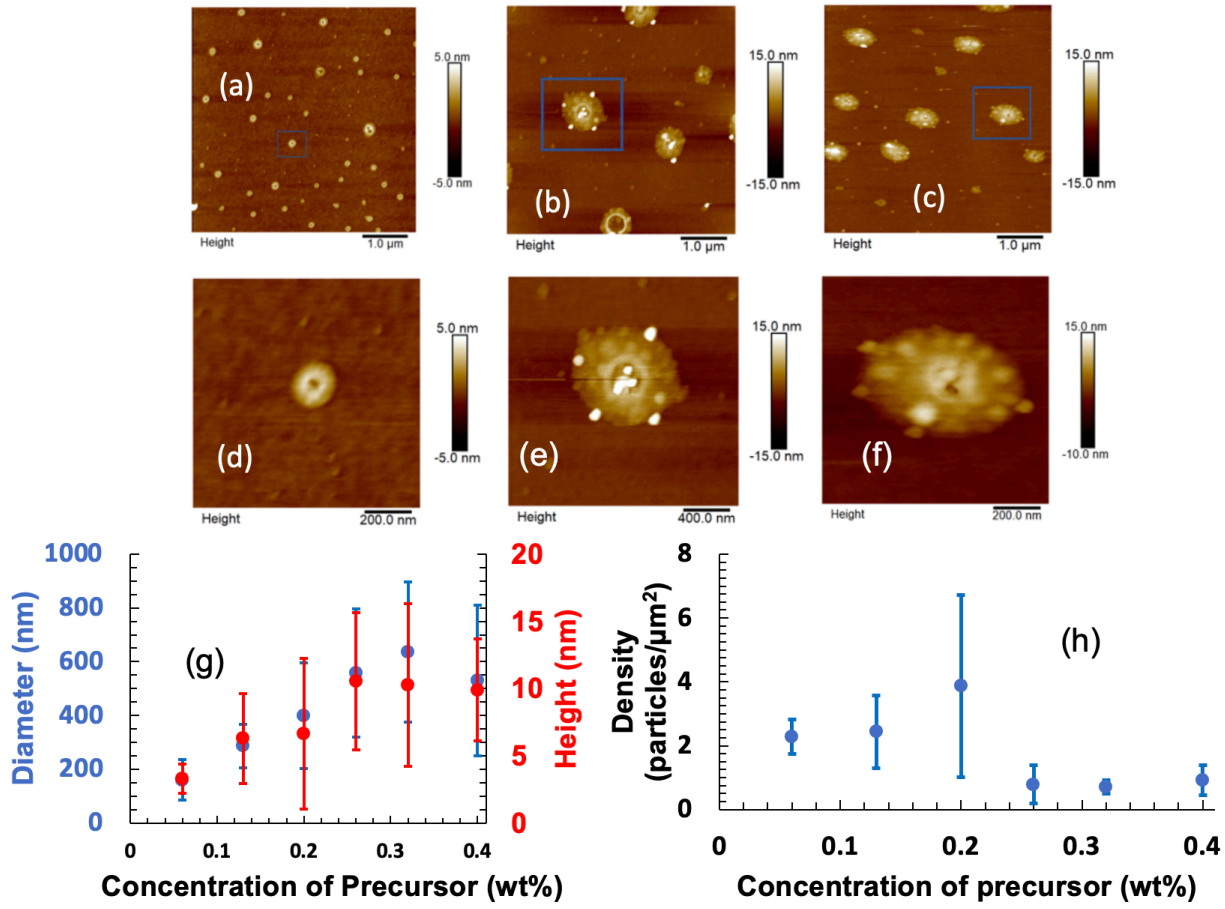

Figure 5.2.4 (a-c) Representative contact AFM images (5 $\mu m \times 5\ \mu m$) along with images of individual features from samples synthesized from MoS_2 precursor concentrations of (a) 0.06 wt%(b) 0.26 wt% and (c) 0.40 wt% (d-f) zoom in view of a-c AFM images, respectively. (g) Average diameter (blue) and height (red) of MoS_2 samples as a function of precursor concentration. (h) average density as a function of precursor concentration. Error bars represent the standard deviation of the measurement.

Figure 5a displays the comparison of the Raman spectra of R6G (5×10^{-5} M) probe molecules on MoS_2/graphene nanohybride substrates that were synthesized with different precursor solution concentrations from 0.06 wt% to 0.32 wt%, measured using the same excitation

of 532 nm wavelength. Most of the R6G Raman peaks are visible on all spectra. Especially, the spectra include the R6G fundamental peaks at 613 cm^{-1} allocated to the C–C–C ring in-plane vibration mode, 773 cm^{-1} assigned to aromatic C–H bending mode, 1190 cm^{-1} and 1648 cm^{-1} allocated to C–O–C stretching mode and the C–C stretching mode, respectively [15, 135]. Among the five spectra, the R6G spectra on the lowest precursor concentration of 0.06 wt% (green) have the lowest R6G peak intensity, indicative of the lowest SERS enhancement. It should be mentioned that MoS_2 N-discs are predominant in this sample. In contrast, the highest SERS enhancement is observed on the spectrum for MoS_2/graphene nanohybride made with 0.26 wt% precursor concentration (black) on which MoS_2 N-donuts are predominant. Quantitatively, the enhancement factor can be estimated using the ratio of the intensity of the R6G Raman peaks on the MoS_2/graphene samples made using different precursor concentrations at 613 cm^{-1} and 773 cm^{-1} to the ones on the MoS_2 (0.06 wt%)/graphene). Figure 5b exhibits the estimated enhancement factor as a function of precursor concentration of the five samples shown in Figure 5a. The maximum enhancement factor of 8.2 was obtained on the MoS_2/graphene sample at 0.26 wt% precursor concentration, suggesting that the SERS enhancement is a compromise of the shape, dimension, and density of MoS_2 NPs. Interestingly, MoS_2 N-donuts are predominant in MoS_2/graphene nanohybrides when the precursor concentration is exceeding ~0.20 wt%. The higher SERS sensitivity in this precursor concentration range, especially the peak SERS sensitivity in MoS_2/graphene nanohybride made from 0.26 wt% precursor concentration, suggests that MoS_2 N-donuts may support LSPR in a more preferable way than other N-discs or other shapes of MoS_2 nanostructures.

The R6G molecule droplets of varying concentrations ranging from 5×10^{-5} M to 2×10^{-12} M were cast and dried on the substrate and then Raman spectra were gathered with a 532 nm laser.

The R6G Raman spectra are compared at the R6G concentrations of 5×10^{-5} M to 5×10^{-9} M in Figure 5c, and the R6G concentrations of 5×10^{-10} M to 2×10^{-12} M in Figure 5d, respectively. All Raman signatures peaks of R6G are obvious at R6G concentrations above 5×10^{-10} M. With further reduction of the R6G concentration to 2×10^{-12} M, most of the R6G Raman signature peaks are still detectable, particularly the vibrational modes with larger polarizability, such as 613 cm^{-1}, 773 cm^{-1}, 1191 cm^{-1}, and 1648 cm^{-1}. Therefore, the R6G sensitivity of 2×10^{-12} M on the MoS_2 N-donuts/graphene nanohybrid is about half an order of magnitude higher than that obtained on MoS_2 N-discs/graphene [69] and about one order of magnitude higher than the best so far reported using the plasmonic metal nanostructure/graphene substrates [114].

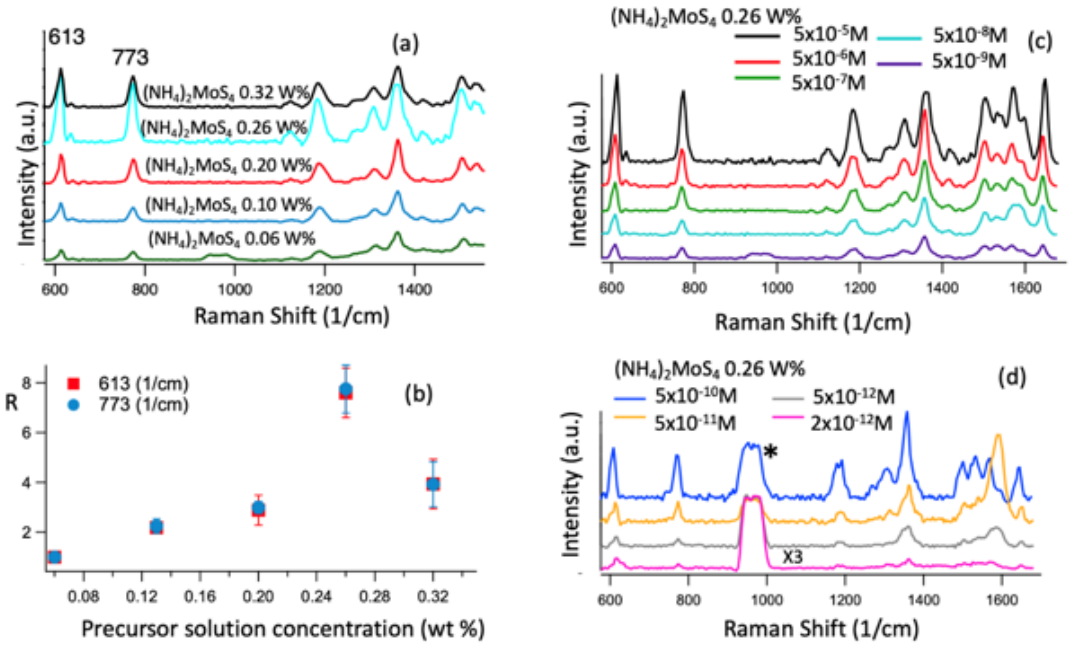

Figure 5.2.5 (a) Average Raman spectra of R6G molecules at the concentration of 5×10^{-5} M, collected from six batches of the samples shown in Figure S2, deposited on five MoS_2/graphene nanohybrids substrates, MoS_2 was synthesized with a precursor solution concentration of 0.06 wt % to 0.32 wt %. (**b**) The corresponding enhancement factor of the 613 and 773 cm^{-1} R6G peaks intensity on the five samples that were synthesized with different precursor solution concentrations with respect to the one was synthesized with a precursor solution concentration of 0.06 wt %. (**c**,**d**) Raman spectra of the R6G

molecules with different concentrations in the range of 5×10^{-5} M to 5×10^{-9} M (**c**), and 5×10^{-10} M to 2×10^{-12} M (multiplied by 3) (**d**) on the MoS_2/graphene nanohybrids substrates, MoS_2 was synthesized with a precursor solution concentration of 0.26 wt %. The * mark denotes the Si peak.

Figure5.2.6 shows the comparison of SERS Sensitivity and R6G 613cm $^{-1}$ peak enhancement factor (with respect to that on graphene SERS substrates) on different SERS substrates of graphene, MoS_2 N-discs(0.1 wt %)/graphene[69], AuNPs/MoS_2 N-discs (0.1 wt %)/graphene[136], WS_2 N-discs +MoS_2 N-discs (0.1 wt %)/graphene[137] and MoS_2 N-donuts (0.26 wt %)/graphene. The result shows that the best enhancement was obtained on the MoS_2 N-donuts (0.26 wt %)/graphene, while the best sensitivity was obtained on WS_2 N-discs +MoS_2 N-discs (0.1 wt %)/graphene.

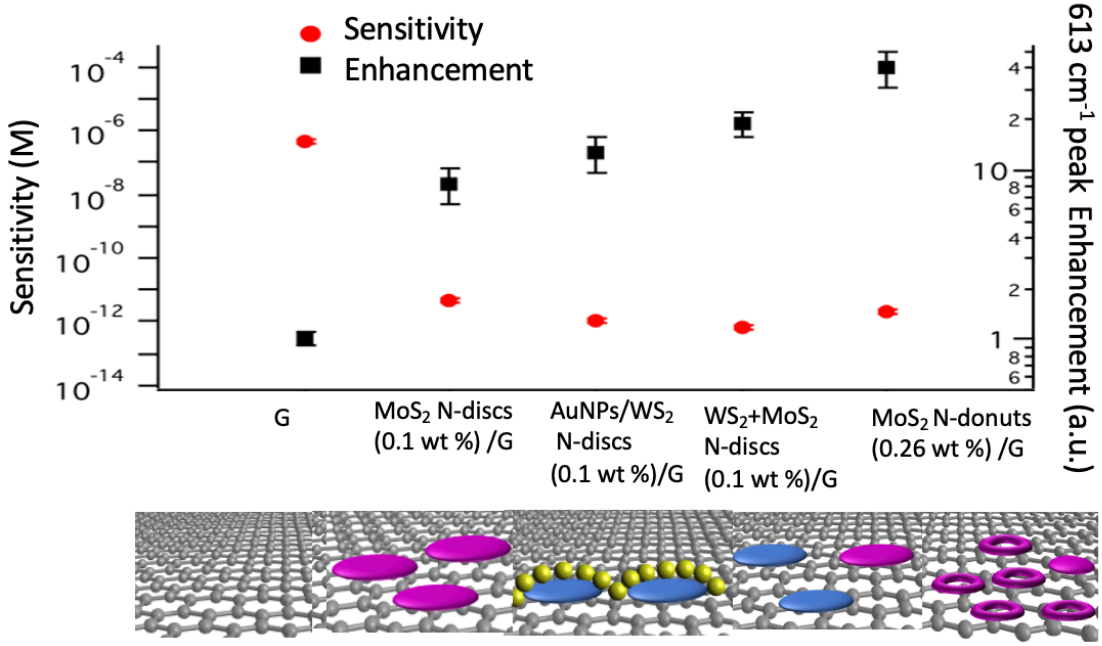

Figure 5.2.6 Comparison of SERS Sensitivity and R6G 613cm $^{-1}$ peak enhancement on different SERS substrates**:** graphene, MoS_2 N-discs (0.1 wt %)/graphene, AuNPs/MoS_2 N-discs (0.1 wt %)/graphene, WS_2 N-discs +MoS_2 N-discs (0.1 wt %)/graphene and MoS_2 N-donuts (0.26 wt %)/graphene.

The R6G Raman peak intensities at 613 and 773 cm^{-1} as a function of the R6G concentration are depicted in Figures 5.2.7 a-d for the MoS_2 N-donuts/graphene. Figures 5.2.7 a-b are in linear scale while Figures 5.2.7 c-d, in semi-logarithmic scale. The curves can be fitted approximately with an equation of $y = \log x + m$. Indeed, this logarithmic relation between the SERS intensity and concentration is noted in earlier reports of SERS sensitivity on a variety of analyte molecules [50, 115-117].

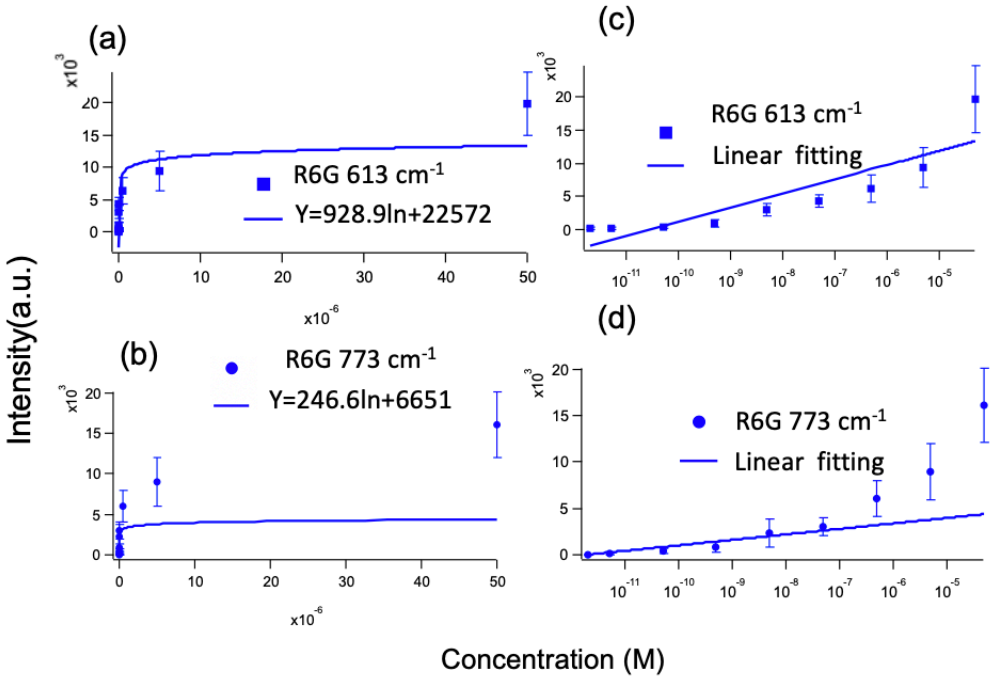

Figure 5.2.7 the intensities of the Raman at 613and 773 cm^{-1} peaks as a function of the R6G concentration on substrates using a linear scale (a, b) and a semi-logarithmic scale (c, d). The Raman excitation was at 532 nm.

The experimental results presented in this paper suggest a higher field enhancement for the case of TMD nanodonuts. The focus of our simulations is to examine the plasmonic features of such nanostructures and their differences with NDs. For this we adopted a phenomenological approach that can reveal these issues without dealing with the detailed microscopic treatment of plasmonic features of the TMD NDs and nanodonuts, which is out of our current scope. For this

we chose Ag as a material model. Of course such a material structure is very different from the MoS_2 material studied in this paper. However, since LSPRs are ubiquitous optical signatures of charge carriers, as shown below, our model can explain the impact the shapes of MoS_2 structures studied in this paper on the SERS enhancement. The simulations were done considering a normal planar polarized light reaching a NDs or N-donut placed on a SiO_2 substrate. The substrates were considered to be air. The mesh size in the x-y plane was considered to be 4 nm and along the z axis 0.5 nm. The extinction spectra of the structures were obtained as 1-T, wherein T was the transmittance.

To further clarify the impact of structure, we considered Ag N-donuts with external diameters (D) of 500, 360, and 240 nm (Figure 5.2.8a). The thicknesses were considered to be about 10 nm based on the experiment. The results presented in Figure 5.2.8b shows the plasmonic bi-resonance nature of such the N-donuts. When the external diameter of the N-donuts is 500 nm, these resonances occur at 815 and 1833 nm (Figure 5.2.8b, solid line). As the diameter decreases both of these resonances are blue shifted while they becoming more distinct (Figure 5.2.8b, dashed and dashed-dotted lines).

The bi-resonance nature of N-donuts allow them to present a robust field enhancement over a wide range of wavelengths. To see this in Figure 5.2.9 we show the field enhancement profiles associated with the N-donuts with external diameters of 500 nm ((a)-(d)) and 240 nm ((a')-(d')). These results suggest that the shorter wavelength peaks seen in Figure 5.2.8b are associated with the inner openings of the N-donuts (inner modes). The field enhancement profiles of such modes in the x-y (Figure 5.2.9a) and x-z (Figure 5.2.9b) planes show high values around the inner edges of the N-donuts. As the wavelength increases, these modes are gradually transformed to the outer edge modes of the N-donuts (Figures 5.2.10c-5.2.9d). The same scenario can also be

seen for the case of N-donuts with external diameter of 240 nm. As seen in Figures 5.2.10a'-5.2.9d' in this case the bi-resonance nature of plasmonic effects are even more continuous, offering large plasmonic field enhancement over a wide range of wavelength. For both cases of D=500 and 240 nm, around the wavelengths that the inner modes happen, the structures supports some degree of optical field enhancement deep in the superstrate. For the near field, close to the surface of N-donuts, one expects field enhancement factor more than 4.

In the case of N-discs (Figure 5.2.8c), however, the prime feature of the plasmonic effect is associated with the dipolar nature of their edge modes. As seen in Figure 5.2.8d, in such a structure when the diameter is 500 or 300 nm, these modes happen at 1850 and 1385 nm, respectively. The weak peaks seen at 800 and 620 nm could be associated with the weak cavity modes, generated by the relatively large lateral sizes of the N-discs. Figure 5.2.10 shows the mode field enhancement profiles in the x-y plane ((Figure 5.2.10a) and (Figure 5.2.10b)) and in the x-z plane ((Figure 5.2.10c) and (Figure 5.2.10d)) when the diameter of the N-disc is 300 nm. Note that the field enhancement associated with cavity modes are rather weak. The dipolar-like mode is rather strong, but it happens in the infrared range.

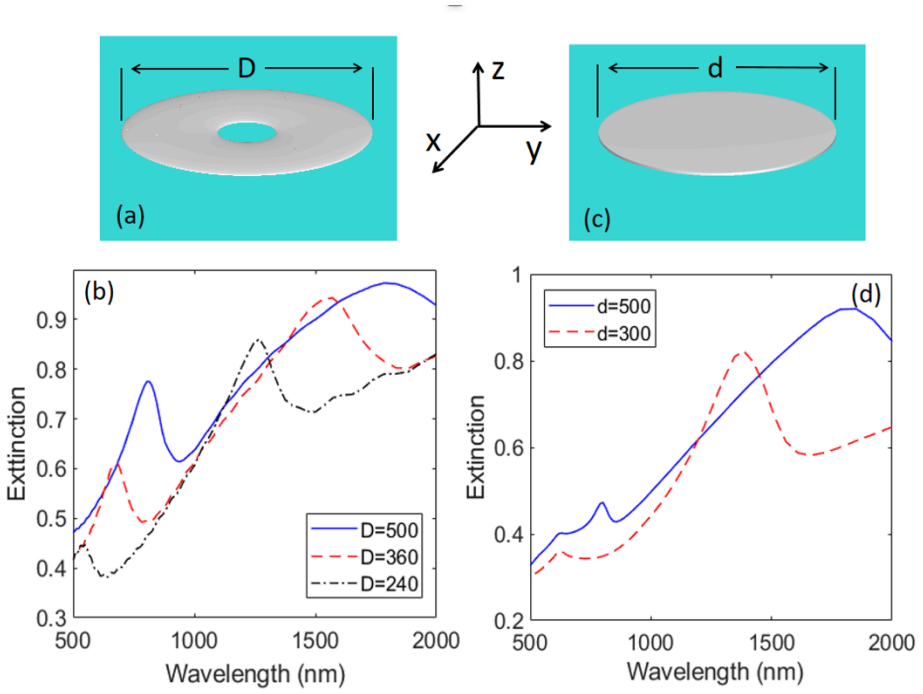

Figure 5.2.8 (a)Simulation structural model of an N-donut with external diameter of D. (b) Extinction of Ag N-donuts with D=500 (solid line), 360 (dashed line) and 240 nm (dashed-dotted line). (c) Simulation structural model of an N-discs with diameter d. (d) Extinction spectra of Ag N-discs with d=500 (solid line) and 300 nm (dashed line). The thicknesses of N-donuts are considered to be 10 nm and those of N-discs to be 7 nm.

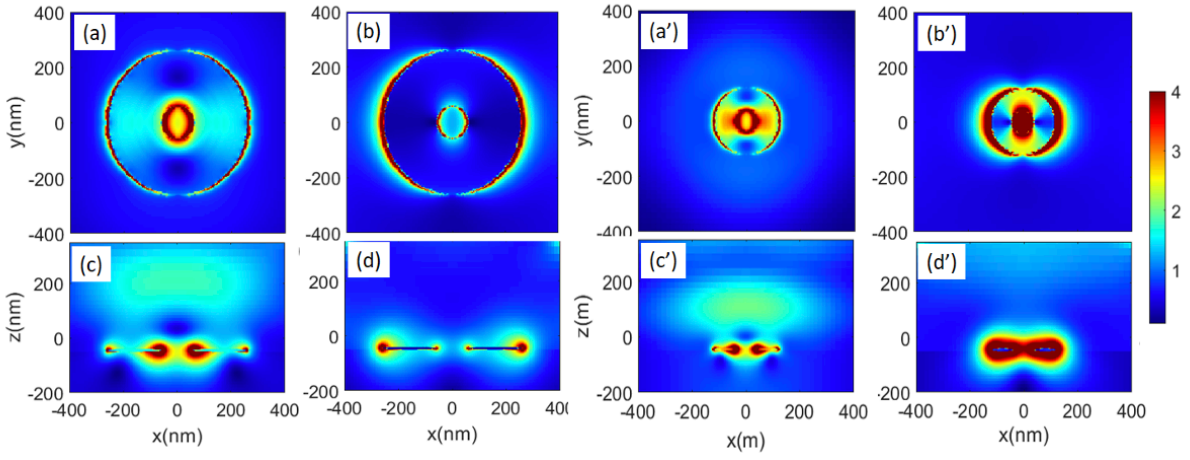

Figure 5.2.9 Mode field enhancement profiles associated with the N-donuts with D=500 nm ((a)-(d)) and 240 nm ((a')-(d')). (a) and (c) are the profiles in the x-y and x-z planes at 814 and (b) and (d) are those at 1833 nm. (a')-(c') are profiles at 532 nm and (b') and (d') are those at 1270 nm.

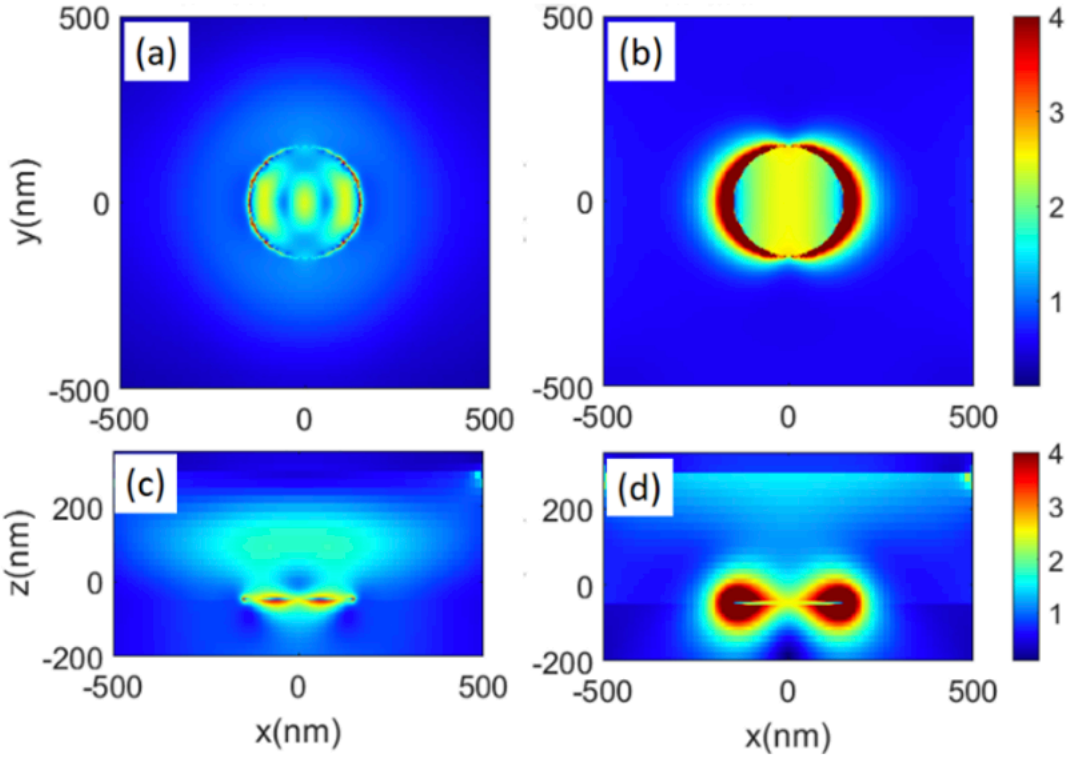

Figure 5.2.10 Mode field enhancement profiles associated in the x-y of a N-disc with D=300 at 620 nm (a) and 1385 (b). (c) and (d) show, respectively their profiles x-z planes

5.3 Conclusion

By varying the $(NH4)_2MoS_4$ precursor solution concentration in the range of 0.06-0.40 wt %, the precursor nuclei size is systematically altered to control the conversion of the precursor to MoS_2 during the sulfur vapor transfer process at 450 °C. At lower precursor concentrations, smaller precursor nuclei form on which the conversion to MoS_2 occurs fairly uniformly, leading to formation of MoS_2 N-discs predominantly on graphene or SiO_2/Si substrates. With increasing precursor concentrations, the precursor nuclei size increases monotonically to allow a faster conversion to MoS_2 at the edge of the nuclei than that in the center, resulting in formation of MoS_2 N-donuts of lateral dimension of 300-600 nm and height of 5-10 nm predominantly at precursor concentrations at and above 0.26 wt%. FDTD simulation indicates MoS_2 N-donuts can better

support LSPR than their MoS_2 N-discs counterparts. Indeed, higher R6G SERS sensitivity has been observed on MoS_2 N-donuts/graphene substrates than on the MoS_2 N-discs/graphene ones using R6G as a probe molecule. Specifically, high SERS sensitivity up to 2×10^{-12} M has been achieved on the MoS_2 N-donuts/graphene, in contrast to 5×10^{-12} M on the MoS_2 N-discs/graphene vdw heterostructure SERS substrates. This result illustrates the feasibility of tuning TMD nanostructure morphology for high-performance non-metallic plasmonic nanostructures using a low-cost, facile approach.

Chapter 6: Superposition of Plasmonic Effect from Metallic Au Nanoparticles and Non-metallic TMDC Nanodiscs

6.1 Motivation

TMD N-discs/graphene presented a unique platform for designing SERS substrates based non-metallic plasmonic structures. This, however, raises a question on whether the non-metallic and metallic plasmonic structures could be combined to further enhance the SERS sensitivity. In order to answer this question, this chapter explores superposition of the LSPR effects of AuNPs and TMD N-discs/graphene vdW heterostructure by decorating the TMD N-discs with AuNPs.

The EM and CM effects can be integrated on the hydride system of 2D atomic materials such as graphene and TMDs and plasmonic metal nanostructures [64, 138-140]. In the previous chapters, TMD nanostructures has demonstrated strong SERS EM enhancement which can be further improved by decorating the TMDs/graphene with AuNPs due to superposition of the LSPR effects of AuNPs and TMD N-discs of AuNPs/WS_2 N-discs/graphene vdW heterostructures.

6.2 Au Nanoparticle/WS_2 N-discs/Graphene van der Waals Heterostructure Substrates for Surface-Enhanced Raman Spectroscopy

Figure 6.2.1a illustrates schematically the AuNPs/WS_2 nanodisc (NDs)/graphene vdW heterostructure for R6G detection as a SERS substrate. The Raman signatures of the R6G probe molecules attached to the substrate are expected to be enhanced by both the EM and CM effects. In order to quantify the LSPR enhancement by the integrated plasmonic AuNPs/WS_2-NDs, Raman spectra of graphene were taken on graphene only, WS_2-NDs/graphene and AuNPs/WS_2-NDs/graphene and the results are depicted in Figure 6.2.1b. On all four samples, the graphene' defect D-peak at ~1356 cm^{-1} has an insignificant intensity, confirming the high quality of the graphene synthesized using CVD for this work. The two main signatures of graphene: i.e. the G

peak at ~1587 cm^{-1} due a primary in-plane vibrational mode and the 2D peak at 2695 cm^{-1} due to a secondary in-plane vibration of zone-boundary phonons, are clearly observable in Figure 6.2.1b. On the graphene only sample (green), the ratio of the 2D and G peak intensities is around 2.1, which is expected for monolayer graphene. However, the peak intensities differ quantitatively due to the LSPR effect at the same Raman measurement condition of 488 nm excitation of 1 mW power. In fact, the G and 2D peak intensities are considerably enhanced with decoration of the plasmonic WS_2-NDs (black) plasmonic AuNPs (blue) and AuNPs/WS_2-NDs (red). On the WS_2-NDs/graphene and AuNPs/graphene samples, the enhancement factors of the graphene G peak and 2D peaks are, respectively, 4.0 and 3.0 and 5.3 and 4.0, which are comparable to that reported previously on plasmonic metal nanostructures/graphene [64, 110, 141]. On the AuNPs/WS_2-NDs/graphene samples, the enhancement factors of the graphene G and 2D peaks is further increased to about 7.8 and 5.6, respectively, which may be attributed to the superposition of the LSPR effects of AuNPs and WS_2-NDs in the AuNPs/WS_2-NDs/graphene vdW heterostructures. The enhanced LSPR effect of the AuNP/WS_2-NDs is most probably due to the increased dipole-dipole interaction at the AuNP/WS_2-NDs vdW interface as shown in a Density Function Theory simulation (DFT) [71]. Figure 6.2.1c shows the side view of the Au/WS_2/graphene heterostructures of 2 atomic layers of Au after the relaxation process in DFT simulation. The electronic structure of the interface between MoS_2 (or WS_2) 2D layer and 1-6 atomic layers of Au was reported recently [71]. It has been found that varying the layer number of the Au from monolayer (1L) to a few layer can lead to a significant reduction of the interatomic distance at the Au/MoS_2 interface, which consequently results in charge transfer enhancement in the AuNPs/MoS_2/graphene vdW heterostructures. Specifically, the interatomic distance is around 3.03 Å in the case of Au (1L) on top on MoS_2, and it reduces about 20% to around 2.47 Å when the Au layer number is increased

to two layers (2L) or more. An enhanced charge transfer is therefore anticipated due to the enhanced dipole-dipole interaction at a reduced interatomic distance, resulting in enhance SERS on Au (2L) or multilayer on WS_2/graphene heterostructures. In addition, 3D plots of the electron localization function (ELF) were investigated and delocalized electron level was shown to be limited on a monolayer of Au/MoS_2 [71]. In contrast, delocalized electron level increases in the presence of 2L or thicker Au layers. Figure 6.2.1d demonstrates the 3D plot of the ELF in the 3L-Au/WS_2 heterostructures. It can be seen that the ELF has a normalized scale of 0-1 with higher values (more red) revealing more localized electrons in "C-shape" red contour structures attaching S atoms to Mo atoms.

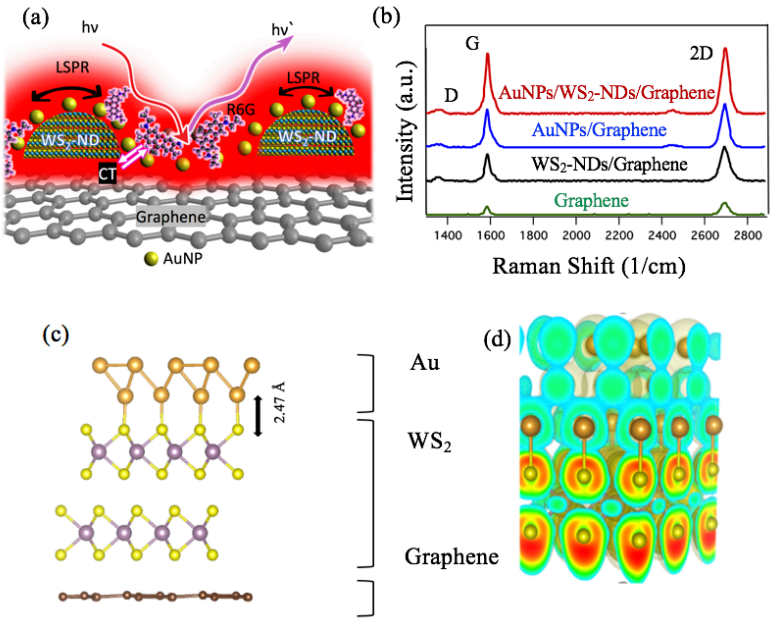

Figure 6.2.1 (a) Schematic illustration of the AuNPs/WS_2-NDs/graphene vdW heterostructure SERS substrate. (b) Raman spectra of graphene taken on four samples of graphene only (green), WS_2-NDs/graphene (black), AuNPs/ graphene (blue) and AuNPs/WS_2-NDs/graphene (red) using 488 nm laser of power of 1 mW. (c) The schematic illustration of the atomic layer stack of Au/WS_2/graphene hybrid heterostructures with the interface distance between the AuNPs and WS_2 labeled. (d) The 3D ELF plot of the stack of Au/WS_2 heterostructure shown in Figure 6.2.1c.

The Raman spectra taken on graphene and on WS_2-NDs/graphene vdW heterostructure are shown in Figure 6.2.2a. Besides the graphene signature peaks at ~1587 cm^{-1} and ~2695 cm^{-1}corresponding to the graphene 's G and 2D bands and a small disorder induced D band at ~1350 cm^{-1}, the Raman peaks associated to the WS_2-NDs grown on top of the single-layer graphene can be observed at ~342 cm^{-1} (E^1_{2g}) and ~ 412 cm^{-1} (A_{1g}) due to, respectively, the in-plane displacement of Mo and S atoms and the out-of-plane displacement of S atoms [142]. Figures 6.2.2b-c illustrate the Raman maps of graphene (2D mode) and WS_2 (E^1_{2g} mode) on the WS_2-NDs/graphene sample using the excitation laser of 488 nm in wavelength. The graphene's Raman map shows continues distribution with lower intensity on the location covered by the WS_2-NDs. The Raman map of the WS_2 (E^1_{2g} mode) exhibits an opposite intensity distribution, demonstrating the formation of the WS_2-NDs with lateral dimension on the order of 300–500 nm. Figure 6.2.2d displays an AFM image of the WS_2 N-discs, from which the lateral dimension of 300 nm-500 nm and height around 4-6 nm have been identified for the N-discs. Figure 6.2.2e-f display an SEM image and EDS maps of W (in green), Au (in purple) and C (in blue), respectively, of an AuNPs/WS_2/graphene heterostructures. The W, Au and C elemental mapping analyses confirm the uniform distribution of the AuNPs and WS_2-NDs on top of graphene with the lateral dimension consistent to that shown in AFM analysis and Raman map. The zoom-in SEM image of the same sample shown in Figure 6.2.2g and the particle size distribution histogram (Figure 6.2.2h) on the selected area marked on the SEM image show that the AuNPs are decorated uniformly throughout the sample including on top of the WS_2-NDs. Most AuNPs have approximately round shapes of lateral dimension in the range of ~40-50 nm. Under the nominal Au thickness of 10-12 nm, the height of the AuNPs is in the range of 10-15 nm [64].

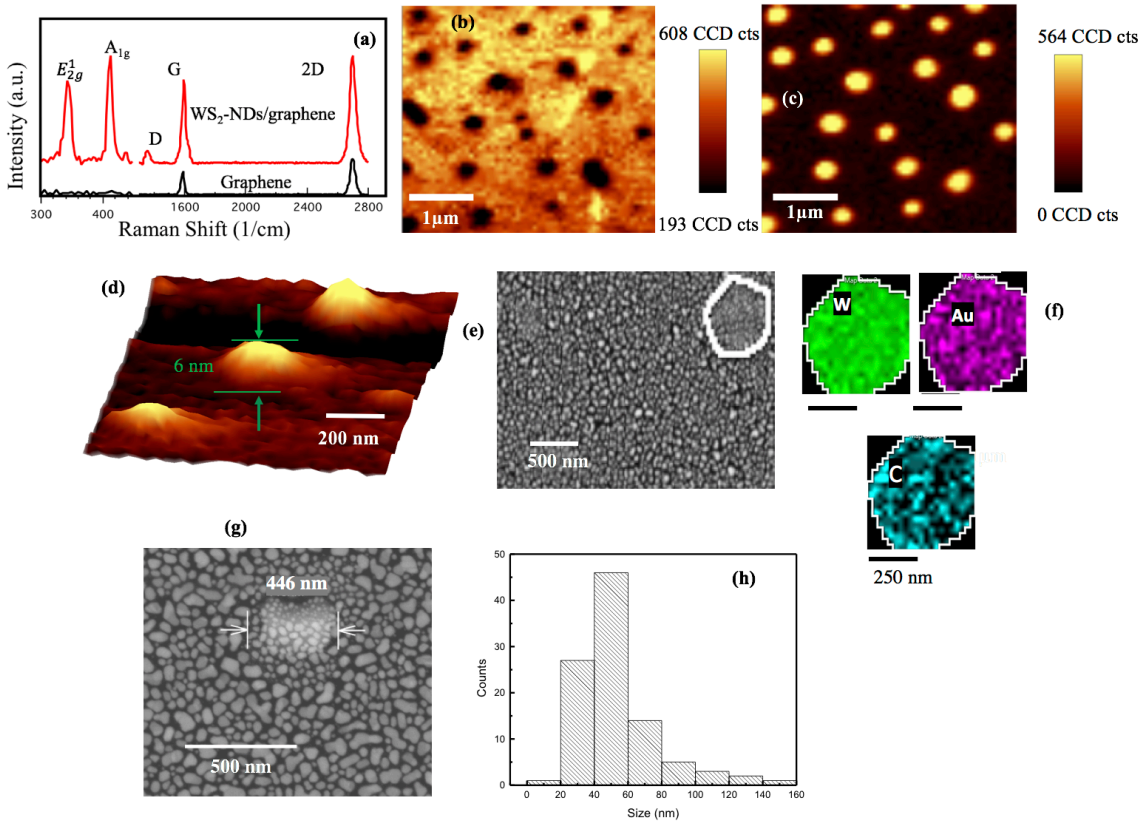

Figure 6.2.2 (a) Raman spectrum of WS_2-NDs/graphene vdW heterostructure and graphene. (b-c) Raman map of graphene (2D mode) and WS_2 (E^1_{2g} mode) on graphene and using the excitation laser of 488 nm. (d) An representative AFM image of the WS_2-NDs; (e-f) an SEM image of an AuNPs/WS_2-NDs/graphene sample and EDS maps of W(green), Au (purple) and C (blue). A zoom-in SEM image of the same sample (g) and a particle size distribution histogram taken on the selected area marked on (h).

Figure 6.2.3 shows the comparison of Raman spectra of R6G ($5x10^{-5}$ M) on AuNPs/WS_2-NDs/graphene heterostructures (red), WS_2-NDs/graphene heterostructures (black), AuNPs/graphene (blue) and graphene (green) substrates using the same excitation of wavelength of 532 nm. A series of R6G Raman signature peaks can be identified on all three spectra including the 613 cm^{-1} peak assigned to the C–C–C ring in-plane vibration mode, 769 cm^{-1} peak assigned to aromatic C–H bending mode, and the 1312 cm^{-1} and 1502 cm^{-1} peaks assigned to N–H in plane bend mode. The peaks at 1361 cm^{-1}, 1504 cm^{-1}, 1576 cm^{-1} and 1648 cm^{-1} can be assigned to the C–C stretching mode, and the 1190 cm^{-1} peak, assigned to C–O–C stretching mode, respectively [15, 143, 144]. For R6G on graphene substrate, the spectrum shows visually low Raman signature

intensity as compared to the spectra on the other three substrates in the same figure. By using the feature peak of R6G at 613 cm^{-1} on graphene as the reference, the enhancement factors of 10.3 and 8.7 have been obtained on WS_2-ND_S/graphene and AuNPs/graphene substrates, respectively. Furthermore, the enhancement factor is increased to 21.2 on the AuNPs/WS_2-NDs/graphene heterostructures, indicating the benefit of superposition of the SERS enhancements by plasmonic AuNPs and WS_2-NDs. Interestingly, the R6G Raman signatures have comparable intensities on the WS_2-ND_S/graphene and AuNPs/graphene substrates, suggesting the SERS enhancement factors by the plasmonic AuNPs and WS_2-ND_S are comparable. This is not surprising considering both AuNPs and TMD-NDs (WS_2-ND_S and WS_2-ND_S) are strong plasmonic nanostructures due to the EM effect [50, 64, 145]. However, the R6G Raman signatures are considerably enhanced on the AuNPs/WS_2-NDs/graphene heterostructures as compared to that on the WS_2-NDs/graphene and AuNPs/graphene substrates. For example, the R6G at 613 cm^{-1} peak is a factor of 2.0 and 2.4 stronger on the AuNPs/WS_2-NDs/graphene substrate than on the WS_2-NDs/graphene and AuNPs/graphene substrates respectively. Similarly, the enhancement factors of the R6G signature at 773 cm^{-1} are 1.6 and 2.4, respectively. This observed SERS enhancement illustrates the benefit of the superposition of the LSPR effects from the WS_2-NDs and AuNPs in the AuNPs/WS_2-NDs/graphene vdW heterostructures.

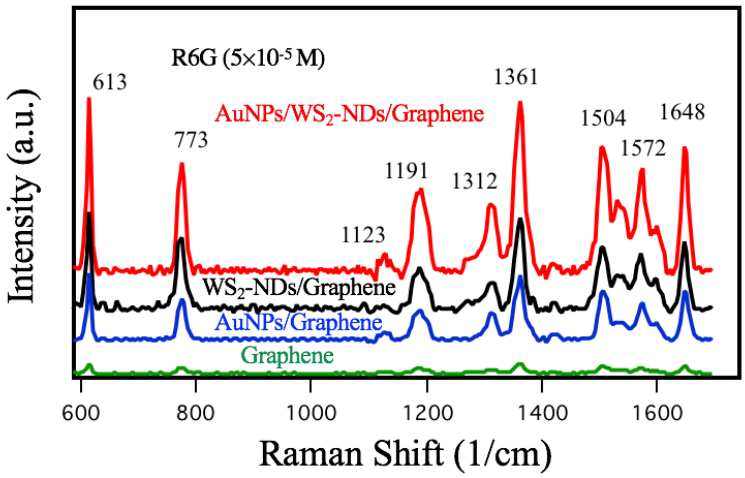

Figure 6.2.3 Raman spectra of R6G molecules at the concentration of 5×10^{-5}M deposited on AuNPs/WS_2-NDs /graphene (red), WS_2-NDs /graphene heterostructures substrates (black), AuNPs /graphene (blue) and graphene (green) with excitation length of 532 nm.

In order to probe the SERS sensitivity of the AuNPs/WS_2-NDs/ graphene vdW heterostructure substrates, Raman spectra of R6G molecules of different concentrations as low as 10^{-12} M were collected using the 532 nm resonance excitation wavelength for R6G, Figure 6.2.4a. On the AuNPs/WS_2-NDs/graphene vdW heterostructure substrate, all Raman signatures of R6G are visible at higher R6G concentrations above 5×10^{-12} M. With further reduction of the R6G concentration, the detectable signature modes of R6G are limited to the vibrational modes with larger polarizability, such as 613 cm^{-1}, 773 cm^{-1} and 1191 cm^{-1}. In fact, the 613 cm^{-1} peak remains visible at the lowest R6G concentration of 1×10^{-12} M. For a comparison, the same experiment was repeated on the WS_2-ND_S/graphene and AuNPs/graphene substrates and the results are shown in Figure 6.2.4b-c.. The Raman signatures of R6G are visible up to the lowest R6G concentrations of 5×10^{-11} M and 5×10^{-9} M, respectively, on WS_2-ND_S/graphene and AuNPs/graphene substrates. This indicates that the R6G SERS sensitivity is indeed enhanced through superposition of the LSPR effects of AuNPs and WS_2-NDs on the AuNPs/WS_2/graphene vdW heterostructure substrates. In addition, the resonant Raman spectra (with 532 nm Raman excitation) of the R6G on AuNPs/WS_2-NDs were collected as shown in Figure 6.2.5. The lower sensitivity of about 5x10-

^{10} M is about an order of magnitude higher than that of 5×10^{-9} M on the AuNPs/TMD continuous layer substrates,[71]which can be attributed to the EM effect enabled in the TMD-NDs. Overall, the AuNPs/WS_2-NDs/graphene heterostructure substrate shows the best SERS enhancement, which is higher than that on AuNPs/graphene or WS_2 only, and to AuNPs/WS_2, implying the EM enhancement through superposition of the SERS from plasmonic AuNPs and WS_2-NDs enhanced by the interfaces in the AuNPs/WS_2-NDs/graphene heterostructures and the CM enhancement of graphene [71, 145]. In fact, the higher SERS sensitivity of the AuNPs/WS_2/graphene is more than an order of magnitude higher than that of the WS_2-NDs/graphene and about three order of magnitude higher than that of AuNPs/graphene [145]. To our knowledge, the R6G sensitivity of 1×10^{-12} M of the AuNPs/WS_2/graphene is one order of magnitude higher than the best resonance R6G sensitivity so far reported using the plasmonic metal nanostructure/graphene substrates,[114] and by about one to four orders of magnitude better than that on the TMDs (continuous layer)/metal nanostructure SERS substrates [71, 132, 146, 147]. In fact, the further enhanced R6G SERS sensitivity illustrated in Figure 6.2.4a is consistent with the enhanced graphene signature enhancement shown in Figure 6.2.1b on AuNPs/WS_2/graphene, which can be attributed to the superposition of the LSPR effects from AuNPs and WS_2-NDs in the AuNPs/WS_2-NDs/graphene heterostructures.

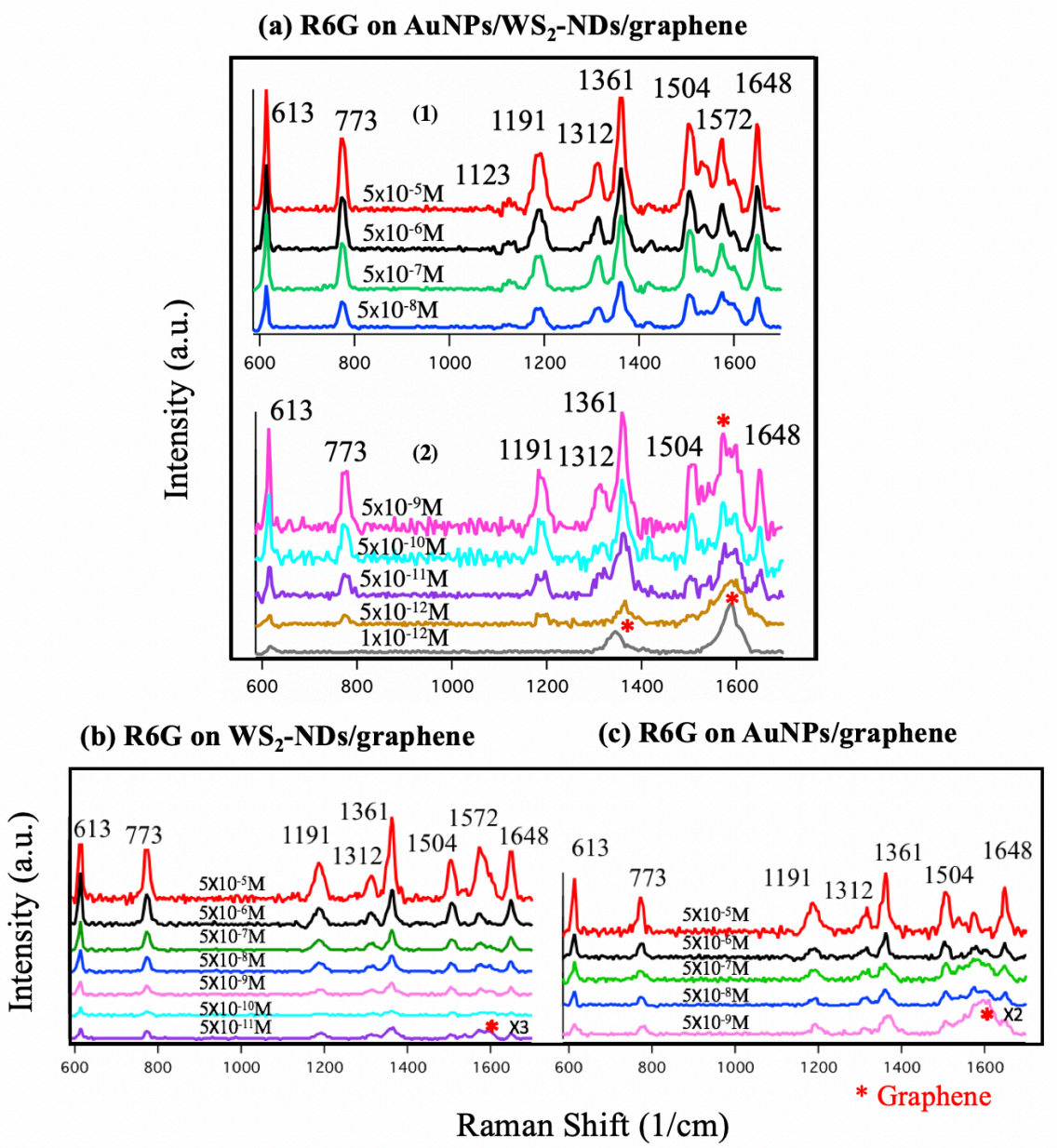

Figure 6.2.4 Raman spectra of the R6G molecules with different concentrations (a) from 5×10^{-5} M to 5×10^{-8} M (1) and from 5×10^{-9} M to 1×10^{-12} M (2) on the AuNPs/WS_2-NDs/graphene with excitation of 532 nm laser; Raman spectra of the R6G molecules with different concentrations: (b) from 5×10^{-5}M to 5×10^{-11} on the WS_2-NDs/graphene (the spectrum of the concentration $5x10^{-11}$ M was multiplied by 3 for better visibility); and (c) from 5×10^{-5}M to 5×10^{-9} on the AuNPs /graphene substrates (the spectrum of the concentration $5x10^{-9}$ M was multiplied by 2 for better visibility). All spectra were taken with excitation of 532 nm laser of the same power.

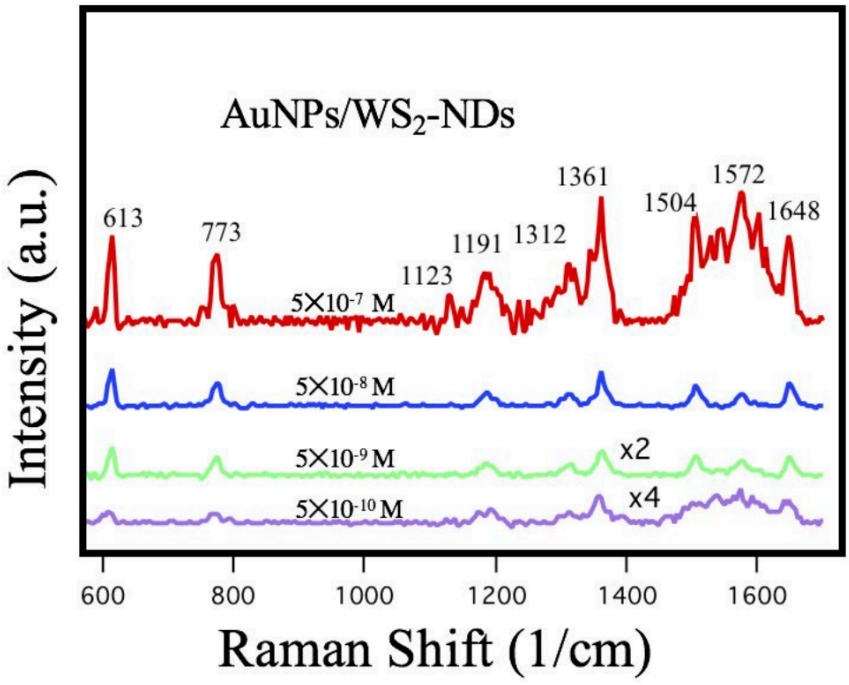

Figure 6.2.5 Raman spectra of the R6G molecules with different concentrations (a) from 5×10^{-5} M to 5×10^{-10}M on the AuNPs/WS_2-NDs with excitation of 532 nm laser.

Figure 6.2.6a-d illustrate the R6G Raman peak intensities at 613 cm^{-1} and 773 cm^{-1}, respecitively, as a function of the R6G concentration on AuNPs/WS_2-NDs/graphene vdW heterostructures. Figures 6.2.6a and 6.2.6c show the logarithmic relation between the Raman peak intensity and R6G concentration using linear scale for the R6G concentration axis with the fitting equation of $y = \log x + m$, while Figures 6.2.6b and 6.2.6 d are the same plots on a logarithmic scale for the concentration axis. An approximately logarithmic relation can be observed since the fitting equation of $y = \log x + m$ fits well of the SERS intensity vs concentration curves as shown in Figure 6.2.6a and 6.2.6c, which is expected from the superposition of the plasmonic enhancement of the AuNPs and WS_2-NDs. Indeed, this logarithmic relation between the SERS intensity and concentration is consistent to the previous reports of SERS sensitivity employing different kinds of analyte molecules [50, 115-117] .However, the few higher R6G concentration

data points does not look to fit the trends as well as the lower R6G concentration data points, which was also observed in our previous report of MoS_2 (WS_2)-NDs/graphene vdW heterostructures SERS sensitivity using R6G [145].

Considering SERS sensitivity is primarily determined by the EM effect, it is important to understand the mechanism of the superposition of the evanescent electromagnetic fields by the AuNPs and WS_2-NDs. Depending on the shapes and sizes of metallic NPs and the materials they made of, plasmonic EM enhancement can, in general, increase the effective intensity of the incident light and shorten radiative decay lifetimes of molecules (Purcell effect). The plasmonic properties of the WS_2-NDs studied in this paper are partially associated with their optical doping [145]. As a result, a primary impact of AuNPs can be enhancement of excitation rates of such WS_2-NDs via plasmonic effects, i.e., $I_{eff} = P_{enh} I_0$ wherein P_{enh} refers to the plasmon field enhancement factor, defined as the ratio of the squares of the field in the presence of AuNPs to that when the AuNP is absent, and I_0 represents the incident light intensity.

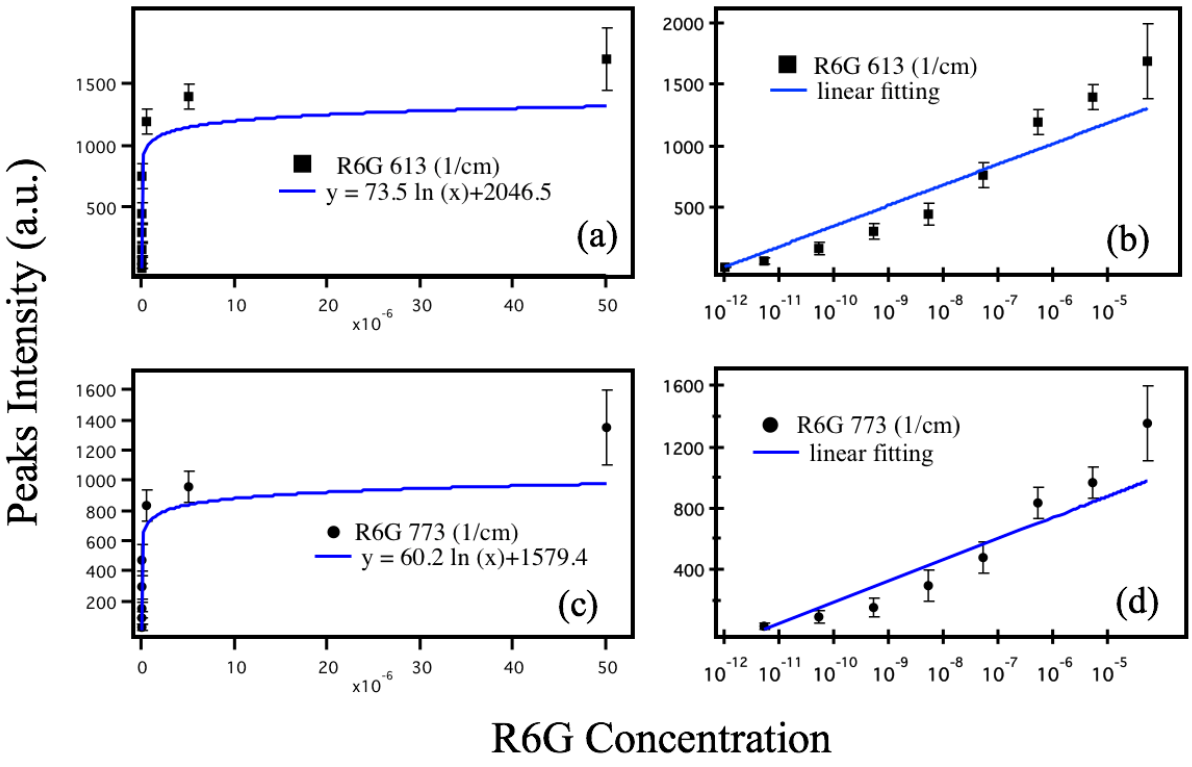

Figure 6.2.6 (a-d) The intensities of the Raman peaks as a function of the R6G concentrations at 613 cm^{-1} (a, b) and 773 cm^{-1} (c, d) for the AuNPs/WS_2-NDs/graphene substrate using 532 nm laser and using a linear scale (a, c) and a logarithmic scale (b, d).

Figure 6.2.7a illustrates schematically the structure for the Finite-Difference Time-Domain (FDTD) simulation. Specifically, the structure includes a semispherical AuNP of 40 nm in diameter on top of a layered structure consisting of a SiO_2 substrate covered with 5 nm thick TMD that is treated as a high refractive index dielectric material. Figure 6.2.7b shows the extinction spectrum of such a structure. This spectrum suggests that the AuNPs of the selected dimension supports formation of a sharp peak at about 568 nm. Interestingly, another peak at about 440 nm is also visible. Figure 6.2.7c shows the mode profile of the AuNP at the wavelength of 568 nm, indicating a significant field enhancement factor (P_{enh}) inside the 5-nm TMD layer. In fact, in the upper side of this layer P_{enh} is close to 15 and in the lower side P_{enh} reduces to about 4. Note that

the wavelength of this mode (568 nm), is close to the maximum peak responsivity of the photodetectors based on application of WS_2-NDs on graphene [148]. This suggests the possibility of coupling of the plasmon modes of the WS_2-NDs with those of the AuNPs, forming heterogeneous plasmonic dimmers. Such dimmers can offer more favorable field plasmon modes, particularly inside the 5-nm thick dielectric layer, leading to ultrahigh SERS sensitivities observed in this paper [149, 150].

Figure 6.2.7d shows that mode profile of the AuNP at 532 nm wavelength that is the wavelength of the laser used to excite the samples was 532 nm (Figure 6.2.7b, square). While the P_{enh} is smaller than that at the peak wavelength of the extinction spectrum, considerable enhancement remain as exhibited in Figure 6.2.7d Specifically, the field enhancement factor P_{enh} at the upper edge, middle and lower edge of the 5-nm thick TMD layer are respectively 10, 3 and 2. This suggests the laser intensity on the WS_2-NDs can be significantly enhanced by the plasmonic effects of the AuNPs.

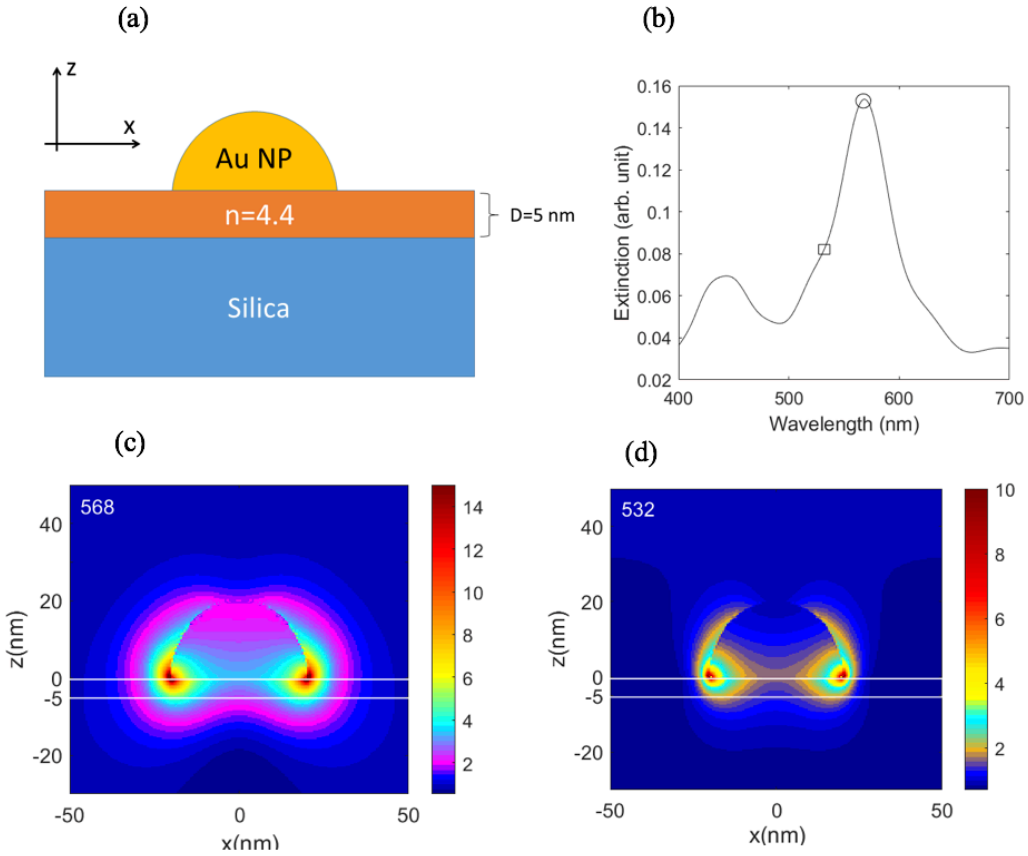

Figure 6.2.7 (a) Schematic of the structure adopted for simulations of plasmonic response of the Au NP. (b) Simulated extinction spectrum of the structure. The circle and square refer here to the wavelengths of the peak and incident laser used for SERS, respectively. (c) and (d) Simulated plasmonic modes of the Au NP at 568 and 532 nm. The scale bars are color-coded presentation of $\boldsymbol{P_{enh}}$ around the NP.

6.3 Conclusion

In summary, this work established a novel SERS substrate with extra high sensitivity-based plasmonic AuNP/WS_2 N-Discs/graphene vdW heterostructures. This substrate integrates two plasmonic nanostructures of AuNPs and WS_2 N-Discs, and the DFT and FDTD simulations indicate that the improved dipole–dipole interaction together with charge transfer at the vdW interfaces plays a critical role to enable superposition of their LSPR effects. This has been confirmed experimentally in observations of enhanced graphene Raman signatures and enhanced SERS sensitivity of R6G probe molecules on the AuNP/WS_2 N-Discs/graphene vdW

heterostructure, comparing to that on WS_2 N-Discs/graphene and AuNP/graphene substrates. Specifically, the graphene's G-peak intensity is enhanced by 7.8-fold by the combination of AuNPs and WS_2 N-Discs, in contrast to 5.3 or 4.0 folds respectively by WS_2 N-Discs or AuNPs alone. Moreover, the high R6G SERS sensitivity of 1×10^{-12} M achieved on the AuNP/WS_2 N-Discs /graphene substrates is one or three orders of magnitude enhancement over that of on the WS_2 N-Discs/graphene or AuNP/graphene, respectively. Furthermore, this sensitivity is two to four orders of magnitude better than that on the TMDs/metal nanostructure SERS substrates and at least an order of magnitude better than the best SERS substrates reported in previous works. This result therefore demonstrates a new path-way in superposition of the LSPR effect from two different kinds of plasmonic nanostructures via vdW heterostructures. Finally, the developed layer-by-layer synthesis process of transfer-free CVD growth of WS_2 N-Discs/graphene followed with in vacuo decoration of the AuNPs can be scale-up for run-to-run synthesis of the AuNP/WS_2 N-Discs/graphene vdW heterostructures SERS substrates for commercialization.

Chapter 7: Conclusion and future work

In this dissertation, new TMD nanostructure/graphene vdW SERS substrates have been explored experimentally for biosensing. Differing fundamentally from most previously reported SERS substrates that rely on metallic plasmonic nanostructures for enhanced EM effect, the non-metallic TMD nanostructure/graphene vdW SERS substrates are designed to both EM and CM enhancement. Density Function Theory simulation was applied to calculate the electronic structure of TMDs and graphene to understand the origin of the charge carrier doping in TMDs that enables SERS on TMD nanostructure/graphene. Furthermore, Finite Difference Time-Domain simulation was adopted to investigate the strength and distribution of electromagnetic evanescent fields generated around the plasmonic TMD nanostructure/graphene as the density and shape of TMD nanostructures are engineered experimentally for optimal SERS enhancement.

Five topics have been studied in this dissertation with an overarching focus on the understanding the material science and physics underlying the non-metallic TMD nanostructure/graphene vdW SERS substrates. In topic one, SERS TMD (MoS_2 and WS_2) N-discs on single-layer CVD graphene N-discs was synthesized using a CVD process and showed an extraordinary enhancement and sensitivity (up to 10^{-12} M) that may attribute to the combination of the CM enhancement due to the enhanced dipole-dipole interaction at the TMD/graphene interface and the EM enhancement through the LSPR on the photo-doped TMD N-discs/graphene. In topic two, methods to achieve high TMD N-discs density was exploited for more enhanced SERS. Mixing two kinds of TMDs (WS_2+MoS_2) N-discs on graphene leads to higher ND density and more enhanced SERS substrates. The obtained high SERS sensitivity up to 5-7×10^{-13} M which is about one order of magnitude higher than that on the single TMD N-discs/graphene counterparts.

In topic three, we further explored the effect of a TMD's shape on the EM effect and SERS enhancement. By changing the concentration of the (NH_4) $2MoS_4$ precursor solution in the range of 0.06-0.40 wt%, we were able to grow TMDs nanodonuts on graphene SERS substrate. A remarkably high R6G SERS sensitivity up to 2×10^{-12} M has been obtained on TMDs nanodonuts/graphene SERS in contrast to the one was obtained on TMDs nanodiscs/graphene SERS substrate, which can be attributed to the more robust LSPR effect than in other TMD nanostructures such as nanodiscs as suggested by the finite-difference time-domain simulation. In topic four, we decorated the TMDs/graphene SERS substrate with plasmonic nanostructures of AuNPs to obtain substrate that integrates two plasmonic nanostructures of AuNPs and WS_2 N-Discs. We found an enhanced SERS sensitivity of R6G probe molecules on the AuNP/WS_2 N-Discs/graphene vdW heterostructure, comparing to that on WS_2 N-Discs/graphene and AuNP/graphene substrates. Specifically, the graphene's G-peak intensity is enhanced by 7.8-fold by the combination of AuNPs and WS_2 N-Discs, in contrast to 5.3 or 4.0 folds respectively by WS_2 N-Discs or AuNPs alone. the high R6G SERS sensitivity of 1×10^{-12} M achieved on the AuNP/WS_2 N-Discs /graphene substrates is one or three orders of magnitude enhancement over that of on the WS_2 N-Discs/graphene or AuNP/graphene, respectively.

For the future work, although, we have done an interesting work to improve the EM effect, we still can improve the CM effect. Therefore, we will focus on how to improve the CM effect. One way, we can use ultraviolet (UV) irradiation to the oxidation of the graphene which was reported larger contribution to CE on aromatic dye molecules than that from the pristine graphene and enhance SERS on the TMDs/graphene substrate.

References

1. Novoselov, K.S., et al., Electric field effect in atomically thin carbon films. Science, 2004. **306**(5696): p. 666-9.
2. Coleman, J.N., et al., Two-dimensional nanosheets produced by liquid exfoliation of layered materials. Science, 2011. **331**(6017): p. 568-71.
3. Mak, K.F., et al., Atomically thin MoS(2): a new direct-gap semiconductor. Phys Rev Lett, 2010. **105**(13): p. 136805.
4. Xia, F., et al., Two-dimensional material nanophotonics. Nature Photonics, 2014. **8**(12): p. 899-907.
5. Castro Neto, A.H., et al., The electronic properties of graphene. Reviews of Modern Physics, 2009. **81**(1): p. 109-162.
6. Mak, K.F., et al., Measurement of the optical conductivity of graphene. Phys Rev Lett, 2008. **101**(19): p. 196405.
7. Balandin, A.A., Thermal properties of graphene and nanostructured carbon materials. Nat Mater, 2011. **10**(8): p. 569-81.
8. Lee, C., et al., Measurement of the elastic properties and intrinsic strength of monolayer graphene. Science, 2008. **321**(5887): p. 385-8.
9. M K, K. and M. Jaiswal, Graphene: A review of optical properties and photonic applications. Asian Journal of Physics, 2016. **25**: p. 809-831.
10. Novoselov, K.S., et al., Two-dimensional gas of massless Dirac fermions in graphene. Nature, 2005. **438**(7065): p. 197-200.
11. Du, X., et al., Approaching ballistic transport in suspended graphene. Nat Nanotechnol, 2008. **3**(8): p. 491-5.
12. Geim, A.K., Graphene: status and prospects. Science, 2009. **324**(5934): p. 1530-4.
13. Meyer, J.C., et al., The structure of suspended graphene sheets. Nature, 2007. **446**(7131): p. 60-3.
14. Avouris, P., Graphene: electronic and photonic properties and devices. Nano Lett, 2010. **10**(11): p. 4285-94.
15. Huh, S., et al., UV/ozone-Oxidized Large-Scale Graphene Platform with Large Chemical Enhancement in Surface-Enhanced Raman Scattering. ACS Nano, 2011. **5**(12): p. 9799-806.
16. Ling, X., et al., Can graphene be used as a substrate for Raman enhancement? Nano Letters, 2010. **10**(2): p. 553-61.
17. Huang, X., et al., Graphene-Based Electrodes. Advanced Materials, 2012. **24**(45): p. 5979-6004.
18. Wang, Z., et al., Direct Electrochemical Reduction of Single-Layer Graphene Oxide and Subsequent Functionalization with Glucose Oxidase. The Journal of Physical Chemistry C, 2009. **113**(32): p. 14071-14075.
19. Pang, S., et al., Patterned Graphene Electrodes from Solution-Processed Graphite Oxide Films for Organic Field-Effect Transistors. Advanced Materials, 2009. **21**(34): p. 3488-3491.

20. Li, B., et al., All-Carbon Electronic Devices Fabricated by Directly Grown Single-Walled Carbon Nanotubes on Reduced Graphene Oxide Electrodes. Advanced Materials, 2010. **22**(28): p. 3058-3061.
21. Schwierz, F., Graphene transistors. Nature Nanotechnology, 2010. **5**(7): p. 487-496.
22. Wang, J., et al., Rod-Coating: Towards Large-Area Fabrication of Uniform Reduced Graphene Oxide Films for Flexible Touch Screens. Advanced Materials, 2012. **24**(21): p. 2874-2878.
23. Xia, F., et al., Ultrafast graphene photodetector. Nature Nanotechnology, 2009. **4**(12): p. 839-843.
24. Lee, J.Y., et al., Two-dimensional semiconductor optoelectronics based on van der Waals heterostructures. Nanomaterials, 2016. **6**(11): p. 193.
25. Geim, A.K. and I.V. Grigorieva, Van der Waals heterostructures. Nature, 2013. **499**(7459): p. 419-25.
26. Dickinson, R.G.P., Linus, The Crystal Structure of Molybdenite. Journal of the American Chemical Society, 1923. **45(6)**: p. 1466-1471.
27. Splendiani, A., et al., Emerging Photoluminescence in Monolayer MoS2. Nano Letters, 2010. **10**(4): p. 1271-1275.
28. Eda, G. and S.A. Maier, Two-dimensional crystals: managing light for optoelectronics. ACS nano, 2013. **7**(7): p. 5660-5665.
29. Yin, Z.Y., et al., Single-Layer MoS2 Phototransistors. Acs Nano, 2012. **6**(1): p. 74-80.
30. Amani, M., et al., Near-unity photoluminescence quantum yield in MoS(2). Science, 2015. **350**(6264): p. 1065-8.
31. Zhang, Y., et al., Direct observation of the transition from indirect to direct bandgap in atomically thin epitaxial MoSe2. Nat Nanotechnol, 2014. **9**(2): p. 111-5.
32. Song, I., C. Park, and H.C. Choi, Synthesis and properties of molybdenum disulphide: from bulk to atomic layers. Rsc Advances, 2015. **5**(10): p. 7495-7514.
33. Alharbi, F., et al., Abundant non-toxic materials for thin film solar cells: Alternative to conventional materials. Renewable Energy, 2011. **36**(10): p. 2753-2758.
34. Zhang, Y., et al., Direct observation of the transition from indirect to direct bandgap in atomically thin epitaxial MoSe2. Nature Nanotechnology, 2014. **9**(2): p. 111-5.
35. Geim, A.K. and I.V. Grigorieva, Van der Waals heterostructures. Nature, 2013. **499**(7459): p. 419-425.
36. Levendorf, M.P., et al., Graphene and boron nitride lateral heterostructures for atomically thin circuitry. Nature, 2012. **488**(7413): p. 627-32.
37. Dean, C.R., et al., Boron nitride substrates for high-quality graphene electronics. Nat Nanotechnol, 2010. **5**(10): p. 722-6.
38. Hong, X., et al., Ultrafast charge transfer in atomically thin MoS(2)/WS(2) heterostructures. Nat Nanotechnol, 2014. **9**(9): p. 682-6.
39. Liu, K., et al., Elastic properties of chemical-vapor-deposited monolayer MoS2, WS2, and their bilayer heterostructures. Nano Lett, 2014. **14**(9): p. 5097-103.
40. Aroca, R., Surface enhanced vibrational spectroscopy. 2006, Hoboken, NJ: Wiley. xxv, 233 p.
41. Fang, Y., N.H. Seong, and D.D. Dlott, Measurement of the Distribution of Site Enhancements in Surface-Enhanced Raman Scattering. sci, 2008. **321**(5887): p. 388-92.
42. Lin, H.X., et al., Uniform Gold Spherical Particles for Single-Particle Surface-Enhanced Raman Spectroscopy. Phys Chem Chem Phys, 2013. **15**(12): p. 4130-5.

43. Potara, M., et al., Chitosan-coated anisotropic silver nanoparticles as a SERS substrate for single-molecule detection. Nanotechnology, 2012. **23**(5): p. 055501-055510.
44. Sivashanmugan, K., et al., Focused-Ion-Beam-Fabricated Au Nanorods Coupled with Ag Nanoparticles Used as Surface-Enhanced Raman Scattering-Active Substrate for Analyzing Trace Melamine Constituents in Solution. Anal Chim Acta, 2013. **800**: p. 56-64.
45. Li, X., et al., A self-powered graphene–MoS2 hybrid phototransistor with fast response rate and high on–off ratio. Carbon, 2015. **92**: p. 126-132.
46. Willets, K.A. and R.P.V. Duyne, Localized Surface Plasmon Resonance Spectroscopy and Sensing. Annual Review of Physical Chemistry, 2007. **58**(1): p. 267-297.
47. Guerrini, L. and D. Graham, Molecularly-Mediated Assemblies of Plasmonic Nanoparticles for Surface-Enhanced Raman Spectroscopy Applications. Chem Soc Rev, 2012. **41**(21): p. 7085-107.
48. Mu, C., J.P. Zhang, and D. Xu, Au nanoparticle arrays with tunable particle gaps by template-assisted electroless deposition for high performance surface-enhanced Raman scattering. Nanotechnology, 2010. **21**(1): p. 015604-015609.
49. Chen, L., et al., Urchin-like LaVO(4)/Au composite microspheres for surface-enhanced Raman scattering detection. Journal of Colloid and Interface Science, 2015. **443**: p. 80-7.
50. Goul, R., et al., Quantitative Analysis of Surface Enhanced Raman Spectroscopy of Rhodamine 6G Using a Composite Graphene and Plasmonic Au Nanoparticle Substrate. Carbon, 2017. **111**: p. 386-392.
51. Zhang, C., et al., SERS detection of R6G based on a novel graphene oxide/silver nanoparticles/silicon pyramid arrays structure. Optics Express, 2015. **23**(19): p. 24811-21.
52. Seney, C.S., B.M. Gutzman, and R.H. Goddard, Correlation of Size and Surface-Enhanced Raman Scattering Activity of Optical and Spectroscopic Properties for Silver Nanoparticles. The Journal of Physical Chemistry C, 2009. **113**(1): p. 74-80.
53. Stamplecoskie, K.G., et al., Optimal Size of Silver Nanoparticles for Surface-Enhanced Raman Spectroscopy. The Journal of Physical Chemistry C, 2011. **115**(5): p. 1403-1409.
54. Xu, W., N. Mao, and J. Zhang, Graphene: a Platform for Surface-Enhanced Raman Spectroscopy. Small, 2013. **9**(8): p. 1206-24.
55. Xu, W., et al., Surface enhanced Raman spectroscopy on a flat graphene surface. Proceedings of the National Academy of Sciences of the United States of America, 2012. **109**(24): p. 9281-6.
56. Tan, Y., et al., Two-Dimensional Heterostructure as a Platform for Surface-Enhanced Raman Scattering. Nano Letters, 2017. **17**(4): p. 2621-2626.
57. Ling, X., et al., Charge-Transfer Mechanism in Graphene-Enhanced Raman Scattering. The Journal of Physical Chemistry C, 2012. **116**(47): p. 25112-25118.
58. Xie, L., et al., Graphene as a substrate to suppress fluorescence in resonance Raman spectroscopy. Journal of the American Chemical Society, 2009. **131**(29): p. 9890-1.
59. Xu, W., et al., Graphene-veiled gold substrate for surface-enhanced Raman spectroscopy. Advanced Materials, 2013. **25**(6): p. 928-33.
60. Ling, X., et al., Raman enhancement effect on two-dimensional layered materials: graphene, h-BN and MoS2. Nano Letters, 2014. **14**(6): p. 3033-40.
61. Yin, Y., et al., Significantly Increased Raman Enhancement on MoX2 (X = S, Se) Monolayers upon Phase Transition. Adv. Funct. Mater, 2017. **27**(16): p. 1606694-7.

62. Qiu, H., et al., Large-Area MoS2 Thin Layers Directly Synthesized on Pyramid-Si Substrate for Surface-Enhanced Raman Scattering. RSC Advances, 2015. **5**(102): p. 83899-83905.
63. Xu, Y.Y., et al., Layer-Controlled Large Area MoS 2 Layers Grown on Mica Substrate for Surface-Enhanced Raman Scattering. Appl. Surf. Sci., 2015. **357**: p. 1708-1713.
64. Lu, R., et al., High Sensitivity Surface Enhanced Raman Spectroscopy of R6G on in Situ Fabricated Au Nanoparticle/Graphene Plasmonic Substrates. Carbon, 2015. **86**: p. 78-85.
65. Xu, S., et al., Graphene isolated Au nanoparticle arrays with high reproducibility for high-performance surface-enhanced Raman scattering. Sensors and Actuators, B, 2016. **222**: p. 1175-1183.
66. Hai-Bin, S., et al., Enhanced Raman scattering of graphene by silver nanoparticles with different densities and locations. Materials Research Express, 2017. **4**(2): p. 025012.
67. Fan, W., et al., Graphene oxide and shape-controlled silver nanoparticle hybrids for ultrasensitive single-particle surface-enhanced Raman scattering (SERS) sensing. Nanoscale, 2014. **6**(9): p. 4843-4851.
68. Novoselov, K.S. and A.H. Castro Neto, Two-dimensional crystals-based heterostructures: materials with tailored properties. Physica Scripta, 2012. **T146**.
69. Ghopry, S.A., et al., Extraordinary Sensitivity of Surface-Enhanced Raman Spectroscopy of Molecules on MoS2 (WS2) Nanodomes/Graphene van der Waals Heterostructure Substrates. Adv. Opt. Mater, 2019. **7**(8): p. 1801249-11.
70. Liu, Q.F., et al., Printable Transfer-Free and Wafer-Size MoS2/Graphene van der Waals Heterostructures for High-Performance Photodetection. Acs Applied Materials & Interfaces, 2017. **9**(14): p. 12728-12733.
71. Alamri, M., et al., Plasmonic Au Nanoparticles on 2D MoS2/Graphene van der Waals Heterostructures for High-Sensitivity Surface-Enhanced Raman Spectroscopy. ACS Applied Nano Materials, 2019. **2**(3): p. 1412-1420.
72. Xu, G., et al., Plasmonic Graphene Transparent Conductors. Advanced Materials, 2012. **24**(10): p. OP71-OP76.
73. Gong, M., et al., Broadband Photodetectors Enabled by Localized Surface Plasmonic Resonance in Doped Iron Pyrite Nanocrystals. Advanced Optical Materials, 2018. **6**(8): p. 1701241.
74. Dion, M., et al., van der Waals density functional for general geometries. Physical Review Letters, 2004. **92**(24): p. 246401.
75. Román-Pérez, G. and J.M. Soler, Efficient Implementation of a van der Waals Density Functional: Application to Double-Wall Carbon Nanotubes. Physical Review Letters, 2009. **103**(9): p. 096102.
76. Henkelman, G., A. Arnaldsson, and H. Jónsson, A fast and robust algorithm for Bader decomposition of charge density. Computational Materials Science, 2006. **36**(3): p. 354-360.
77. Sanville, E., et al., Improved grid-based algorithm for Bader charge allocation. Journal of Computational Chemistry, 2007. **28**(5): p. 899-908.
78. Tang, W., E. Sanville, and G. Henkelman, A grid-based Bader analysis algorithm without lattice bias. Journal of Physics: Condensed Matter, 2009. **21**(8): p. 084204.
79. Blöchl, P.E., Projector augmented-wave method. Physical Review B: Condensed Matter, 1994. **50**(24): p. 17953-17979.

80. Kohn, W. and L.J. Sham, Self-Consistent Equations Including Exchange and Correlation Effects. Physical Review, 1965. **140**(4A): p. A1133-A1138.
81. Kresse, G. and J. Furthmuller, Efficient iterative schemes for ab initio total-energy calculations using a plane-wave basis set. Phys Rev B Condens Matter, 1996. **54**(16): p. 11169-11186.
82. Chen, C.T., et al., Very High Refractive Index Transition Metal Dichalcogenide Photonic Conformal Coatings by Conversion of ALD Metal Oxides. Sci Rep, 2019. **9**(1): p. 2768.
83. Li, Y.L., et al., Measurement of the optical dielectric function of monolayer transition-metal dichalcogenides: MoS2, MoSe2, WS2, and WSe2. Physical Review B, 2014. **90**(20).
84. Liu, H.L., et al., Optical properties of monolayer transition metal dichalcogenides probed by spectroscopic ellipsometry. Applied Physics Letters, 2014. **105**(20).
85. Gamucci, A., et al., Anomalous low-temperature Coulomb drag in graphene-GaAs heterostructures. Nature Communications, 2014. **5**: p. 5824.
86. Georgiou, T., et al., Vertical field-effect transistor based on graphene-WS2 heterostructures for flexible and transparent electronics. Nature Nanotechnology, 2013. **8**(2): p. 100-3.
87. Ma, Y., et al., Graphene adhesion on MoS(2) monolayer: an ab initio study. Nanoscale, 2011. **3**(9): p. 3883-7.
88. Roy, K., et al., Graphene-MoS2 hybrid structures for multifunctional photoresponsive memory devices. Nature Nanotechnology, 2013. **8**(11): p. 826-30.
89. Luther, J.M., et al., Localized surface plasmon resonances arising from free carriers in doped quantum dots. Nature Materials, 2011. **10**(5): p. 361-6.
90. Liang, L. and V. Meunier, First-principles Raman spectra of MoS2, WS2 and their heterostructures. Nanoscale, 2014. **6**(10): p. 5394-401.
91. Liu, Q., et al., Printable Transfer-Free and Wafer-Size MoS2/Graphene van der Waals Heterostructures for High-Performance Photodetection. ACS Applied Materials & Interfaces, 2017. **9**(14): p. 12728-12733.
92. Yu, Y., et al., Controlled scalable synthesis of uniform, high-quality monolayer and few-layer MoS2 films. Scientific Reports, 2013. **3**: p. 1866.
93. Lin, Z., et al., Controllable Growth of Large-Size Crystalline MoS2 and Resist-Free Transfer Assisted with a Cu Thin Film. Scientific Reports, 2015. **5**: p. 18596.
94. Buscema, M., et al., The effect of the substrate on the Raman and photoluminescence emission of single-layer MoS2. Nano Research, 2015. **7**(4): p. 561-571.
95. Feng, S., et al., Ultrasensitive molecular sensor using N-doped graphene through enhanced Raman scattering. Science Advances, 2016. **2**(7): p. e1600322.
96. Li, M., et al., Detection of adenosine triphosphate with an aptamer biosensor based on surface-enhanced Raman scattering. Analytical Chemistry, 2012. **84**(6): p. 2837-42.
97. Shi, Y., et al., Ultrasensitive, Specific, Recyclable, and Reproducible Detection of Lead Ions in Real Systems through a Polyadenine-Assisted, Surface-Enhanced Raman Scattering Silicon Chip. Analytical Chemistry, 2016. **88**(7): p. 3723-9.
98. Hwang, J.S. and M. Yang, Sensitive and Reproducible Gold SERS Sensor Based on Interference Lithography and Electrophoretic Deposition. Sensors, 2018. **18**: p. 4076.
99. Zong, C., et al., In situ synthesis of low-cost and large-scale flexible metal nanoparticle–polymer composite films as highly sensitive SERS substrates for surface trace analysis. RSC Advances, 2019. **9**: p. 2857-2864.

100. Xu, L., et al., Two-Dimensional MoS2-Graphene-Based Multilayer van der Waals Heterostructures: Enhanced Charge Transfer and Optical Absorption, and Electric-Field Tunable Dirac Point and Band Gap. Chemistry of Materials, 2017. **29**(13): p. 5504-5512.
101. Joo, Y., et al., Effect of Dipolar Molecule Structure on the Mechanism of Graphene-Enhanced Raman Scattering. Journal of Physical Chemistry C, 2016. **120**(25): p. 13815-13824.
102. Lo, S.S., et al., Emergent properties resulting from type-II band alignment in semiconductor nanoheterostructures. Advanced Materials, 2011. **23**(2): p. 180-97.
103. Buonsanti, R., et al., Tunable infrared absorption and visible transparency of colloidal aluminum-doped zinc oxide nanocrystals. Nano Letters, 2011. **11**(11): p. 4706-10.
104. Liu, Q., et al., Printable Transfer-Free and Wafer-Size MoS2/Graphene van der Waals Heterostructures for High-Performance Photodetection. ACS Appl Mater Interfaces, 2017. **9**(14): p. 12728-12733.
105. Chen, K., et al., Lateral Built-In Potential of Monolayer MoS2-WS2 In-Plane Heterostructures by a Shortcut Growth Strategy. Adv Mater, 2015. **27**(41): p. 6431-7.
106. Guo, Y., X. Fu, and Z. Peng, Controllable Synthesis of MoS 2 Nanostructures from Monolayer Flakes, Few-Layer Pyramids to Multilayer Blocks by Catalyst-Assisted Thermal Evaporation. J. Mater. Sci., 2018. **53**(11): p. 8098-8107.
107. Kim, S.K., et al., Synergetic Effect at the Interfaces of Solution Processed MoS 2 -WS 2 Composite for Hydrogen Evolution Reaction. Appl. Surf. Sci., 2017. **425**: p. 241-245.
108. Wang, F., et al., Tuning Coupling Behavior of Stacked Heterostructures Based on MoS 2 , WS 2 , and WSe 2. Sci. Rep, 2017. **7**(1): p. 44712-44722.
109. Liu, J., et al., Doped Graphene Nanohole Arrays for Flexible Transparent Conductors. Appl. Phys. Lett., 2011. **99**(2): p. 023111-3.
110. Mahigir, A., et al., Plasmonic nanohole array for enhancing the SERS signal of a single layer of graphene in water. Sci Rep, 2017. **7**(1): p. 14044-14052.
111. Zhang, S.G., et al., Raman Peak Enhancement and Shift of Few-Layer Graphene Induced by Plasmonic Coupling with Silver Nanoparticles. Appl. Phys. Lett., 2014. **104**(12): p. 121109-5.
112. Ghopry, S.A., et al., Au Nanoparticle/WS2 Nanodome/Graphene van der Waals Heterostructure Substrates for Surface-Enhanced Raman Spectroscopy. ACS Appl. Nano Mater., 2020. **3**(3): p. 2354-2363.
113. Hou, M.-J., et al., Preparation of SiO2@ Au Nanorod Array as Novel Surface Enhanced Raman Substrate for Trace Pollutants Detection. Chin. Phys. B, 2015. **24**(3): p. 034203-4.
114. Xu, S., et al., Graphene Isolated Au Nanoparticle Arrays with High Reproducibility for High-Performance Surface-Enhanced Raman Scattering. SENSOR ACTUAT B-CHEM, 2016. **222**: p. 1175-1183.
115. Li, M., et al., Detection of Adenosine Triphosphate with an Aptamer Biosensor based on Surface-Enhanced Raman Scattering. Anal Chem, 2012. **84**(6): p. 2837-42.
116. Shi, Y., et al., Ultrasensitive, Specific, Recyclable, and Reproducible Detection of Lead Ions in Real Systems through a Polyadenine-Assisted, Surface-Enhanced Raman Scattering Silicon Chip. Anal Chem, 2016. **88**(7): p. 3723-9.
117. Xie, L., et al., Graphene as a Substrate to Suppress Fluorescence in Resonance Raman Spectroscopy. J Am Chem Soc, 2009. **131**(29): p. 9890-1.
118. Hong, S. and X. Li, Optimal Size of Gold Nanoparticles for Surface-Enhanced Raman Spectroscopy under Different Conditions. Journal of Nanomaterials, 2013. **2013**: p. 1-9.

119. Yoon, J.K., K. Kim, and K.S. Shin, Raman Scattering of 4-Aminobenzenethiol Sandwiched between Au Nanoparticles and a Macroscopically Smooth Au Substrate: Effect of Size of Au Nanoparticles. The Journal of Physical Chemistry C, 2009. **113**(5): p. 1769-1774.
120. Mir-Simon, B., et al., SERS efficiencies of micrometric polystyrene beads coated with gold and silver nanoparticles: the effect of nanoparticle size. Journal of Optics, 2015. **17**(11).
121. Yoon, J.H., et al., Surface Plasmon Coupling in Dimers of Gold Nanoparticles: Experiment and Theory for Ideal (Spherical) and Nonideal (Faceted) Building Blocks. ACS Photonics, 2019. **6**(3): p. 642-648.
122. Makam, P., et al., SERS and fluorescence-based ultrasensitive detection of mercury in water. Biosens Bioelectron, 2018. **100**: p. 556-564.
123. Zhu, J., et al., Multi-branched gold nanostars with fractal structure for SERS detection of the pesticide thiram. Spectrochim Acta A Mol Biomol Spectrosc, 2018. **189**: p. 586-593.
124. Chen, X., et al., Use of Standing Gold Nanorods for Detection of Malachite Green and Crystal Violet in Fish by SERS. J Food Sci, 2017. **82**(7): p. 1640-1646.
125. Zhang, C.H., et al., Small and Sharp Triangular Silver Nanoplates Synthesized Utilizing Tiny Triangular Nuclei and Their Excellent SERS Activity for Selective Detection of Thiram Residue in Soil. ACS Appl Mater Interfaces, 2017. **9**(20): p. 17387-17398.
126. Li, D., et al., Griess reaction-based paper strip for colorimetric/fluorescent/SERS triple sensing of nitrite. Biosens Bioelectron, 2018. **99**: p. 389-398.
127. Li, Q., et al., Production of Monodisperse Gold Nanobipyramids with Number Percentages Approaching 100% and Evaluation of Their Plasmonic Properties. Advanced Optical Materials, 2015. **3**(6): p. 801-812.
128. Fan, W., et al., Graphene oxide and shape-controlled silver nanoparticle hybrids for ultrasensitive single-particle surface-enhanced Raman scattering (SERS) sensing. Nanoscale, 2014. **6**(9): p. 4843-51.
129. Alamri, M., et al., Plasmonic Au Nanoparticles on 2D MoS2/Graphene van der Waals Heterostructures for High-Sensitivity Surface-Enhanced Raman Spectroscopy. ACS Appl. Nano Mater, 2019. **2**(3): p. 1412-1420.
130. Chen, P.X., et al., A Novel Surface-Enhanced Raman Spectroscopy Substrate Based on a Large Area of MoS2 and Ag Nanoparticles Hybrid System. Appl. Surf. Sci., 2016. **375**: p. 207-214.
131. Lu, Z., et al., Sensitive, Reproducible, and Stable 3D Plasmonic Hybrids with Bilayer WS2 as Nanospacer for SERS Analysis. Optics Express, 2018. **26**(17): p. 21626-21641.
132. Shorie, M., et al., Plasmonic DNA Hotspots Made from Tungsten Disulfide Nanosheets and Gold Nanoparticles for Ultrasensitive Aptamer-Based SERS Detection of Myoglobin. Mikrochim Acta, 2018. **185**(3): p. 158-8.
133. Saito, R., et al., Raman spectroscopy of graphene and carbon nanotubes. Advances in Physics, 2011. **60**(3): p. 413-550.
134. Lee, C., et al., Anomalous lattice vibrations of single- and few-layer MoS2. ACS Nano, 2010. **4**(5): p. 2695-700.
135. Hou, M.-J., et al., Preparation of SiO2@ Au nanorod array as novel surface enhanced Raman substrate for trace pollutants detection. Chinese Physics B, 2015. **24**(3): p. 034203-034206.

136. Ghopry, S.A., et al., Au Nanoparticle/WS2 Nanodome/Graphene van der Waals Heterostructure Substrates for Surface-Enhanced Raman Spectroscopy. ACS Applied Nano Materials, 2020. **3**(3): p. 2354-2363.
137. Ghopry, S.A., et al., Intermixed WS2+MoS2 Nanodisks/Graphene van der Waals Heterostructures for Surface-Enhanced Raman Spectroscopy Sensing. ACS Applied Nano Materials, 2021. **4**(3): p. 2941-2951.
138. Liu, Y. and F. Luo, Large-Scale Highly Ordered Periodic Au Nano-discs/Graphene and Graphene/Au Nanoholes Plasmonic Substrates for Surface-Enhanced Raman Scattering. Nano Research, 2019. **12**(11): p. 2788-2795.
139. Liu, Y. and F. Luo, Spatial Raman Mapping Investigation of SERS Performance Related to Localized Surface Plasmons. Nano Res., 2020. **13**(1): p. 138-144.
140. Xu, W., et al., Surface Enhanced Raman Spectroscopy on a Flat Graphene Surface. Proc Natl Acad Sci U S A, 2012. **109**(24): p. 9281-6.
141. Zhang, S.G., et al., Raman peak enhancement and shift of few-layer graphene induced by plasmonic coupling with silver nanoparticles. Applied Physics Letters, 2014. **104**(12): p. 121109-121114.
142. Zhao, W., et al., Lattice dynamics in mono- and few-layer sheets of WS2 and WSe2. Nanoscale, 2013. **5**(20): p. 9677-83.
143. Huh, S., et al., UV/ozone-oxidized large-scale graphene platform with large chemical enhancement in surface-enhanced Raman scattering. ACS nano, 2011. **5**(12): p. 9799-9806.
144. Meng-Jing, H., et al., Preparation of SiO2@ Au nanorod array as novel surface enhanced Raman substrate for trace pollutants detection. Chinese Physics B, 2015. **24**(3): p. 034203.
145. Ghopry, S., et al., Extraordinary Sensitivity of Surface-Enhanced Raman Spectroscopy of Molecules on MoS2 (WS2) Nanodomes/Graphene van der Waals Heterostructure Substrates Advanced Optical Materials, 2019: p. 1801249-1801259.
146. Chen, P.X., et al., A novel surface-enhanced Raman spectroscopy substrate based on a large area of MoS 2 and Ag nanoparticles hybrid system. Applied Surface Science, 2016. **375**: p. 207-214.
147. Lu, Z., et al., Sensitive, reproducible, and stable 3D plasmonic hybrids with bilayer WS2 as nanospacer for SERS analysis. Opt Express, 2018. **26**(17): p. 21626-21641.
148. Alamri, M., et al., Plasmonic WS2 Nanodiscs/Graphene van der Waals Heterostructure Photodetectors. ACS Appl Mater Interfaces, 2019. **11**(36): p. 33390-33398.
149. Oubre, C. and P. Nordlander, Finite-difference time-domain studies of the optical properties of nanoshell dimers. Journal of Physical Chemistry B, 2005. **109**(20): p. 10042-10051.
150. Romero, I., et al., Plasmons in nearly touching metallic nanoparticles: singular response in the limit of touching dimers. Optics Express, 2006. **14**(21): p. 9988-9999.